MODELING THE DUST CYCLE ON MARS WITH THE GLOBAL MARS MULTISCALE MODEL GEM-MARS

DI WU

A DISSERTATION SUBMITTED TO
THE FACULTY GRADUATE STUDIES
IN PARTIAL FULFILLMENT OF THE REQUIREMENTS
FOR THE DEGREE OF

DOCTOR OF PHILOSOPHY

Graduate Program in Earth and Space Science
York University
Toronto, Ontario

September 2015

Abstract

The Mars atmosphere General Circulation Model GEM-Mars developed at York University has been used to simulate the dust cycle on Mars. The dynamic core is based on the Canadian operational weather forecast Global Environmental Multiscale NWP Model (GEM 3.3.0). Both dust devils and wind shear lifting schemes are included in the model. The wind shear scheme was modified from the terrestrial Dust Entrainment And Deposition (DEAD) model. This study has explored the two dust lifting schemes, dust radiative transfer, dust dry deposition, and other physical schemes, such as CO_2 thermal infrared transfer, CO_2 near-infrared absorption, UV-EUV heating, surface force-restore method, turbulence and diffusion, and CO_2 condensation schemes. The expanded model has successfully simulated Mars dust cycles in a spontaneous and self-consistent way. Our results agree with observations that: during the perihelion season (roughly southern spring and summer, solar insulation is stronger, the solar longitude Ls = 180^0-360^0) the Martian atmosphere is relatively warm and dusty, and during the aphelion season (Ls = 0^0-180^0) it is relatively cool with less dust. The simulated dust vertical distributions and atmospheric temperatures are generally consistent with the MCS and Phoenix observations. The two dust lifting schemes

both contribute to atmospheric dust loading with mechanical lifting scheme triggering dust storms while dust devils keep the atmospheric dust background. However, our simulated dust storms show a regular variability with time and locations every Mars year without inter-annual variability.

Acknowledgements

I would like to thank my supervisor Prof. Peter A. Taylor for his valuable support and help. His wide knowledge about atmospheric science and admired personality have been of great value to me. I also like to thank my PhD committee Professor Yongsheng Chen and Professor Jim Whiteway for their continuous support and guide.

I would like to thank Dr. Akingunola who introduced me the latest Mars model, and Dr. Hao who introduced the terrestrial dust model to me. Especially I thank my previous supervisor Professor McConnell (deceased), and research group members Dr. Kaminski, Dr. Beagley, Dr. Lupu, and Dr. Toyota who gave me constantly valuable advices and helps. I am also thankful to NSERC for supporting me during my Master's degree and PhD studies from 2008 to 2012.

Table of Contents

Abstract ii

Acknowledgements iv

Table of Contents v

List of Tables viii

List of Figures ix

1 Introduction 1

1.1 Overview of Mars 1

1.2 Mars topography 3

1.3 Atmosphere of Mars 5

1.4 Dust storms on Mars 8

1.5 Modeling the Martian dust cycle 13

1.6 The goals of this study and the structure of this thesis 15

2 The Description of Global Mars Model: GEM-Mars (YorkU) 17

2.1 Dust Solar radiation: Delat-Eddington and two-stream approximation 18

2.2 Dust IR radiation transfer 19

2.3 CO_2 thermal infrared transfer 20

2.4 Non local thermodynamic equilibrium (non-LTE)..... 21

2.5 UV-EUV heating 22

2.6 CO_2 near-infrared absorption..... 22

2.7 Dust thermal convection lifting scheme 23

2.8 Dust mechanical lifting scheme-DEAD model 25

2.8.1 Saltation processes and horizontal saltation mass flux..... 28

2.8.2 Vertical dust mass flux and vertical diffusion 30

2.8.3 Dust particle size distributions 31

2.8.4 Dust dry deposition..... 33

2.9 Surface scheme: GEM force-restore method..... 34

2.10 Vertical diffusion and boundary layer: GEM turbulence and diffusion 36

2.11 CO_2 condensation 40

2.12 The dynamics of GEM..... 42

3 Simulation with a one-dimensional model 46

3.1 Radiative schemes testing and comparison with UH 1-D model 46

3.2 Dust lifting schemes 53

3.3 Surface heat budget..... 56

4 Simulation with 3-D GEM-Mars 62

4.1 The dust cycles in multiyear simulation and observation 63

4.2 The CO_2 cycles in multiyear simulation and observation 69

4.3 The variations of dust in different seasons 71

4.4 The vertical dust distribution and vertical temperature profiles 81

4.4.1 GEM-Mars dust vertical profile comparing with prescribed dust profile 81

4.4.2 Comparison with MCS datasets 84

4.5 Comparison with Phoenix datasets 91

4.5.1 Comparison with atmospheric dust optical depth 92

4.5.2 Comparison with LIDAR measurements 94

4.5.3 Comparison with entry data from ASE 95

4.5.4 Comparison with near surface temperature from MET 97

4.5.5 Cross section above Phoenix lander location from GEM-Mars 99

4.6 Zonal mean structure and global circulation of the Martian atmosphere 100

4.7 Comparison dusty atmosphere with clear atmosphere 106

5 Conclusions 111

References 115

Appendix A Delta-Eddington Approximation 128

List of Tables

1.1 Mars seasonal duration 2

2.1 Dust properties in visible and infrared bands 20

2.2 Tri-modal size distribution in source modes [Zender at al., 2002] 32

2.3 Transport bins and sub-bin distribution parameters [Zender at al., 2002] 33

List of Figures

1.1 Mars orbit around the Sun in one Mars year from Ls = 0^0 to Ls = 360^0. The dashed line shown the position of perihelion (shortest Mars-Sun distance) ~ Ls = 71^0 and aphelion (longest Mars-Sun distance) ~ Ls = 251^0 2

1.2 Map of global topography of Mars [Smith et al., 1999] 4

1.3 Vertical structure of the Martian atmosphere. Colored curves are temperature inferred from deceleration measurements aboard the Viking 1 (blue), Viking 2 (green), and Pathfinder (red) landers [Haberle, 1999]. 6

1.4 Mars global dust storm as observed by Hubble space telescope in 2001 9

1.5 Local dust storms in Promethei (38.4^0 S, 248^0 W). Arrows indicate areas of active dust-lifting. The image was taken by MARCI (600 nm filter) at a resolution of ~ 1 km/pixel 10

1.6 The dust devil activity observed by Mars Exploration Rover Spirit from the surface within Gusev crater (14.5° S 175.4° E) 12

2.1 The relationship between threshold friction velocity m/s to particle diameter in the range 5-450 μm when Reynolds number is less than 10 for Earth. The optimal size corresponds to the lowest threshold friction velocity therefore is about 75 μm with a

minimal threshold 0.21 m/s. 27

2.2 The same plot as Figure 2.1 but for Mars. Particle diameter is in the range 5-950 μm when Reynolds number is less than 10. The optimal size corresponds to the lowest threshold friction velocity therefore is about 110 μm with a minimal threshold 1.85 m/s. 28

3.1 Diurnal near surface temperature cycle (1.27 m above surface) at the 3th sol from MPF observations (plus symbols) and simulation (full line), surface temperature (dashed line) around $Ls141^0$ from simulation with dust optical depth ~0.3 [Savijarvi et al., 2004]..... 48

3.2 Simulated surface and near surface temperature (24 m above the surface) from 1-D model at the same time with simulated dust optical depth ~ 0.25..... 48

3.3 Vertical temperature profile from GEM-Mars 1-D model simulation at local solar time 0600,1000,1600, 2200 49

3.4 Vertical temperature profile from UH model simulation at local solar time 0600,1000,1600,2200 49

3.5 Same as Fig. 3.3 but for total (radiative+turbulent) heating rate (K/hr) 50

3.6 Same as Fig. 3.4 but for total (radiative+turbulent) heating rate (K/hr) 50

3.7 Same as Fig. 3.3 but for solar radiative heating rate (K/hr)..... 50

3.8 Same as Fig. 3.4 but for solar radiative heating rate (K/hr)..... 50

3.9 Same as Fig. 3.3 but for thermal long wave (CO_2+dust) radiative heating rate (K/hr) .. 50

3.10 Same as Fig. 3.4 but for thermal long wave (CO_2+dust) radiative heating rate (K/hr) .. 50

3.11 Same as Fig. 3.3 but for turbulent heating rate (K/hr) 51

3.12 Same as Fig. 3.4 but for turbulent heating rate (K/hr) 51

3.13 Dust optical depth from 1-D GEM-Mars for 120 sols at MPF lading site 19^0N and 33^0W (Ls = 81^0 - 141^0). 54

3.14 Dust optical depth from 3-D GEM-Mars for 5 sols (Ls = 141^0) at MPF lading stie 19^0 N and 33^0 W..... 54

3.15 Sensible heat flux from 1-D GEM-Mars for 5 sols (Ls = 141^0) at MPF lading stie 19^0N and 33^0W. 55

3.16 Near surface (~40 m above surface) wind speed from 1-D GEM-Mars for 5 sols (Ls = 141^0) at MPF lading stie 19^0N and 33^0W..... 55

3.17 Same as Figure 3.15 but from 3-D GEM-Mars. 55

3.18 Same as Figure 3.16 but from 3-D GEM-Mars 55

3.19 The diurnal surface heat budget simulated by GEM-Mars 1-D model for Phoenix landing site (680N, 234^0E) around Ls = 90^0 with geostrophic wind 32.5 m/s and dust optical depth ~ 0.3 at the sol 60 of the run: the net longwave heat flux (IR), the net shortwave (SW) heat flux, sensible heat flux, and ground heat flux for 1 sol (24 hours). 57

3.20 The diurnal surface heat budget simulated by Davy's 1-D model for the same location and time with dust optical depth ~ 0.3 58

3.21 The diurnal temperature profile for Phoenix landing site (68^0N, 234^0E) around Ls = 90^0 with geostrophic wind 32.5 m/s, and the dust optical depth ~ 0.3 at the sol 60 of the run. The surface and near air temperature (24 m above the surface) are plotted for 24 hours. 59

3.22 The diurnal surface temperature for the Phoenix landing site a ~ Ls = 90^0 with dust optical depth of 0.3, 0.5 1, and 5 59

3.23 The simulated diurnal surface and near air temperature by GEM-Mars 1-D model for Phoenix landing site at Ls = 90^0 with geostrophic wind 30 m/s and the dust optical depth ~ 0.175 at the sol 60 of the run. 60

3.24 Same as Figure 3.23 but with geostrophic wind 35 m/s and the dust optical depth ~ 0.5 at the sol 60 of the run. 61

4.1 Daytime zonal average column dust optical depth over three Mars years from GEM-Mars simulation. The simulated visible optical dust opacity is scaled to IR band by a factor of 2 ($\tau_{0.67\mu m}/ \tau_{9\mu m}$=2 [Forget, 1998]) and scaled to an equivalent 6.1 mbar pressure surface to remove the effect of topography. 64

4.2 Daytime zonal average column dust optical depth over 3.5 Mars years from THEMIS [Smith 2009]. The dust optical at 1075 cm^{-1} (9.35 μm) scaled to an equivalent 6.1 mbar pressure surface to remove the effect of topography. 64

4.3 Daytime zonal average air temperature at ~0.5mb(~25km above the surface) over three Mars years from GEM-Mars simulation. 65

4.4 Daytime zonal average air temperature at ~0.5mb (~25km above the surface) over 3.5 Mars years from THEMIS..... 65

4.5 Global average column dust optical depth from GEM-Mars for three Mars years 68

4.6 Observed global average dust optical depth from TES for Mars years 24, 25 and 26 .. 68

4.7 Simulated zonal average accumulated CO_2 ice (kg/m^2) within three Mars years 70

4.8 Simulated zonal average surface pressure (mbar) within three Mars years 71

4.9 Global average surface pressure from GEM-Mars for three Mars years..... 71

4.10 The snapshots surface dust column optical depth in the visible wavelength 0.63 μm at four seasons Ls = 90^0 (top left), 180^0 (top right), 270^0 (bottom left), 360^0 (bottom right) for the second simulated year. The local noon is around longitude 30^0 E. The background gray contours stands for the topography. 73

4.11 The snapshots surface temperature at the same time as Figure 4.10. 74

4.12 A snapshot of near surface winds for Ls = 270^0 (same time as bottom left panel in Figure 4.11) for the second simulated Mars year, local noon is around longitude 30^0 E. Topography is shaded in colors with grey is highest and decreases from red to yellow. 75

4.13 Snapshots for threshold friction velocity for saltation (top left), deposited CO_2 ice (top right), surface friction velocity (bottom left), and the wind magnitude of near surface wind (bottom right) with local noon at 30^0 E for Ls = 270^0. The topography is plotted as grey contours. 76

4.14 The snapshots of dust optical depths for constant saltation friction velocity thresholds (A and C 1.7m/s; B and D 1.2 m/s); for variable saltation thresholds with inject tuning parameter (2×10^{-3} for E and G; 7×10^{-5} for F and H). A, C, E, and G at Ls = 90^0; B, D, F and H at Ls = 270^0..... 76

4.15 (Left) simulated vertical dust optical depth at local noon around Ls = 270^0 located at 35^0 S, 65^0 E (northwestern rim of Hellas) with dust optical depth about 0.98; (Right) prescribed dust optical depth with dust optical depth 0.98 at the surface. 82

4.16 (Left) Scaled simulated dust mass mixing ratio for all four dust bins at the same time

and location as Figure 4.15, dust mixing ration is divided by 1.1254e-5 so that the surface dust mass mixing ratio is scaled to 1 ; (Right) prescribed scaled dust mass mixing ratio 83

4.17 The $\log_{10}$ of zonal average and time average of density-scaled dust opacity per unit height (m^2/kg) for the 2nd simulated year (top left) and 3rd simulated year (middle left) versus MCS retrieved data (bottom left) which is at 463 cm^{-1} (wavelength 21.6 μm); zonal average and time average air temperature for the 2nd simulated year (top right) and 3rd simulated year (middle right) versus MCS retrieved data (bottom right). The vertical axis is altitude in km. Time average is taking the day and night between Ls = 89.5^0 to Ls = 90.5^0 for MCS observations around June 2008 and the second and third year for GEM-Mars. In the bottom panels the white space at low altitude is missing data in the MCS retrieval..... 85

4.18 Same as Figure 4.17 but for Ls = 269.5^0 to Ls = 270.5^0..... 86

4.19 Same as Figure 4.17 but for Ls = 359.5^0 to Ls = 0.5^0..... 88

4.20 Same as Figure 4.17 but for Ls = 179.5^0 to Ls = 180.5^0..... 90

4.21 Atmospheric dust optical depth measurements obtained from Phoenix Lander's Surface Stereoscopic Imager (SSI) of the Sun at wavelengths of 451 nm for Mars Year 29 and simulated dust optical depth for three Mars years 93

4.22 Dust extinction coefficient and density-scaled extinction coefficient retrieved at wavelength 523nm on mission sol 48 ~ Ls = 98.3^0 (Left, cited from Komguem et al. [2013]) simulated (Right) at Ls = 98.3^0 for three Mars years. 94

4.23 Comparison of retrieved temperature (left), pressure (right top), and density (right

bottom) profiles from Phoenix entry datasets with GEM-Mars simulations for three Martian years at landing location 68.22^0 N, 234.25^0 E around Ls = 76.73^0 96

4.24 Comparison retrieved temperature from MET at 0.25 m,0.5 m, and 1 m with surface temperature from GEM-Mars third year simulation at Phoenix landing location 68.22^0 N, 234.25^0 E around Ls = 105^0 98

4.25 The cross section with topography along longitude 125^0W (Phoenix lander at 68.22^0N) for air temperature in K (top left), wind magnitude in m/s (top right), dust opacity (bottom left) and density scaled dust opacity (bottom right) at third Mars year Ls = 90^0 from GEM-Mars. The vertical axis is altitude in km. 99

4.26 Latitude–height cross section of zonal mean atmospheric temperature (K), zonal wind (m/s), meridional wind (m/s), vertical wind (m/s) and mass streamfunction (10^9 kg/s) from the top panel to the bottom in sequence. Left column for Ls = 90^0 and right column Ls = 270^0. The vertical axis is altitude in km. 103

4.27 Latitude–height cross section of zonal mean atmospheric temperature (K), zonal wind (m/s), meridional wind (m/s), vertical wind (m/s) and mass streamfunction (10^9 kg/s) from the top panel to the bottom in sequence. Left column for Ls = 0^0 and right column Ls = 180^0. The vertical axis is altitude in km. 106

4.28 Latitude–height cross section of zonal mean atmospheric temperature (K), left column for Ls = 90^0 and right column Ls = 270^0, clear atmosphere top panel, dusty atmosphere (middle), the difference between dusty and clear atmosphere (bottom). The vertical axis is altitude in unit km. 107

4.29 Latitude–height cross section of zonal mean atmospheric zonal wind (m/s), left

column for Ls = 90^0 and right column Ls = 270^0, clear atmosphere top panel, dusty atmosphere (middle), the difference between dusty and clear atmosphere (bottom). The vertical axis is altitude in unit km. 108

4.30 Latitude–height cross section of zonal mean atmospheric mass streamfunction (10^9 kg/s), left column for Ls=90^0 and right column Ls=270^0, clear atmosphere top panel, dusty atmosphere (middle), the difference between dusty and clear atmosphere temperature (bottom). The vertical axis is altitude in unit km. 109

Chapter 1 Introduction

1.1 Overview of Mars

Mars is the fourth planet from the Sun in our solar system. The average distance from Mars to Sun is about 1.5 AU (astronomical Unit, 1AU = 1.496×10^{11}) which is 0.5 AU longer than that of Earth and Sun distance. Similar to Earth, Mars has four seasons because the axial tilt of Mars is around 25.19^0 while Earth's axial tilt is about 23.4^0. The Martian orbital eccentricity is about 0.09 which is larger than that of Earth, 0.0167, and means that the orbit of Mars is more elliptical than the orbit of Earth, and results in the unequal lengths of the four seasons on Mars. The seasons on Mars are referred to in term of the solar longitude Ls, the Mars-Sun angle, measured from the Northern Hemisphere spring equinox where Ls = 0^0. Thus Ls = 90^0 corresponds to summer solstice, Ls = 180^0 the autumn equinox and Ls = 270^0 the winter solstice for the northern hemisphere. Table 1 shows the range of Mars seasons in terms of Ls and the lengths of seasons in terms of Mars' sols. A Mars' sol is referred to a sidereal day and has an average length of 88775.244 seconds, or equivalently 24 hours 39 minutes 35.244 seconds, and a Martian year is 668.6 sols long (~ 687 Earth days, about twice the 365-day Earth year). Figure 1.1 illustrates the Mars orbit in one Mars

year from Ls = 0^0 to Ls = 360^0. The Mars orbital parameters described above affect the locations and the amount of incoming insolation at the top of the Mars atmosphere.

Table 1.1: Mars seasonal duration

Ls ^{0}	Seasons for Northern Hemisphere	Length (sols)
0-90	Spring	194
90 -180	Summer	178
180-270	Fall	143
270-360	Winter	154

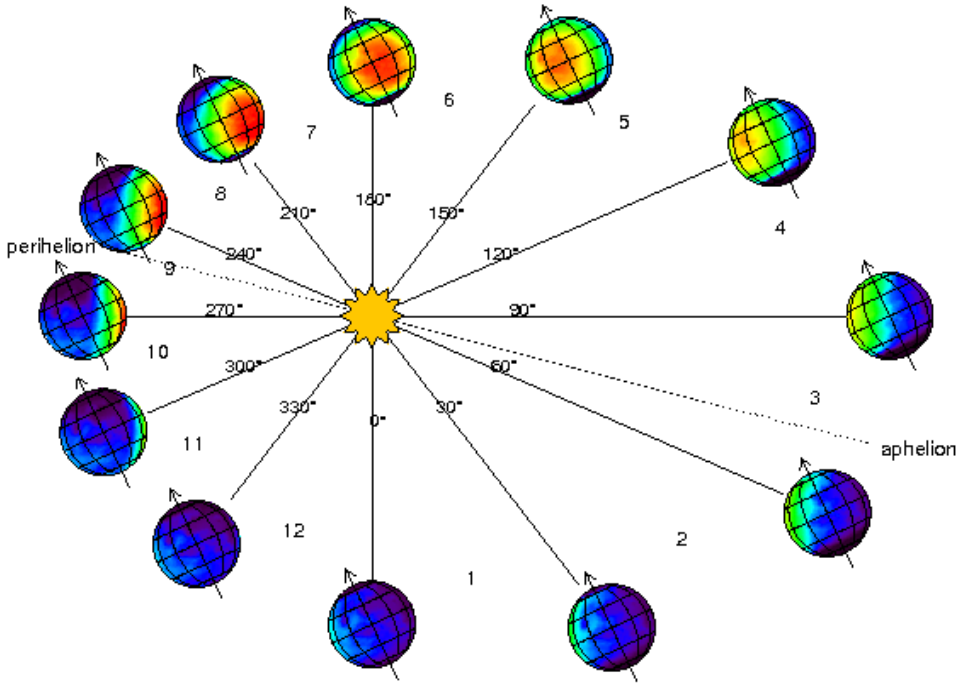

Figure 1.1: Mars orbit around the Sun in one Mars year from Ls = 0^0 to Ls = 360^0. The dashed line shown the position of perihelion (shortest Mars-Sun distance) ~ Ls = 71^0 and aphelion (longest Mars-Sun distance) ~ Ls = 251^0. Cited from [http://www-mars.lmd.jussieu.fr/mars/time/solar_longitude.html].

Similarly to Earth, one Martian year can be divided into 12 months (one month = 30 degrees in Ls), and one Mars sol into 24 hours. To distinguish between multi-year Mars observation, we will use the designation by Clancy et al [2000] of "Mars Year 1" beginning on 11 April 1955, consecutively, MY (Mars Year) 24 beginning 14 July 1998, MY 25 beginning 31 May 2000, MY 26 beginning 18 April 2002, and MY 27 beginning 5 March 2004. In our model local true solar time is related to the position of the sun in the sky so that local true solar time noon occurs when the sun is highest in the sky and Martian season is represented in degrees past northern spring equinox. We adopted the same time definition as the Mars Climate database maintained by Laboratory of Dynamic Meteorology (LMD).

1.2 Mars topography

Mars is much smaller than Earth in terms of size and mass. The radius of Mars is about half of Earth's radius, and the total volume of Mars is around 15% of Earth's volume. The total mass of Mars is about 11% of the mass of Earth, and it is less dense than Earth. The gravity at the surface of Mars is about 3.69 m/s^2, roughly 1/3 of Earth's surface gravity. The surface of Mars is dry and there is no liquid water existed on the surface because of low atmosphere pressure and cold temperature. Most of surface is deeply covered by finely grained iron oxide dust so Mars appears with a reddish color.

The major differences between north and south hemisphere measured by MOLA (Mars Orbiter Laser Altimeter) are that terrain appears in younger and more lightly cratered, flat and smooth in northern hemisphere, whereas that in the southern hemisphere is old and heavily cratered, with rougher plains than the northern plains. The dominant feature of the

topography is the striking (~5 km) elevation difference, relative to a zero geopotential, between the low northern hemisphere and high southern hemisphere measured by MOLA as seen in Fig. 1.2. This difference results in the average surface pressure of northern hemisphere 3.8 mbar higher than the southern hemisphere if we take the global average pressure 6 mbar and an atmospheric scale height 10.8 km.

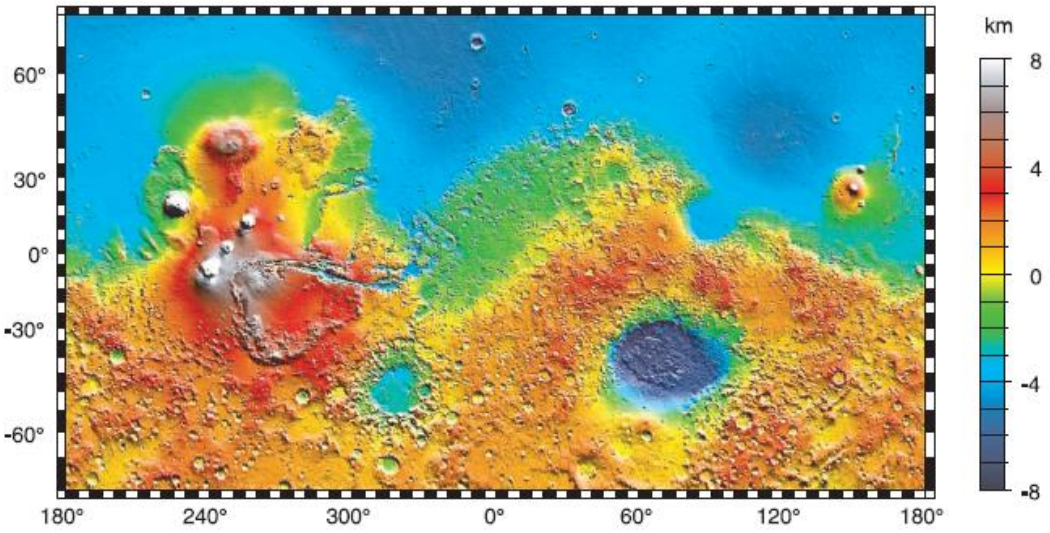

Figure 1.2: Map of global topography of Mars [Smith et al., 1999]

There are ice caps on both poles. The ice caps are composed of both water ice and CO_2 ice. About 25-30% of the CO_2 in the atmosphere is involved in the CO_2 cycle on Mars. That is CO_2 gas condenses and deposits on the polar regions during their wintertime and CO_2 ice sublimates back to the atmosphere during the summertime. Due to the longer wintertime in the southern hemisphere the southern polar ice cap covers a larger area than that of North polar ice, and it can reach as farther as southern latitude 60^0 during the southern winter. The maximum solar insolation arriving at Mars at perihelion (the smallest Mars-Sun

distance) around Ls = 251^0 during northern hemisphere winter, results in the south polar ice cap is shallower in depth than north polar cap.

1.3 Atmosphere of Mars

Martian atmosphere is composed of four regions, the Lower Atmosphere, Middle Atmosphere (Mesosphere), Upper Atmosphere (Thermosphere) and the Exosphere. Figure 1.3 illustrates the variation of temperature with height. Note that Mars does not have a stratosphere due to the lack of an ozone layer. The Lower Atmosphere known as Troposphere (<60 km) is warm because it is affected by the heat from the ground and from airborne dust and temperature decreases with height. In the Middle Atmosphere known as Mesosphere (60~120 km), temperatures become nearly constant, but oscillations due to the adiabatic heating and cooling associated with vertically propagating planetary waves are superimposed on this constant structure. The Upper Atmosphere (120~220 km) is also known as the Thermosphere where the temperature is very high because of heating from the sun and gasses in this part of the atmosphere separate. The Exosphere (>220 km) is where Mars atmosphere stops and space begins.

The Mars atmosphere is relatively low humidity, low atmospheric pressure, low temperatures comparing to Earth, it is enable to produce strong wind to cause the local dust storms for several sols and occasional planet-wide dust storms to obscure the surface for months at a time. Because of low gravity (~1/3 of Earth gravity) the dust particles (diameters in the order of 0.01-10 μm) could keep suspended in atmosphere for longer periods of time than in Earth atmosphere. The planet equilibrium temperature on Mars is

about 210 K, and the mean surface temperature is about 215 K [Carr and Head, 2010], so results in a relatively weak greenhouse effect about 5 K comparing to a mild greenhouse effect ~33 K warming on Earth.

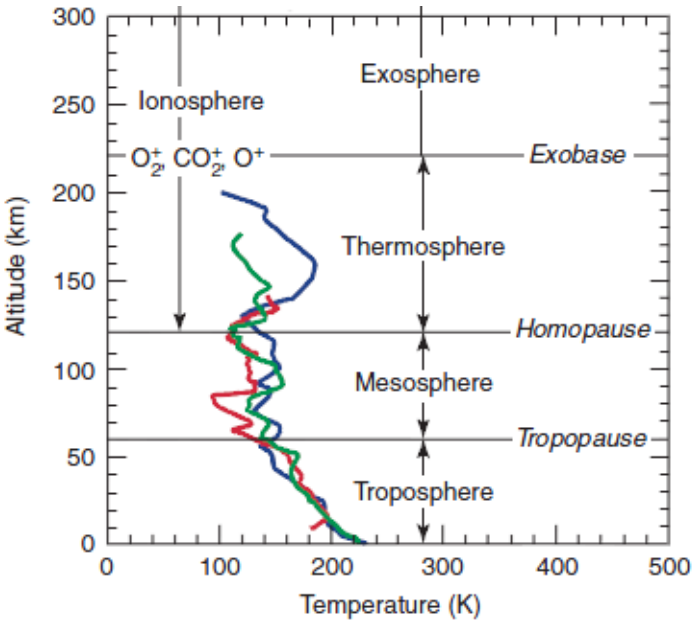

Figure 1.3: Vertical structure of the Martian atmosphere. Colored curves are temperature inferred from deceleration measurements aboard the Viking 1 (blue), Viking 2 (green), and Pathfinder (red) landers [Haberle, 1999].

The Martian atmosphere is about 100 times less dense than that of Earth and it consists of roughly 95.97% CO_2, 1.89% N_2, 1.93% Ar (argon), 0.146% O_2 by volume, and the remaining percentages making up traces of water vapor, methane and so on. Water ice clouds have been observed exist in all Martian seasons [Smith, 2013]. The average surface air pressure on Mars is about 6-7 mb (less than 1% of the Earth's), though it varies greatly with altitude from about 13 millibars in the deepest basins to about 0.2 mb at the top of

Olympus Mons, the highest point on Mars. Although during the summer daytime the surface temperature at low latitudes can be significantly above water freezing point (273.15 K), the atmospheric pressure is so low that water ice turns directly into water vapor without first becoming liquid. A minor variable abundance (0.03% volume) of water vapor has been detected in the Martian atmosphere. NASA detected methane in Martian atmosphere through telescopes spectral features of the gas in 2009. The recent detection of trace amounts of methane and possibly also of ammonia could indicate the presence of life on Mars, although there are other ways of explaining these gases.

The troposphere on Mars is deep by comparison to Earth. Based on Viking and Pathfinder lander entry measurements, the troposphere on Mars extends to almost 60 km with an average lapse rate of ~2.5 K/km. On Earth, the troposphere is about 12 km deep, and the lapse rate is ~ 6.5 K/km [Haberle, 1999]. For Earth, the reason that the observed lapse rate is less than the dry adiabatic lapse rate (~9.8 K/km) is due to latent heat release associated with the condensation of water vapor. For Mars, the additional heating comes from the absorption of solar radiation by suspended dust particles can explain why the observed lapses rate is much less than the dry adiabatic lapse rate is ~4.3 K/km [Haberle, 1999]. The theoretical daytime boundary layer convection could extend to very high altitudes about 15 km on Mars. Above 15 km, temperatures continue to decrease with height and controlled almost by radiation rather than convection. In Figure 1.3 the Viking lander 1 entry profile shows a near dry adiabatic lapse rate from the surface up to 6 km indicating a daytime convection in such region where the lapse rates should be close to the adiabatic value.

1.4 Dust storms on Mars

Dust plays important role analogous to the role of water vapor on Earth. Global dust storms are planetary-scale and can last for many sols, the duration may vary from 35 to 70 sols or more, and the dust optical depth during the global dust storm is greater than 1. The optical depth is referred as the total column optical depth which is the total mass of the radiation absorber times the absorption cross section. The large regional (area $>1.6\times10^6$ km^2) or global Mars dust storms have been observed from ground-based observations for over a century. But these observations are limited in spatial and temporal resolution. Spacecraft observations in the 1970s gave us the high-resolution images of the Mars surface and local (area $>10^2$ km^2), regional and global dust activity. In 2001 NASA's Hubble Space Telescope saw the biggest storm ever seen in the past several decades as shown in Figure 1.4. The seeds of the storm were caught brewing in the giant Hellas Basin in June, 2001 and in another storm at the northern polar cap as seen in the left of Figure 1.4. In early September, the storm had already been raging across the planet for nearly two months obscuring all surface features as seen in the right of Figure 1.4. The fine airborne dust blocks a significant amount of sunlight from reaching the Martian surface [Bell et al., 2001].

The local dust storms are less intense, and form and dissipate in a few days or less. Local dust storms have observed to occur most frequently in the approximately latitude belts 10^0 to 20^0 N and 20^0 to 40^0 S, with more dust clouds seen in the south than in the north, the majority of which occurred during southern spring [Appelbaum et al., 1989]. When dust storms are not present, the dust optical depth is typically about 0.5 from the

observations of Viking lander I (landing site 22.3^0 N, 47.9^0 W) and II (landing site 47.7^0 N, 225.7^0 W) [Appelbaum et al., 1989].

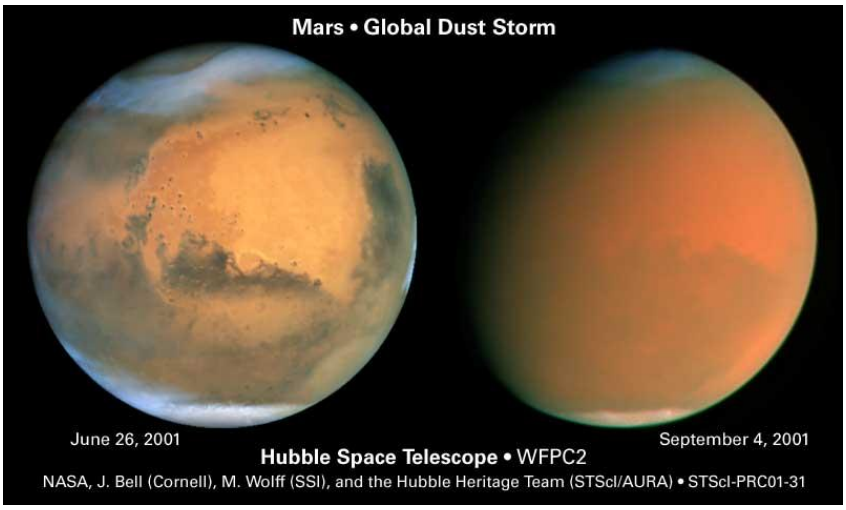

Figure 1.4: Mars global dust storm as observed by Hubble space telescope in 2001 [Bell et al., 2001]

With the help of the high-resolution and continual spacecraft observations we can see the local dust storm in details. The Mars Color Imager (MARCI) on-board the Mars Reconnaissance Orbiter (MRO) continues the daily global observations of Mars made by the Mars Global Surveyor (MGS) Mars Orbiter Camera (MOC) Wide-Angle Camera (WA) and provides the higher spatial resolution. MARCI is able to capture the location of dust sources-areas where dust is actually lifted from the surface to create any observed dust storm. In Figure 1.5 a local dust storms in Promethei (38.4^0 S, 248^0 W) was imaged by MARCI. This location is close to the receding seasonal south polar cap edge. The arrows in Figure 1.5 are indicators of area of active dust-lifting in the storm [Malin et al., 2007]. After dust is lifted from the surface, faster winds at higher altitude move dust to the east and form dust clouds. Observations by MARCI confirm with previous observations that the fine

surface dust lofted by local storms can easily reach the altitude at which water vapor is saturated in the cold thin Martian atmosphere and act as the perfect nucleation sites for water ice. This is why water-ice clouds are commonly found above very convective dust storms.

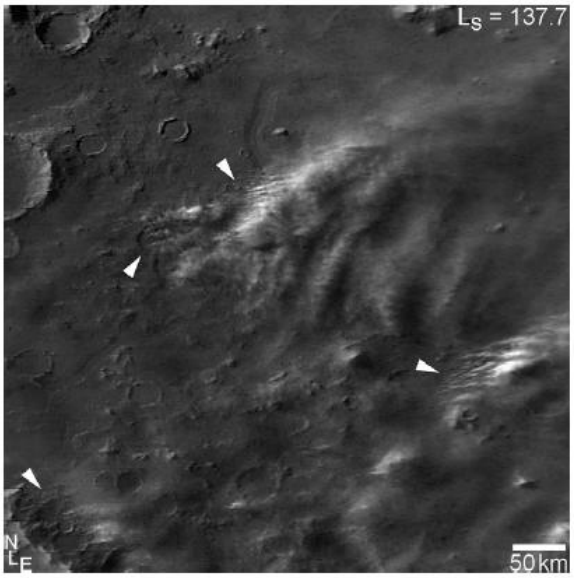

Figure 1.5: Local dust storms in Promethei (38.4^0 S, 248^0 W). Arrows indicate areas of active dust-lifting. The image was taken by MARCI (600 nm filter) at a resolution of ~ 1 km/pixel [Malin et al., 2007].

Dust devils are thermal driven vortices in the atmosphere that are common on Earth and Mars. Mars GCM models [Newman et al., 2002; Basu et al., 2004; Kahre et al., 2006] suggest that dust devils could lift significant dust from the surface and maintain the dust haze in the atmosphere. Dust devils are estimated to lift approximately half as much material as local and regional dust storms annually and are therefore significant contribution of dust into the Martian atmosphere [Whelley and Greeley, 2007]. Dust devil

does not appear to be controlled significantly by elevation, topographic slope, dust cover or surface physical properties [Whelley and Greeley, 2007]. More recently an entire Mars year of dust devil activity was observed from the surface within Gusev crater (14.5° S 175.4° E) as seen in Figure 1.6 [Greeley et al., 2006]. Orbital observations of active dust devils and dust devil tracks are documented in Mars Orbiter Camera (MOC), Thermal Emissions Imaging System (THEMIS), and High Resolution Stereo Camera (HRSC) images, and dust devils and their tracks have been observed in many regions of Mars. Dust devils tracks tend to fade with time, which is attributed either to the deposition of dust or the removal of dust adjacent to the dust devil track [Balme et al., 2003; Fisher et al., 2005].

On Mars the global dust storms do not appear every year, and, when they occur neither the same size nor begin at exactly the same time each year. The reasons of the interannual variability of global dust storms are not totally understood yet, there are many hypotheses for triggering global dust storms. One hypothesis relates to the non-linear dust radiative feedback which dependents of the amount of atmospheric dust loading and the dust distribution [Lemmon, 2014], others may relate to the superposition of the Hadley cell circulation, the planetary-scale topographic winds, and the thermal tide [Leovy et al., 1973]. The 1999 cross-equatorial mass dust loading suggests that the southern hemisphere subtropical latitudes require at least 2-3 Mars year to replenish their dust sources before global storms can form [Cantor et al., 2001]. Pankine and Ingersoll [2002] proposed that stochastic resonance due to prescribed weather noise was responsible for the triggering of these global storms, furthermore, the boundary conditions, such as albedo or surface dust reservoir also are the reasons to trigger global dust storms [Basu, 2006].

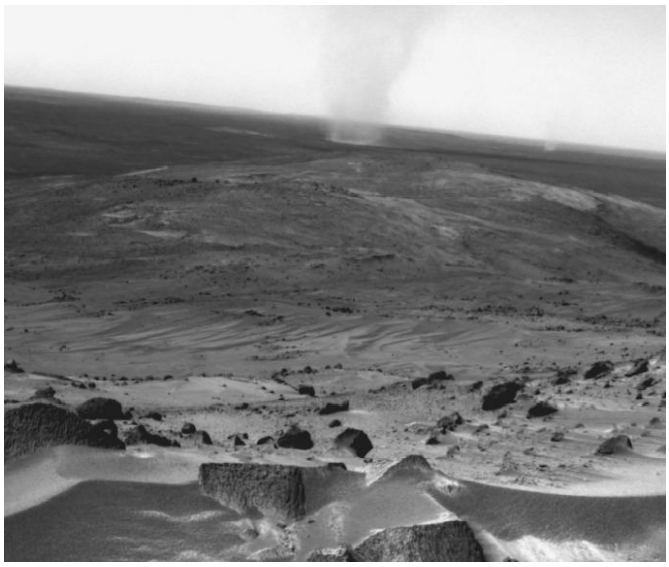

Figure 1.6: The dust devil activity observed by Mars Exploration Rover Spirit from the surface within Gusev crater (14.5° S 175.4° E) [Greeley et al., 2006]

The Mars surface temperature, surface column dust and water ice optical depth have been retrieved by TES (Thermal Emission Spectrometer) and show that during the aphelion season (Ls = 0^0 - 180^0) the Martian atmosphere is relatively cool, more water ice clouds, less dust in the air, and the atmosphere is relatively clear; in the perihelion season (Ls = 180^0-360^0) the Martian atmosphere is warmer, dusty, and has less water ice clouds [Smith, 2004]. The limb measurements of MCS (Mars Climate Sounder) and CRISM (Compact Reconnaissance Imaging Spectrometer for Mars) have retrieved vertical thermal structure of the atmosphere and vertical distribution of dust and water ice aerosols. These observations show that dust typically can extend to higher altitudes (~40–50 km) during the perihelion season than during the aphelion season (< 20 km), and the Hellas region consistently shows more dust mixed to higher altitudes than other locations [Smith, 2013].

Detached water ice clouds are common, and water ice aerosols are observed to cap the dust layer in all seasons [Smith, 2013].

1.5 Modeling the Martian dust cycle

In the previous Mars GCM, such as described by Forget et al. [1999], Kuroda et al. [2005, 2008], Hartogh et al. [2005], Moudden and McConnell [2005], Richardson et al. [2007], the dust mixing ratio is prescribed both in the horizontal and in the vertical and the dust is not transported by model winds. Newman [2002] firstly developed a radiatively active dust cycle including dust lifting, advection by the model winds, atmospheric mixing, and gravitation sedimentation by using the AOPP-LMD Mars general circulation model, which is developed by Atmospheric, Oceanic and Planetary Physics, Oxford University and Laboratory of Meteorology Dynamics, University Paris 6, and described fully by Forget et al., [1999]. But the self-consistent multi-annual dust cycles of Newman [2002] caused unrealistic high opacities and crashing the radiative transfer scheme.

The dust lifting initiated by near-surface wind stress and dust devils had been explored. Newman found that the results are dramatically affected by the use of a more threshold-sensitive parameterization. Haberle et al. [2003] addressed that the history of the three low thermal inertia regions by analyzing the pattern of model predicted wind stress lifting over a wide range of obliquity, but the model did not include dust devil lifting, dust transport, and deposition. Basu et al. [2004] used the Geophysical Fluid Dynamics Laboratory (GFDL) GCM to study dust injection by dust devils and model resolved wind stresses, size-dependent dust settling, transport by large-scale winds, and radiative heating

due to the predicted dust distribution. Basu et al. [2004, 2006] discovered that high-threshold wind stress lifting combining with the convective lifting, a "best fit" multiyear simulation, which produces a realistic thermal state, spontaneous and interannully variable global dust storms. Note that the high-threshold for wind stress lifting is a global constant. Kahre et al. [2006] employed the NASA Ames Mars GCM to investigate the dust lifting mechanisms responsible for the observed Martian dust cycle and the net surface response to the combined influence of dust lifting and deposition. But unlike Nasu [2004, 2006] Kahre [2006] didn't find the interannual variability of dust storms if such high thresholds were used. Newman and Richardson [2015] have investigated the impact of finite surface dust cover on the martian dust cycle simulated by the MarsWRF GCM, running with radiative active dust, parameterized dust lifting, and spontaneous dust storms. They found that re-tune the dust lifting parameters is necessary when using finite surface dust. This means that if a simulation is begun with uniform but limited surface dust and surface regions are allowed to deplete, then the best fit dust lifting parameters will change over time [Newman and Richardson 2015].

Previous GCM simulations find that it is relatively easy to independently simulate the correct weather conditions (in agreement with observations) for a particular season or location. What is difficult is a good global representation of the Martian dust cycle, which can be achieved only when all the interactions between various lifting schemes, the boundary layer phenomena and the radiative dynamical feedback are formulated accurately [Basu, 2006]. There are two schemes to lift dust from the surface: the first represents small-scale, convective lifting (dust devils) and relates the injection rate to the sensible heat

flux and boundary layer depth (following Newman et al. [2002]); the second scheme relates dust injection to the wind shear generated by model-resolved winds. The convective scheme is found unable to generate a dust storm, from which it is concluded that dust devils do not initiate dust storms, in agreement with the conclusion reached by Cantor et al. [1999] based on MOC imagery. Coarse particles (10μm-100μm) will settle out of the Martian atmosphere rapidly. Once fine dust (1-10μm) is raised into the atmosphere, it may stay suspended from less than a single Martian day to over 150 sols for global dust storms [Cantor et. al., 1999]. This suggests that the local dust storms that have been observed to disappear within one diurnal cycle are probably composed of course-grained particles (10μm-100μm) [Cantor et. al., 1999].

1.6 The goals of this study and the structure of this thesis

The main goal of this study is to simulate a self-consistent multi-years steady state dust cycle using the Global Environmental Multiscale model (GEM) and the terrestrial dust model Dust Entrainment And Deposition (DEAD). As discussed in section 1.5, in the early research stage one would have to drive the Mars GCM model with a tuned opacity to reach an agreement with the observations, thereby losing its self-consistency. Recently, self-consistent dust cycles including active dust with both thermal and dynamic effects have been studied by several research groups. In these studies the dust lifting schemes by wind shears and dust devils are theoretically similar and depend on lifting thresholds. These thresholds are not reusable from one Mars GCM to another. DEAD model has been used to study the global distribution of windborne mineral dust on Earth and has been

evaluated in the model of Atmospheric Transport and Chemistry (MATCH) [Zender 2002], in the model GEOS-chem (Goddard Earth Observing System) which is 3-D atmospheric chemistry model driven by assimilated meteorological observations from GEOS by Zhang et al. [2013], as well as in the model GEM-AQ (Global Environmental Multiscale model with Air Quality processes) by Wu [2010]. The study provides the details of the dust lifting parameters and proves that DEAD model with variable lifting threshold is suitable to the dust entrainment and deposition processes for Mars. The major work of this study focusses the development of the 3-D GEM-Mars, which is based on the dynamics of GEM and modified physics schemes. The updated GEM-Mars model is able to provide accurate radiative and dynamic feedback to the suspend dust in the Martian atmosphere. Thus the study goal could be fulfilled by adding DEAD model into GEM-Mars.

In Chapter 2 the detailed physics scheme including Dust Entrainment And Deposition (DEAD) model are described. A one dimensional GEM-Mars model was built to test all the physics schemes. In Chapter 3 the sensitive tests of radiation, two dust lifting schemes, and surface heat budget have been discussed. The same codes were transferred into the physical packages of GEM-Mars 3D model after 1-D tests were successfully. In Chapter 4 three Mars year dust and CO_2 cycle have been presented and compared with observations. The differences between the simulations and observations as well as the failure of interannual variability of global dust storms are explained in section 4.3, 4.4 and 4.5. The further exploration of the dynamic atmospheric circulations and the impacts of dust on the thermal and dynamics of Martian atmosphere are addressed in section 4.6 and 4.7 respectively. Finally Chapter 5 gives the summary of this study and future improvements.

Chapter 2 The Description of Global Mars Model: GEM-Mars (YorkU)

The Mars atmosphere General Circulation Model (GCM) GEM-Mars developed at York University has been used to simulate the dust cycle on Mars. The dynamic core is based on the Canadian operational weather forecast Global Environmental Multiscale NWP Model (GEM 3.3.0). The physics parts are modified based on the model GM3 developed by Moudden and McConnell [2005] and Akingunola [2008]. Both dust devils and wind shear lifting schemes are included in the model. The wind shear scheme is modified from terrestrial Dust Entrainment And Deposition (DEAD) model. The dust lifting processes are self-consistently determined by the resolved surface friction velocity and the surface sensible heat flux. This study has explored the two dust lifting schemes and dust radiative effects.

The physical schemes and GEM dynamics are described respectively in the following sections. In the current GEM-Mars model there are modified radiation, surface, vertical diffusion, dust lifting and deposition and CO_2 condensation schemes.

2.1 Dust Solar radiation: Delat-Eddington and two-stream approximation

The absorption and scattering of solar radiation by the dust is based on the CCM2 model (NCAR Community Climate Model version 2) two-stream Delta-Eddington solar radiation scheme. The two-stream Eddington approximation solution for the radiative transfer in planetary atmospheres is computationally efficient and therefore often used in climate models. The two stream approximation is applied to the calculation of the radiative transfer equations in two directions, i.e. upward and downward. In the model, the vertical column is divided into multiple layers. The solar radiation flux coming from the top of the atmosphere is transferred downward to the surface and is absorbed and scattered by the dust in each vertical layer. The reflectivity and transmissivity are calculated using the Delta-Eddington solution in each vertical layer and then the solar radiation flux is calculated at the interface of each layer in upward and downward directions.

Since the scattering by atmospheric aerosols has a strong forward diffraction peak isotropic scattering is not adequate and the Eddington approximation is replaced by the Delta-Eddington approximation where a delta-function adjustment replaces a highly peaked phase function (the angular distribution of the scattered energy as a function of the scattered angle [Liou, 2002]) with a delta function in the forward direction and a smoother, scaled phase function.

Appendix A shows the detailed calculation of the layer reflectivity and transmisivity to direct solar radiation and to the diffuse radiation, and the expressions of reflectivity and

transmissivity for two combined layers with the direct and diffuse radiation incident from the above. For the computation efficiency, the solar radiation is divided into two wide bands 0.1-0.5 μm and 0.5-5 μm and the single-scattering albedo and asymmetry factor for each band are shown in Table 2.1.

2.2 Dust IR radiation transfer

The scattering of the thermal infrared radiation by gases is not taken into account on Earth and Mars because of the strong isotropy of the radiation emitted by gaseous atmosphere. But the multiple scattering by dust outside the CO_2 15-μm band is not negligible on Mars, and it is important for weak bands (at the wings). The infrared spectrum outside the CO_2 15 μm band is divided into two wide bands as in Forget [1999] and previous Mars GCM GM3 9 μm silicate band (5-11.6 μm) and one for the rest of the IR (20-200 μm) as seen in Table 2.1. We adopt the ratio of 2 between the dust opacity in the visible bands and that in the infrared bands, i.e. τ(VIS)/τ(IR)=2. Other Mars GCMs developed by Forget et al. [1996] and Hartogh et al. [2005] also use this ratio value. The measurements of the dust optical depth made separately at solar and infrared wavelengths at the same time and location suggest a visible (0.67 μm) to infrared (9 μm) ration of about 2-2.5 [Martin, 1986; Clancy et al.1995]. The ratio value 2 works better because the longwave radiation doesn't consider dust opacity in the 15 micron band which is difficult to implement. We have increased our opacity to reflect the extra emissive capability of the 15 micron band that we are not calculating.

The two-stream Eddington approximation is applied to solve the radiative transfer equations as described by Toon [1989].

Table 2.1: Dust properties in visible and infrared bands

Wave length(μm)	single-scattering albedo ϖ	asymmetry factor g
0.1-0.5	0.665	0.819
0.5-5	0.927	0.648
5-11.6	0.470	0.528
20-200	0.370	0.362

2.3 CO_2 thermal infrared transfer

CO_2 absorption and emission theory in the 15um band (11.5-20 μm) is described by Hourdin [1992] and the code is modified from WRF planet-Mars. CO_2 15 μm band is divided into three wide bands: the central strongly absorbing part (14.2-15.7 μm), and two wings. The infrared emissivity algorithm is based on Garand [1983]. The infrared heating rate in the atmosphere due to the presence of an absorbing-emitting substance is given by Garand [1983],

$$q = \frac{\partial T(\sigma)}{\partial t} = \frac{g}{C_P P_s} n = \sum_{n=1}^{N} \frac{\partial F_n}{\partial \sigma} \tag{2.1}$$

where T is the air temperature, F_n is the net long wave radiation flux for the n^{th} spectral band, N is the total number of spectral bands, C_p is the specific heat of dry air at constant pressure, and g is the gravitational acceleration. For a non-scattering atmosphere

$$F_n(\sigma) = F_n \uparrow (\sigma) - F_n \downarrow (\sigma) \tag{2.2}$$

$$H_n(\sigma,\sigma') = \frac{\partial B_n}{\partial \sigma'}[T(\sigma')]\tau_n(\sigma,\sigma') \tag{2.3}$$

$$F_n \downarrow(\sigma) = -B_n[T(0)]\tau_n(0,\sigma) - \int_0^{\sigma} H_n(\sigma,\sigma')d\sigma' + B_n(\sigma) \tag{2.4}$$

$$F_n \uparrow(\sigma) = -(1-\varepsilon_{gn})B_n[T(1)]\tau_n(1,\sigma) + \int_{\sigma}^{1} H_n(\sigma,\sigma')d\sigma' + B_n(\sigma) \tag{2.5}$$

where $B_n[T(\sigma')]$ is the Planck function in flux integrated over the nth spectral band, $\tau_n(\sigma,\sigma')$ is the transmission function for the nth spectral band between level σ and σ', ε_{gn} is the ground emissivity for the nth spectral band. The transmission function is given in Hourdin [1992]. The code for the transmission function is modified from WRF planet, the final transmission function is the average of the three 15 μm band. The set of Pade coefficients vary with different temperature as given in Tables 3 and 4 in Hourdin [1992].

2.4 Non local thermodynamic equilibrium (non-LTE)

The non-LTE (local thermodynamic equilibrium) cooling is applied above approximately 80 km based on tabulated CO_2 cooling rates calculated by Lopez-Valverde et al. [1998] because above 50 km collisions become too infrequent to maintain the equilibrium. However, Bougher and Dickinson [1988] suggested that LTE holds up to about 90 km since the CO_2 15 μm band is sufficiently opaque. Lopez-Valverde et al. [1998] described a new non-LTE radiative transfer model for the CO and CO_2 infrared emissions in the Martian atmosphere. The code developed by Lopez-Valverde et al. has been inserted into GEM-Mars to provide CO_2 15 μm band cooling rate above 80 km.

2.5 UV-EUV heating

In the upper atmosphere, the main heating process is absorption of solar radiation in the ultraviolet (UV) and extreme ultraviolet (EUV) regions. The CO_2 15 μm band cooling (see section 2.4) at high altitude above 80 km approximately balances this UV-EUV heating and thermal vertical diffusion calculated by GEM (see section 2.10). We adopt the EUV-UV heating rate calculation described in Moudden [2005], which use a single band that covers the entire region, with solar flux of 1.2×10^{-5} $Wm^{-2}nm^{-1}$ and a cross section of 2.0×10^{-21} m^2. A more accurate representation will require the specification of several bands with a solar flux that may vary with the solar cycle.

2.6 CO_2 near-infrared absorption

CO_2 near-infrared absorption is negligible below 30 km but becomes considerable above 50 km. The absorption is added using a simple formula of heating rate which depends on pressure, Mars-Sun distance and solar zenithal angle [Forget 1999].

$$\frac{\partial T}{\partial t}(p,r,\mu) = \frac{\partial T}{\partial t}(p_0,r_0,0)\times\frac{r_0^2}{r^2}\sqrt{\frac{p_0}{p}\,\tilde{\mu}}\left(1+\frac{p_1}{p}\right)^{-b} \qquad (2.6)$$

With $p_1 = 0.0015889$ Pa, b=1.9628, and $\tilde{\mu}$ is the cosine of solar zenith angle μ corrected for the atmosphere refraction ($\tilde{\mu} = \left[\left(1224\mu^2+1\right)/1225\right]^{1/2}$). The cosine of solar zenith angle μ for a given location (lat, lon) on Mars is given by:

$$\mu(lat,lon) = \sin(lat)\sin(\delta_s) + \cos(lat)\cos(\delta_s)\cos(H) \qquad (2.7)$$

where δ_s is the solar declination angle in degrees and given below, Ls is the Mars orbital longitude angle discussed in section 1.1, and H is the local hour that depends on the

longitude.

$$\delta_s = sin^{-1}(0.4256\sin(L_s)) + 0.25\sin(L_s) \quad (2.8)$$

2.7 Dust thermal convection lifting scheme

Previous studies of the Martian dust cycle [Newman et al 2002, Basu et al. 2004] have taken into account two dust lifting mechanisms: mechanical processes (wind shear) and thermal convective processes (specifically, dust devils). They suggested that thermal convective processes can maintain the background dust haze, and the mechanical processes can trigger global and local dust storms.

A threshold-independent scheme is based on the thermodynamics of dust devils studied by Renno et al. [1998] and was first used in a GCM by Newman et al. [2002], and later was applied to the thermal convective dust lifting scheme in NASA Ames Mars GCM [Kahre et al., 2006]. The thermal convective process is treated as a heat engine and a scaling theory for dust devils which is described by Renno et al. in 1998. The dust devil activity defined as the flux of energy available to drive dust devils is given by $\Lambda \approx \eta F_s$, where η is the thermodynamic efficiency of the dust devil convective heat engine (the fraction of the input heat which is turned into work), and F_s is the surface sensible heat flux. The thermodynamic efficiency increases with the depth of the convective boundary layer, whereas the surface sensible heat flux increases with the surface to air temperature gradient [Newman et al., 2002].

Renno et al. [1998] have concluded that the intensity of a dust devil is a function of its thermodynamic efficiency and the input heat energy. For dry convective plumes, the heat

input is approximately equal to the sensible heat flux. The thermodynamic efficiency of the convective heat engine can be written as $\eta = \frac{T_h - T_c}{T_h}$ where T_h and T_c are, respectively, the entropy averaged temperatures of the heat source and sink. To a first approximation, the entropy of the convective boundary layer is constant with height. Thus, the entropy averaged temperature of the boundary layer air is equal to its pressure averaged temperature. It follows from the first law of thermodynamics that the temperature profile of a dry adiabatic layer is given by $T \approx \overline{T_s}\left(\frac{p}{p_s}\right)^{\chi}$. Integrating this temperature profile from the surface to the top of the convective layer, we get an expression for the temperature of the heat sink $T_c = \frac{\overline{T_s}\left(p_s^{\chi+1} - p_{top}^{\chi+1}\right)}{(p_s - p_{top})(\chi+1)} = b\overline{T_s}$ where p_s is the ambient surface pressure, p_{top} is the ambient pressure at the top of the convective boundary layer, $\chi = 0.25$ is the specific gas constant divided by the specific heat capacity at constant pressure, and b is defined as,

$$b = \frac{\left(P_s^{\chi+1} - P_{con}^{\chi+1}\right)}{(P_s - P_{con})(\chi+1)P_s^{\chi}} \tag{2.9}$$

The thermodynamic efficiency of a dry convective heat engine is given by $\eta \approx \frac{\overline{T_s} - b\overline{T_s}}{\overline{T_s}} \approx 1 - b$, which is a function of pressure thickness of the convective layer. This result is in agreement with observations of boundary layer convection and results of numerical simulations that show an increase in the intensity of convection with increase in the boundary layer thickness.

Newman et al. [2002] proposed a dust lifting flux rate defined as,

$$F_D = \alpha_D * F_s * \eta \tag{2.10}$$

F_D has a unit of ($kgm^{-2}s^{-1}$) Fs is the vertical sensible heat flux (Wm^{-2}), α_D is a tunable efficiency parameter with units of (kgJ^{-1}), and $\alpha_D = 2\times10^{-6}$ is applied in the code, and η is thermodynamic efficiency of the convective heat engine $\eta \approx 1 - b$ with b defined as in (2.9).

Equation (2.10) states that the dust devils lifting flux rate is proportional to the boundary layer thickness and the sensible heat flux. Thus dust is injected into the atmosphere whenever the lifting flux rate F_D is positive. The observations find that the peak in the dust devils occurrence at around 1300 local time is due to a peak in the surface heat input [Renno, 1998].

2.8 Dust mechanical lifting scheme-DEAD model

A mechanical dust lifting process is based on the terrestrial Dust Entrainment And Deposition (DEAD) model [Zender et al., 2002].The dust lifting in the DEAD model is based on mechanical processes. Due to the particle weight and the interparticle cohesive forces in the soil, the actual friction velocity u* has to exceed a threshold friction velocity U_t^* in order to lift a soil particle from the surface.

On Earth only small size particles (diameter < 60 um) can stay in the air for a long time and have the opportunity to go up to the upper atmosphere by turbulences and vertical motions. The threshold wind friction depends on particle size, particle density, air density, and kinematic viscosity of the air. The procedure to calculate the threshold is given by Marticorena et al. [1995], which B is defined as the friction Reynolds number,

$$B = \frac{U_t^* D_P}{\upsilon} \tag{2.11}$$

where D_P is the particle diameter, υ is the kinematic viscosity of the air. For 0.03 < B < 10,

$$U_t^*(D_P) = \frac{0.129K}{(1.928B^{0.092} - 1)^{0.5}} \tag{2.12}$$

for B > 10,

$$U_t^*(D_P) = 0.12K\left[1 - 0.0858\exp\left(-0.0617(B-10)\right)\right] \tag{2.13}$$

with $K = \left(\frac{\rho_P g D_P}{\rho_a}\right)^{0.5}\left(1 + \frac{0.006}{\rho_P g D_P^{2.5}}\right)^{0.5}$, where the factor 0.006 has the unit of $gcm^{0.5}s^{-2}$, other numbers and parameters are dimensionless, ρ_P is the particle density, ρ_a is the air density, and g is gravitational acceleration.

The kinematic viscosity of the air $\upsilon = \frac{\mu}{\rho_a}$, where μ is dynamics viscosity of air and is a function of temperature. The dynamics viscosity is calculated using Sutherland's formula:

$$\mu = \mu_0 \frac{T + C}{(T + C)}\left(\frac{T}{T_0}\right)^{3/2} \tag{2.14}$$

where μ_0 is the reference viscosity in (Pa·s) at reference temperature T_0. For earth T_0 = 293.15 K, $\mu_0 = 18.27\times10^{-6}$ P_a·s and C = 120 K; For Mars (about 96% air is CO_2) T_0 = 293.15 K, $\mu_0 = 14.8\times10^{-6}$ P_a·s and C = 240 K.

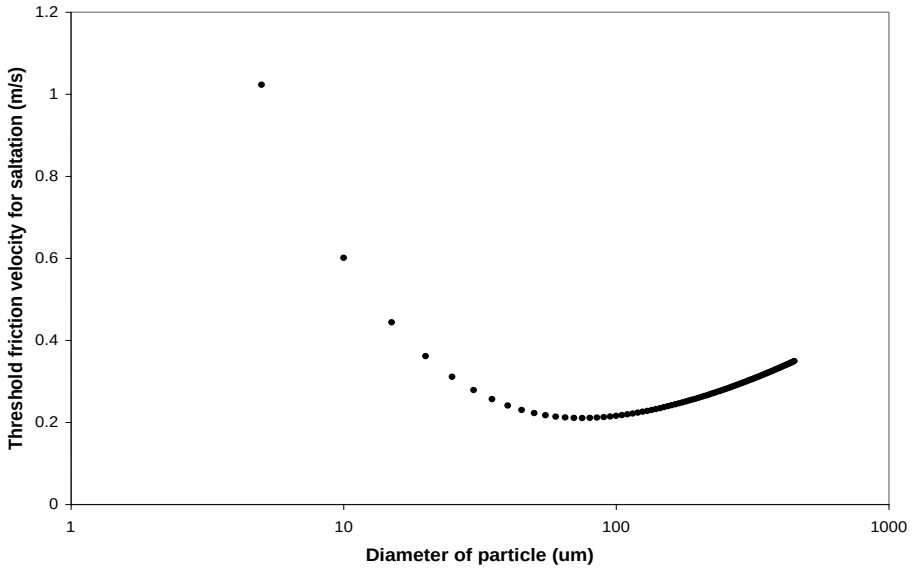

Figure 2.1: The relationship between threshold friction velocity m/s to particle diameter in the range 5-450 μm when Reynolds number is less than 10 for Earth. The optimal size corresponds to the lowest threshold friction velocity therefore is about 75 μm with a minimal threshold 0.21 m/s.

The threshold U_t^* can be solved by iteration using equations (2.11), (2.12) and (2.13). The relationship between U_t^* and the particle size is plotted in Figure 2.1 for Earth with particle size D_p in the range 5-450 μm, particle density 2650 kg/m3, air density 1.16 kg/m^3, ground temperature 291K. Figure 2.2 shows the same relationship for Mars D_p in the range 5-950 μm, particle density 2700 kg/m3, air density 0.012 kg/m^3, ground temperature 260 K.

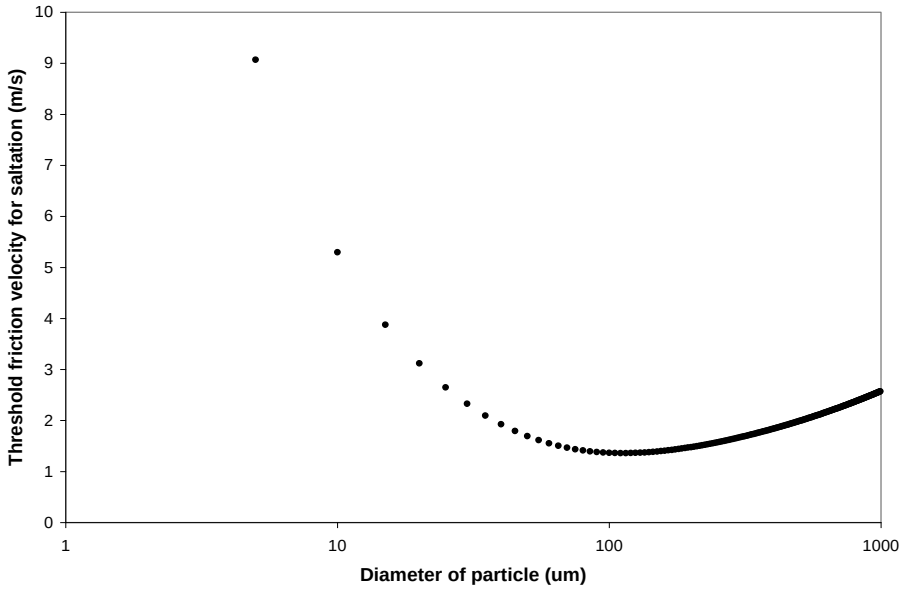

Figure 2.2: The same plot as Figure 2.1 but for Mars. Particle diameter is in the range 5-950 μm when Reynolds number is less than 10. The optimal size corresponds to the lowest threshold friction velocity therefore is about 110 μm with a minimal threshold 1.85 m/s.

There exists an optimal particle size for the minimal threshold. The threshold increases again beyond this optimal size. The optimal size is about 75 um for Earth and 110 um for Mars, corresponding with minimum threshold friction velocity 0.21 m/s and 1.85 m/s. For Mars when the ground temperature and air density vary from 233-260 K, 0.021-0.012 kg/m^3, the optimal size is about the same. Figure 2.1 and 2.2 illustrate that on Mars it is more difficult to lift particles from the surface.

2.8.1 Saltation processes and horizontal saltation mass flux

On Earth because of high threshold friction velocity U_t^* the direct lifting dust size particles (D_p < 60 μm) by near surface winds is negligible [Greeley and Iversen, 1985]. Similarly,

the same thing occurs on Mars. We know that the predominant particle size suspended in the Martian atmosphere is about the order of 1 μm. From figure 2.2 we can find that the threshold friction velocity is relatively high for small size particles. The threshold for diameter of 1 μm particle is 43.8 m/s, for 5 μm is 12.5 m/s. The typical mean wind in the neutral surface layer varies logarithmically with height, that is,

$$U(z) = \frac{U^*}{\kappa} \ln\left(\frac{z + z_0}{z_0}\right) \tag{2.15}$$

where $U(z)$ is the mean wind speed at the height z above the surface, z_0 is the surface roughness length (assuming $z_0 = 0.01$ m), and $\kappa = 0.4$ is the Von Karman's constant. It turns out that the near surface wind speed at 10 m would have to be as high as 757 m/s and 215 m/s in order to lift particles with diameter 1 μm and 5 μm directly from the surface. Under non-neutral situations (stable or unstable boundary layers), the wind profile deviates slightly from logarithmic in the neutral situation. Such wind speeds are unrealistic high. However, if we look at the large particles, such as 110 μm, which needs about 32 m/s wind speed at 10 m to lift up. So the results suggest that low threshold sand particles (diameter > 100 μm) saltate and can cause small particles to be injected into atmosphere. Since these large particles are two heavy to go up they will fall back on the surface. When they impact on the surface, they will disaggregate and eject small size particles by passing their momentum to them.

In the model we adopt the optimal sand size $D_p = 110$ um when friction velocity $u_* > u_t^*$, the horizontal saltation mass flux with a unit has a unit kg/m/s, is calculated using the formula of White [1979],

$$Q_s = \frac{c_s \rho u_*^3}{g}\left(1-\frac{u_t^*}{u_*}\right)\left(1+\frac{u_t^*}{u_*}\right)^2 \tag{2.16}$$

where c_s =2.61, ρ is the atmospheric density, u_* is the friction velocity, u_t^* is the threshold friction velocity for the optimal sand size.

2.8.2 Vertical dust mass flux and vertical diffusion

The vertical dust mass flux F_d is considered to be a fraction of the horizontal saltation mass flux Q_s in the DEAD model,

$$F_d = \alpha Q_s \tag{2.17}$$

where F_d has a unit $kgm^{-2}s^{-1}$, Q_s has a unit $kgm^{-1}s^{-1}$, and α is called the ratio of vertical dust flux to streamwise mass flux and has a unit m^{-1}. According to Marticorena et al. [1995], the fraction α is assumed independent of size and drag and can be calculated using an empirical formula which is derived from a linear fitting of measured data, and given by Marticorena et al. [1995] as

$$\alpha = 100exp\left[\left(13.4M_{clay} - 6.0\right)ln10\right] \tag{2.18}$$

where M_{clay} is the mass fraction of clay particles in the soil. The fraction α increases with M_{clay}, in the DEAD model for Earth $M_{clay} < 0.2$, so that $\alpha < 0.048$ m^{-1}. Since there is not enough information of M_{clay} on Mars, for simple, we assume a global uniform $M_{clay} = 0$, resulting in $\alpha = 10^{-4}$ m^{-1}.

In GEM-Mars dust is diffused vertically by the diffusion scheme of GEM. The diffusion scheme includes both local and non-local mixing, and the diffusion equation for a tracer C expresses as $\frac{\partial C}{\partial t} = \frac{\partial}{\partial z}\left[K_T\left(\frac{\partial C}{\partial z} - \gamma_{CG}\right)\right]$. The diffusion of dust depends on the

diffusion coefficient for heat and moisture K_T and countergradient term γ_{CG} which are described in section 2.10.

2.8.3 Dust particle size distributions

In the previous dust cycle modelings particle size distributions have been described using gamma distributions [Tomasko et al., 1999], modified gamma distributions [Toon et al., 1977], and lognormal distributions [Pollack et al., 1995]. Recent analysis indicates that the properties of airborne dust particles vary in space and time and have an effective radius ranging from 1.0 μm to 2.5 μm [Clancy et al., 2003; Wolff and Clancy, 2003]. The dust mass lifted from the surface in the model by the parameterizations described below is distributed in a lognormal particle size distribution that produces an average particle size of radius 1.5 μm. The dust particle size and shape is important for the radiative transfer calculation of the optical depth. This relationship between mass and optical depth changes as the suspended particle size distribution evolves.

DEAD uses a bin-method to independently transport discrete non-interacting, size (mass) classes. Within each transport bin, particles are assumed to have an analytic, time-invariant, sub-bin distribution. Each bin has an independently configurable sub-bin distribution which allows more accurate treatment of particle number and optical properties when the number of transport bins is small [Zender at al., 2002]. The number of transport bins limited only by the computational requirements of the model. Although the entrainment of mineral dust aerosol is initiated by the saltation of sand-size particles, only

particles with diameter less than 10 μm reside in the atmosphere long enough to travel significant distances downwind [Zender at al., 2002].

The vertical dust flux F_d obtained by equation (2.17) is assumed to be size-distributed in an analytic, tri-modal lognormal probability density function (PDF) which is globally uniform. The parameters of dust in the source modes are the number median diameter D_n, mass median diameter D_v, geometric standard deviation σ_g, and mass fraction M of each mode, and all the values are given in Table 2.2.

Table 2.2: Tri-modal size distribution in source modes [Zender at al., 2002]

D_n (μm)	D_v (μm)	σ_g (fraction)	M (fraction)
0.16	0.832	2.10	0.036
3.19	4.82	1.9	0.957
10.0	19.38	1.6	0.007

For the computational efficiency we adopt the default four dust din (J = 4), and employs the long range transport mode with D_v = 2.524 μm and σ_g = 2 for a normalized size distribution for sub-bin distribution. Since σ_g = 2 means long range transport, which is found to produce good agreement in visible optical depth with satellite observations, the modeled dust transport is the most realistic for the long range transport mode.

All time-independent size-varying properties (extinction, scavenging cross-sections, sedimentation velocities) are computed on a high resolution size grid, then weighted by the appropriate sub-bin distribution (surface area for extinction, volume for sedimentation), and then integrated to bin-mean values [Zender at al., 2002]. While the absolute mass in each bin changes every timestep due to size dependent source and sink processes (e.g.,

sedimentation), the assumed sub-bin distribution within each bin never changes. The bin-mean values shown in Table 2.3 is used in the DEAD model, for each size bin the minimum size $D_{min,}$ maximum size $D_{max,}$ volume median D_v, and geometric standard deviation σ_g of sub-bin distribution, specific (i.e., per unit mass) number N, surface area S, scattering Ψ_s, extinction Ψ_e, and mass fraction of entrained and transported dust M_j.

Table 2.3: Transport bins and sub-bin distribution parameters [Zender at al., 2002]

Bin	D_{min} (μm)	D_{max} (μm)	D_v (μm)	σ_g	N $\#kg^{-1}$	S m^2kg^{-1}	Ψ_s m^2kg^{-1}	Ψ_e m^2kg^{-1}	M_j %
1	0.1	1.0	2.524	2.0	3.484×10^{15}	3.464×10^{3}	2.834×10^{3}	2.893×10^{3}	3.2
2	1.0	2.5	2.524	2.0	2.138×10^{14}	1.471×10^{3}	7.779×10^{2}	8.350×10^{2}	17
3	2.5	5.0	2.524	2.0	2.205×10^{13}	7.107×10^{2}	3.343×10^{2}	3.825×10^{2}	41
4	5.0	10.0	2.524	2.0	3.165×10^{12}	3.741×10^{2}	1.705×10^{2}	1.961×10^{2}	38

2.8.4 Dust dry deposition

Dust dry deposition For the gravitational settling the DEAD model uses Stokes velocity u_{st} to approximate the terminal velocity v_g. The Stokes approximation is less time consuming but is limited to the transported particle size $0.1< D_p<10\mu m$. For Reynolds number $Re < 0.1$, the Stokes settling velocity is given,

$$u_{st} = \frac{D^2 \rho_P g C_c}{18\mu} \tag{2.19}$$

where μ is the dynamic viscosity of the air. The turbulent deposition in the DEAD uses the resistance-in-series method. The turbulent deposition velocity v_t is given,

$$v_t = \frac{1}{r_a + r_b + r_a r_b v_g} \tag{2.20}$$

where v_g is the terminal velocity r_a is the aerodynamic resistance of the constant flux layer and is independent of particle size, r_b is the quasi-laminar layer resistance and depends on the particle's properties and is expressed as,

$$r_b = \frac{1}{u_*(Sc^{-2/3} + 10^{-3/St})} \tag{2.21}$$

where the Schmidt number Sc accounts for Brownian diffusion and dominates for $D_P \leq 0.7\mu m$, the Stokes number St accounts for inertial impaction and dominates for $D_P \geq 5\mu m$.

After the vertical dust flux is obtained, dust is partitioned into four dust bins for vertical diffusion by GEM's vertical diffusion process and then for horizontal transport via the GEM dynamics subroutines. In our simulation, the long range transport mode has been employed with a volume median diameter 2.524 μm. The parameters for four transported dust bins and the sub-bin distribution are given in Table 2.3. The integrated dust optical depth of four dust bins is calculated at each vertical level using the sub-bin distribution parameters in Table 2.3 in the DEAD model at every time step.

2.9 Surface scheme: GEM force-restore method

We adopt the modified surface force-restore method described by Deardorff [1978] which is the one of the three options of GEM land surface processes. The force-restore method is an efficient time-dependent equation for predicting ground surface temperature. The

surface temperature is governed by the balance between incoming solar heat flux, downward thermal flux from the atmosphere, upward thermal flux from surface itself, and the turbulent flux. The net heat flux on the surface is given:

$$H_A = \epsilon_g \sigma T_g^4 + H_{sg} + L \cdot E_g - \left(1 - \propto_g\right) S^{\downarrow} - \epsilon_g {R_L}^{\downarrow} = -G \tag{2.22}$$

where H_A is the sum of the fluxes in the atmosphere at the ground (upward is positive), G is the net fluxes received at the ground (downward is positive), ϵ_g is the emissivity of the ground surface in the infrared, σ is the Stefan-Boltzman constant, H_{sg} is the sensible heat flux at the ground to the atmosphere, L is the latent heat of condensation, E_g is the evaporation rate from the soil surface, $\propto_g$ is the ground albedo, $S^{\downarrow}$is the magnitude of the shortwave radiative flux, and ${R_L}^{\downarrow}$ is the downward longwave radiative flux. The latent heat due to CO_2 condensation and sublimation is neglected in the simplified scheme. The sensible heat flux H_{sg} from the surface is produced by the turbulent heat flux in the boundary layer. $H_{sg} = \rho c_P \overline{w'\theta_s'}$ where ρ is the air density, c_P is the specific heat capacity at constant pressure, $\overline{w'\theta_s'}$ is the turbulent heat flux, w' and θ_s' are the turbulent parts of vertical velocity and surface penitential temperature respectively.

We chose the H_A forcing method to derive the ground temperature T_g:

$$\frac{\partial T_g}{\partial t} = \frac{-\sqrt{\pi} H_A}{\rho_s c_s d_1} \tag{2.23}$$

where $d_1 = (\kappa_s \tau_1)^{1/2}$ is proportional to the depth reached by the diurnal temperature wave, κ_s is the soil thermal diffusivity, τ_1 is a period of 1 Mars sol, τ_1 = 88775.244 seconds. The surface thermal inertia χ is defined as below and is known from the initial input $\chi = \rho_s c_s \kappa_s^{1/2}$

with a unit of ($Jm^{-2}s^{-1/2}K^{-1}$). So we can replace three unknown variables ρ_s, c_s, κ_s with χ. Then equation (2.23) become:

$$\frac{\partial T_g}{\partial t} = \frac{-\sqrt{\pi} H_A}{\chi \sqrt{\tau_1}} \tag{2.24}$$

The force-restore method gives a reasonable surface temperature response to the radiative forcing as we can see in section 3.1 that the simulated ground temperature is compared well with Mars Pathfinder measured ground temperature. A more sophisticated multilayer soil scheme would be more accurate and necessary for calculating the distribution of water in the regolith.

2.10 Vertical diffusion and boundary layer: GEM turbulence and diffusion

The treatment of eddy vertical diffusion in the Planetary Boundary Layer (PBL) rests on a time-dependent equation for the kinetic energy of turbulence (TKE) to describe turbulent processes [Benoit et al., 1989]. TKE is directly related to the momentum, heat, and moisture transport through the boundary layer, and is also sometimes used as a starting point for approximations of turbulent diffusion [Stull, 2009]. The definition of a mean TKE is presented as

$$E = 0.5(\overline{u'u'} + \overline{v'v'} + \overline{w'w'}) \tag{2.25}$$

where the kinetic energy of turbulence E has units m^2s^{-2}, u', v', and w' are turbulent parts of zonal, meridional and vertical winds respectively. The TKE budget equation is given from its definition that E is the sum of velocity variances divides by two. If we assume horizontal

homogeneity, and neglect the advection of E, then TKE budget equation is given [Stull, 2009]:

$$\frac{\partial E}{\partial t} = -\overline{\boldsymbol{V}'w'} \cdot \frac{\partial \boldsymbol{V}}{\partial z} + \frac{g}{\theta_{vs}} \overline{w'\theta_v'} - \frac{\partial}{\partial z}\left[\overline{w'\left(\frac{p'}{\rho} + E'\right)}\right] - \epsilon \qquad (2.26)$$

where **V** is the mean horizontal wind vector **V** = (u,v), θ_{vs} is the mean surface virtual potential temperature, θ_v' is the turbulent part of virtual potential temperature, w' is the turbulent part of vertical velocity, p' is the turbulent part of pressure, E' is the turbulent part of TKE, ρ is the mean air density, and ϵ represents the viscous dissipation of TKE, i.e., the conversion of TKE into heat. Turbulence is dissipative, this means that TKE is not a conserved quantity and it will trend to decrease and disappear with time, unless it can be generated locally or transported in by mean, turbulent, or pressure processes [Stull, 2009].

The first term on the right side of equation (2.26) is a mechanical or shear production/loss term, the second term is the buoyant production or consumption term, and the third term is the pressure-diffusion term. The closure relations of Tennekes and Lumley (1972) are used for the pressure-diffusion term

$$\overline{w'\left(\frac{p'}{\rho} + E'\right)} = -K_M \frac{\partial E}{\partial z} \qquad (2.27)$$

where K_M is the diffusion coefficient for momentum, and the expression for K_M is given by Kolmogorov [1942],

$$K_M = a\lambda E^{1/2} \qquad (2.28)$$

where λ is a turbulent length scale (or a mixing length), and a is a nondimensiional universal constant. The viscous dissipation term is parameterized as

$$\epsilon = c(\xi)E^{3/2},\ c = 0.14 + 0.56\xi \ \text{ with } 0 \le \xi \le 1. \qquad (2.29)$$

The approach is set to increase c up to 0.7 in the highly convective conditions relative to a basic value of 0.14 when the flow is stable or slightly unstable [Mailhot and Benoit, 1982].

Applying the first order closure approximation gradient transport theory or K-theory, we can parameterize the turbulent fluxes as

$$\overline{\boldsymbol{V}'w'} = -K_M \frac{\partial \boldsymbol{V}}{\partial z} \tag{2.30}$$

$$\overline{w'\theta_v'} = K_T \left(\frac{\partial \theta_v}{\partial z} - \gamma_{CG}\right) \tag{2.31}$$

where γ_{CG} is an imposed vertical potential temperature gradient in order to permit an upward "countergradient" heat flux under unstable conditions, $\gamma_{CG} = 0$ for stable case, and $\gamma_{CG} = \frac{b\left(\overline{\theta_v'w'}\right)_s}{w_* h}$ for unstable case, where b is on the order of 10, h is the height of the boundary layer, $\left(\overline{\theta_v'w'}\right)_s$ is the surface flux of θ_v and w_* is the boundary layer convective velocity scale defined by $w_*^3 = \frac{g}{\theta_{vs}}\left(\overline{\theta_v'w'}\right)_s h$. Typically, γ_{CG} is on the order of 10^{-3} Km^{-1} [Mailhot and Benoit, 1982].

If we combine TKE budget equation (2.26) with (2.27), (2.29), (2.30) and (2.31) then we obtain,

$$\frac{\partial E}{\partial t} = -K_M \frac{\partial \boldsymbol{V}}{\partial z} \cdot \frac{\partial \boldsymbol{V}}{\partial z} - K_T \frac{g}{\theta_{vs}}\left(\frac{\partial \theta_v}{\partial z} - \gamma_{CG}\right) + \frac{\partial}{\partial z}\left(K_M \frac{\partial E}{\partial z}\right) - c(\xi)E^{3/2} \tag{2.32}$$

where $K_T = K_M/P_r$ is the diffusion coefficient for heat and moisture, and P_r is the Prandtl number. Replace K_M and K_T in equation (2.32) with (2.28) and $\frac{\partial \boldsymbol{V}}{\partial z} \cdot \frac{\partial \boldsymbol{V}}{\partial z} = \left(\frac{\partial u}{\partial z}\right)^2 + \left(\frac{\partial v}{\partial z}\right)^2$ we get the TKE budget equation,

$$\frac{\partial E}{\partial t} = -a\lambda E^{1/2}\left[\left(\frac{\partial u}{\partial z}\right)^2 + \left(\frac{\partial v}{\partial z}\right)^2 + \frac{1}{P_r}\frac{g}{\theta_{vs}}\left(\frac{\partial \theta_v}{\partial z} - \gamma_{CG}\right)\right] - c(\xi)E^{3/2} + \frac{\partial}{\partial z}\left(K_M \frac{\partial E}{\partial z}\right) \quad (2.33)$$

Finally, the TKE equation can be formally

$$\frac{dE}{dt} = BE^{1/2} - CE^{3/2} + \frac{\partial}{\partial z}\left(K_M \frac{\partial E}{\partial z}\right). \quad (2.34)$$

where the terms in the right-hand-side represent the source-sink, the viscous dissipation and the redistribution with $B = -a\lambda\left[\left(\frac{\partial u}{\partial z}\right)^2 + \left(\frac{\partial v}{\partial z}\right)^2 + \frac{1}{P_r}\frac{g}{\theta_{vs}}\left(\frac{\partial \theta_v}{\partial z} - \gamma_{CG}\right)\right]$ and $C = c(\xi)$.

Introducing the definition of Richardson number,

$$R_i = \frac{g}{\theta_{vs}} \frac{\frac{\partial \theta_v}{\partial z}}{\left(\frac{\partial u}{\partial z}\right)^2 + \left(\frac{\partial v}{\partial z}\right)^2} \quad (2.35)$$

We get the expression for B,

$$B = -a\lambda \frac{g}{\theta_{vs}}\left[\left(\frac{1}{R_i} + \frac{1}{P_r}\right) - \frac{\gamma_{CG}}{P_r}\right]. \quad (2.36)$$

The source term (first term on the right side of 2.34) is produced by shear (positive) and buoyancy (positive or negative), that is, depending on the local Richardson number the coefficient B can be positive or negative as seen in (2.36). The coefficient C in the viscous dissipation term (second term on the right side of 2.34) is always positive.

The TKE is solved by a fractional step method which breaks down equation (2.34) into two parts:

$$\int_{n\Delta t}^{(n+1)\Delta t} dt = \int_{E^n}^{E^*} \frac{dE}{BE^{1/2} - CE^{3/2}}, \quad E \geq 0 \quad (2.37)$$

$$\frac{E^{n+1} - E*}{\Delta t} = \frac{\partial}{\partial z}\left(K_M{}^n \frac{\partial E^{n+1}}{\partial z}\right) \quad (2.38)$$

The first part (2.37) is done analytically (assuming B and C to be independent of time), the

details solution is given in GEM description Appendix 1. The second part (2.38), the diffusion part, the boundary conditions are vanishing flux at the base and at the top of the atmosphere, and the details on the solution is given is Appendix 2 in the GEM document. A time filter is applied with a coefficient of 0.5.

$$E_k^* = E_k + 0.5\nu\left(E_{k+1} - 2E_k + E_{k-1}\right) \tag{2.39}$$

with $\nu = 0.1$ and a lower bound of 10^{-4}m^{2}s^{-2} is imposed on E.

No additional free atmosphere vertical diffusion is included. GEM relies on the TKE equation to react to low values of Richardson number and generate sufficient upper air turbulence to do the required mixing.

2.11 CO_2 condensation

CO_2 condenses and releases the latent heat required to keep the solid–gas interface at the condensation temperature when the surface or air temperature falls below the condensation temperature. Conversely, when CO_2 ice is heated, it partially sublimes to keep its temperature at the frost point temperature. The amount of CO_2 condensed is computed from the top of the atmosphere to the surface within an air column and deposited at the ground within one timestep without falling velocity. There are no CO_2 ice clouds in the current model, and no radiative effect of CO_2 ice in the atmosphere. CO_2 ice can only stay on the surface. The condensation of CO_2 from the air and subsequently the sublimation of surface CO_2 ice impacts on the surface pressure. The surface pressure change is local and impacts the dynamics via this change in column mass. Note that in the model there is no CO_2 volume mixing ratio change and the impact of CO_2 phase change is reflected by the

global surface pressure change only. The scheme is based on Forget [1998] and code modified from WRF planet.

The mass of CO2 condensation in the atmosphere within the level N is calculated every time step,

$$\delta m_N = \frac{c_P M_N}{L}\left(T_{CN} - T_N\right) \tag{2.40}$$

$$T_{CN} = 149.2 + 6.48 * \ln(P/100) \tag{2.41}$$

where P is local pressure in P_a, T_N is the air temperature in layer N, T_{CN} is the condensation temperature at local pressure P, M_N is the layer mass kgm^{-2}, C_P is CO_2 specific heat at constant pressure (which is a constant in the model 735.9 J/kg/K), and L is the latent heat of sublimation or deposition of CO2 and is a constant 5.9×10^5 J/kg. At each time step, in the model, condensed CO2 from the whole column air is added to the total ice mass on the ground m_0. When the ground temperature is greater than T_{CN} at surface pressure and m_0>0, there are two cases considered:

(1) Partial sublimation of surface CO2 ice:

The surface temperature will keep as CO_2 the condensation temperature. The amount CO2 ice sublimated is given by

$$\delta m_S = \frac{c_i \rho_i}{L_i}\left(T_S - T_{CN}\right) \tag{2.42}$$

where ρ_i is the density of CO_2 ice $\rho_i = 1.5\times10^3$ kg/m^3, c_i is the specific heat of CO_2 ice with units in $Jkg^{-1}K^{-1}$ and it changes with temperature $c_i = 349. + 4.8 * T$.

(2) Complete sublimation of surface CO2 ice:

The surface temperature will decrease because some of the heating is used to sublimate CO_2

$$T_S = T_S - \frac{m_0 \mathrm{L}}{c_i(T_S)\rho_{\mathrm{i}}} \tag{2.43}$$

where m_0 is the total ice mass on the ground and $c_i(T_S)$ stands for the specific heat of CO_2 ice at surface temperature. Finally, we need to update the surface pressure at the current time step n via the previous time step n-1, that is $P_{S,n} = P_{S,n-1} - g(\delta m_s - \sum \delta m_N)$ at every time step.

2.12 The dynamics of GEM

The Global Environmental Multiscale model (GEM), Cote et al. [1997], is a consolidation of both the global and regional assimilation and forecasting systems within a single flexible modeling framework. This couples physics, chemistry, the needs of a nonhydrostatic mesoscale research model for the development and validation of physical parameterizations, such as surface and boundary layer phenomena, moist convection, gravity wave drag, as well as for nowcasting research.

The vertical coordinate of the GEM model is defined by $\eta = \frac{\pi - \pi_T}{\pi_S - \pi_T}$, where π the hydrostatic pressure of Laprise, that is, it satisfies $\rho g = -\frac{\partial \pi}{\partial z}$. The dynamics equations have been formulated in terms of the terrain-following hydrostatic pressure coordinate η. The governing equations of GEM dynamics are the forced hydrostatic primitive equations

as described by Cote [1997]:

Horizontal momentum: $\frac{dV^H}{dt} + R_d T_v \nabla ln p + \nabla \phi + f(\mathbf{k} \times \mathbf{V}^H) = \mathbf{F}^H$ (2.44)

Continuity equation: $\frac{d}{dt} ln \left|\frac{\partial p}{\partial \eta}\right| + \nabla \cdot \mathbf{V}^H + \frac{\partial \dot{\eta}}{\partial \eta} = 0$ (2.45)

Thermodynamic equation: $\frac{d}{dt}\left[ln\left(\frac{T_v}{T^*}\right) - \kappa ln\left(\frac{p}{p^*}\right)\right] - \kappa \dot{\eta} \frac{d}{d\eta}(lnp^*) = F^{T_v}$ (2.46)

Moisture equation: $\frac{dq_v}{dt} = F^{q_v}$ (2.47)

Diagnostic hydrostatic equation: $\frac{\partial \phi}{\partial \eta} = -R_d T_v \frac{\partial lnp}{\partial \eta}$ (2.48)

where $p = \rho R_d T_v$ and $\frac{d}{dt} = \frac{\partial}{\partial t} + \mathbf{V}^H \cdot \nabla + \dot{\eta} \frac{\partial}{\partial \eta}$ is the substantive derivative following the fluid, $\mathbf{V}^H$ is horizontal velocity, $\phi \equiv gz$ is the geopotential height, ρ is density, T_v is virtual temperature, $\kappa = R_d/c_{pd}$, R_d is the gas constant for dry air, c_{pd} is the specific heat of dry air at constant pressure, q_v is specific humidity of water vapor, f is the Coriolis parameter, **k** is a unit vector in the vertical, g is the vertical acceleration due to gravity, and $\mathbf{F}^H$, $\mathbf{F}^{T_v}$ and $\mathbf{F}^{q_v}$ are parameterized forcings.

The boundary conditions are periodicity in the horizontal and no motion across the top and bottom of the atmosphere, where the top is at constant pressure p_T [Cote, 1997]. Thus the boundary condition at the top and bottom of the atmosphere are $\dot{\eta} \equiv \frac{d\eta}{dt}$=0 at η=0,1.

The cloud liquid water, ice particles, chemical species such as ozone, hydrocarbons, and aerosols are transported in the GEM via atmospheric tracers. The advective form of transport equation is in the form,

$$\frac{\partial}{\partial t}(\rho \psi_i) + \nabla_3 \cdot (\rho \psi_i \mathbf{V}_3) = \rho F^{\psi_i} \quad (2.49)$$

where ψ_i is the mass mixing ratio of the *i*th atmospheric tracer, F^{ψ_i} is the parameterized forcing, $\mathbf{\nabla}_3$ and $\mathbf{V}_3$ are the three-dimensional gradient operator and velocity vector respectively [Cote, 1997].

The time discretization in GEM used to integrate the prognostic equations, such as equation 2.44-2.47 and 2.49, is implicit semi-Lagrangian. For a prognostic equation,

$$\frac{dF}{dt} + G = 0 \tag{2.50}$$

where F represents one of the prognostic quantities and G represents the remaining terms, some of which are nonlinear. Such prognostic equation is approximated by time differences and weighted average along a trajectory determined by an approximate solution to

$$\frac{dx_3}{dt} = \mathrm{V}_3(x_3, t) \tag{2.51}$$

where x_3 and V_3 are the three-dimensional position and velocity vectors, respectively [Cote, 1997]. Thus

$$\frac{F^n - F^{n-1}}{\Delta t} + \left[\left(\frac{1}{2} + \varepsilon\right) G^n + \left(\frac{1}{2} - \varepsilon\right) G^{n-1}\right] = 0 \tag{2.52}$$

where $\psi^n = \psi(x_3, t)$, $\psi^{n-1} = \psi[(x_3(t - \Delta t), t - \Delta t)]$, $\psi = (F, G), t = n\Delta t$, ε is the off-centering parameter currently set to 0.1 for the operational regional configuration. Grouping terms at the new time on the left-hand side and known quantities on the right-hand side, may be written as,

$$\left[F + \left(\frac{1}{2} + \varepsilon\right)\Delta t G\right]^n = \left[F - \left(\frac{1}{2} - \varepsilon\right)\Delta t G\right]^{n-1} \tag{2.53}$$

this yields a set of coupled nonlinear equations for unknown quantities at the mesh points of a regular grid the new time t. An implicit time treatment of nonlinear terms has useful property of being inherently computationally more stable than an explicit one [Cote, 1997].

The horizontal resolution is on an Arakawa C grid, which can be either variable-resolution or uniform-resolution in spherical geometry. In current GEM-Mars the uniform resolution is adopted. The uniform resolution reduces to the usual staggered finite-difference formulation in spherical geometry because it is more suitable for future massive parallel architectures than the implicit spatial discretization and it is considered to be the best one when the mesh length is less than the Rossby radius of deformation [Cote, 1997]. GEM uses an implicit (or semi-implicit) time treatment of the terms that govern the propagation of acoustic and gravitational oscillations in order to greatly retard their propagation and permit a much larger time step. A further advantage of a time-implicit treatment of acoustic and gravitational oscillations [Staniforth, 1997] is that for large time steps it dramatically retards the inward propagation of any error from the boundary region of a limited-area model, or from the outer region of a variable-resolution model. Furthermore, the use of a semi-Lagrangian treatment of advection, which is stable for Courant numbers much greater than unity, permits the time step to be chosen on the basis of accuracy rather than stability.

Chapter 3 Simulation with a one-dimensional model

A one-dimensional (1-D) model, i.e. a column of air with102 layers up to 190 km and 1 by 1 grid on the surface, no advection and no horizontal diffusion, is built for testing the physical scheme and debugging the code. The 1-D model includes all the physics schemes mentioned in Chapter 2. The model starts from an isothermal air temperature and surface temperature 220K, and a fixed logarithmic vertical wind profile. The following 1-D model results are compared with the results from a one-dimensional high-resolution boundary-layer UH (University of Helsinki) model, developed by Savijrävi et al. [2003].

3.1 Radiative schemes testing and comparison with UH 1-D model

The radiative adsorption and scattering due to CO_2 and dust in both solar and infrared bands control the low and middle atmosphere thermal structure. All the physical schemes mentioned in Chapter 2 are tested in our 1-D model. Furthermore, all the radiative results are compared with the UH model [Savijarvi et al., 2003] simulation and Mars Pathfinder (MPF) measurements [Savijaarvi et al, 2003]. The following runs start from an initial solar

longitude of 81^0 (Ls = 81^0) and go through 2880 time steps (120 sols) with a time step of one Mars hour; the plots are at around Ls = 141^0. Other input parameters are a surface pressure 675Pa, geostrophic wind 30 m/s, surface emissivity 0.95, surface albedo 0.21, scale height 10.8 km, gravity 3.72 m/s^2, and the air specific heat at constant pressure 764.8 J/kg/K. The total dust optical depth at the 120 sol of the run ~ Ls = 141^0 is around 0.25 (see Figure 3.13). The location is the Mars Pathfinder landing site at 19.13^0 N and 33.22^0 W.

Figure 3.1 shows MPF observations at the 3rd sol after landing (around Ls141^0) the observed near surface (1.27 m above surface) temperature (symbol plus) and UH model simulated temperature (solid line), and the surface temperature (dashed line) with dust optical depth ~ 0.3 from the UH simulation by Savijarvi et al. [2003]. Figure 3.2 is simulated surface and near surface temperature (~24 m above the surface) from our 1-D model at the same season. The MPF observation and UH simulation display a strong diurnal cycle with lowest temperature near 0600 local time ~197 K for 1.27 m and ~195 K for surface, and highest temperature ~260 K for 1.27 m around 1500 local time and ~275 K for surface around local 1300. From this diurnal temperature cycle we see a rapid increase for both air and surface temperature right after sun rise (after 0700), and a drop quickly after 1500 for both measurments and simulated near-surface temperature. Figure 3.2 is the simulated near surface temperature (~40 m above surface) and surface temperature. It shows the similar dinurnal temperature cycle, the maximum near suface temperature ~244 K and surface temperature ~282 K.

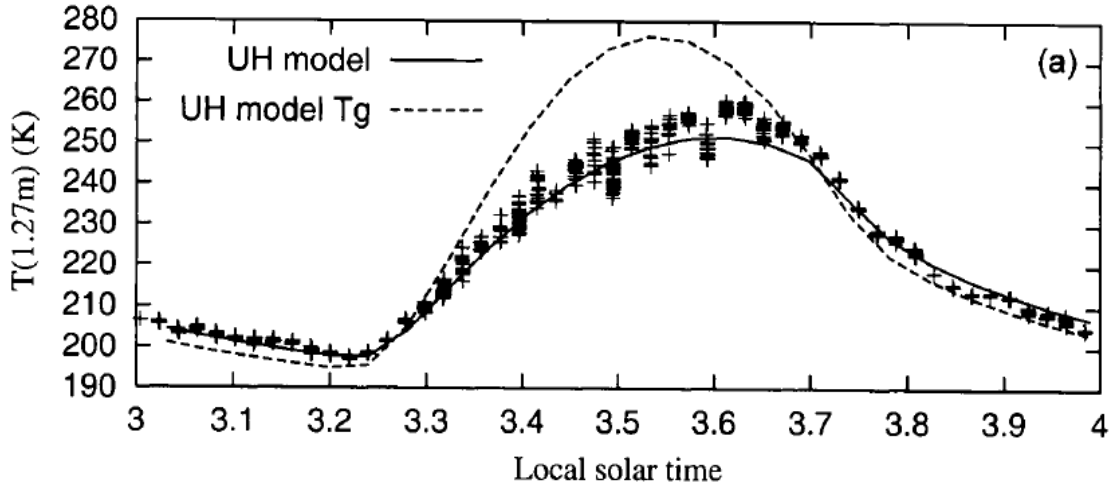

Figure 3.1: Diurnal near surface temperature cycle (1.27 m above surface) at the 3th sol from MPF observations (plus symbols) and simulation (full line), surface temperature (dashed line) around Ls = 141^0 from simulation with dust optical depth ~0.3 [Savijarvi et al., 2004].

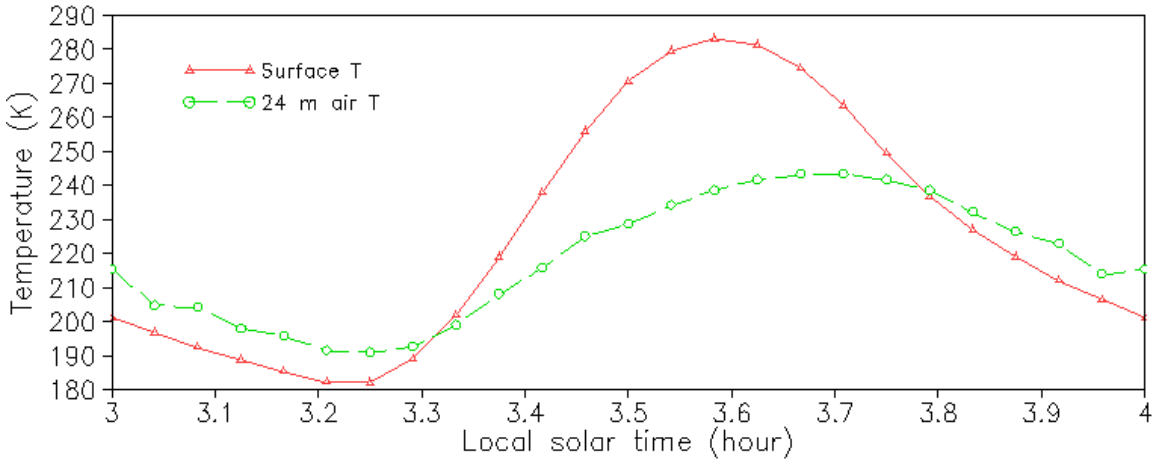

Figure 3.2: Simulated surface and near surface temperature (24 m above the surface) from 1-D model at the same time with simulated dust optical depth ~ 0.25.

The temperature is determined by radiative and turbulent processes in the 1-D model, and the advection and vertical motion are neglected. The main radiative components in the

Martian atmosphere are CO_2 and suspended dust aerosols. In our model the radiative heating schemes include the CO_2 thermal cooling, solar and infrared dust heating, CO_2 near IR heating, non-LTE (local thermodynamic equilibrium) cooling, UV-EUV heating, and the turbulent diffusion heating. From the surface up to 60 km CO_2 IR cooling, solar and infrared dust heating, and turbulent heating these three heating rates determine the atmospheric temperature. The suspended dust in the Martian atmosphere plays an important role in the radiation budget by absorbing and scattering solar radiation and emitting in the infrared. Our simulation suggests that dust can reach up to 60 km and mainly stay within the boundary layer, especially under 5 km.

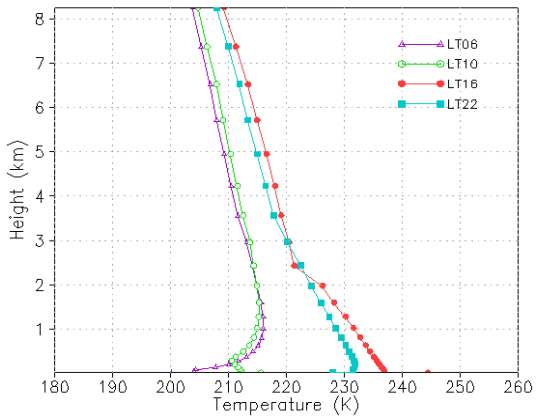

Figure 3.3: Vertical temperature profile from GEM-Mars 1-D model simulation at local solar time 0600,1000,1600, 2200

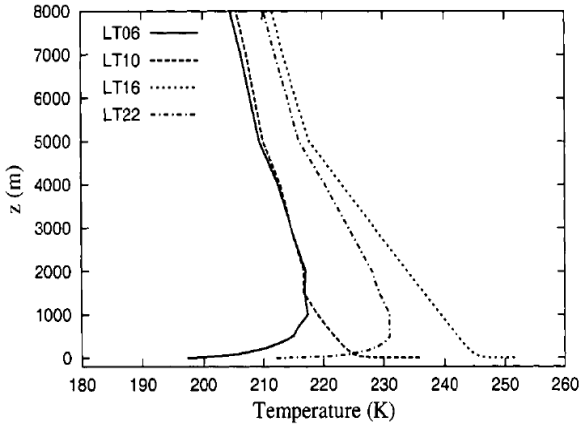

Figure 3.4: Vertical temperature profile from UH model simulation at local solar time 0600,1000,1600,2200

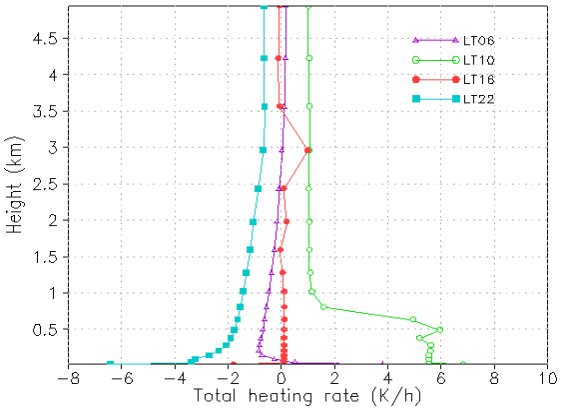

Figure 3.5: Same as Fig. 3.3 but for total (radiative+turbulent) heating rate (K/hr)

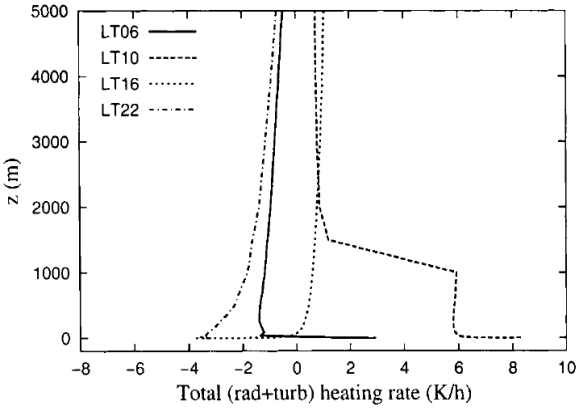

Figure 3.6: Same as Fig. 3.4 but for total (radiative+turbulent) heating rate (K/hr)

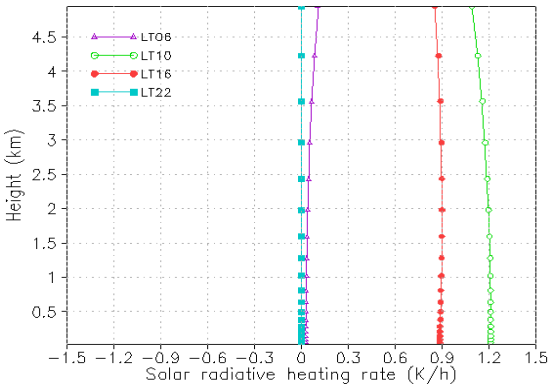

Figure 3.7: Same as Fig. 3.3 but for solar radiative heating rate (K/hr)

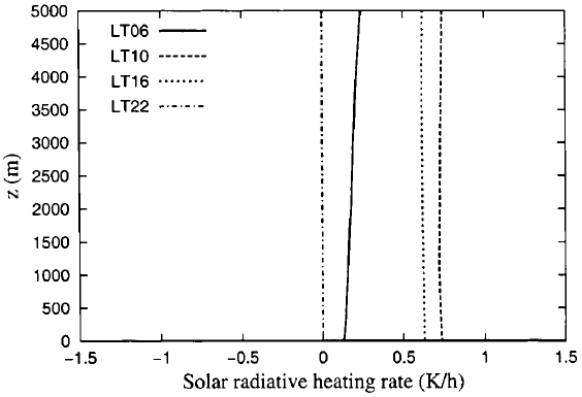

Figure 3.8: Same as Fig. 3.4 but for solar radiative heating rate (K/hr)

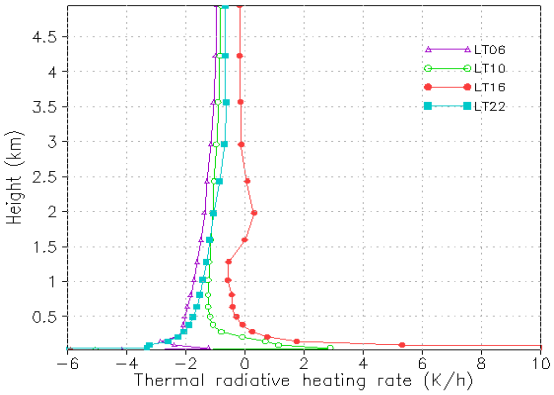

Figure 3.9: Same as Fig. 3.3 but for thermal long wave (CO_2+dust) radiative heating rate (K/hr)

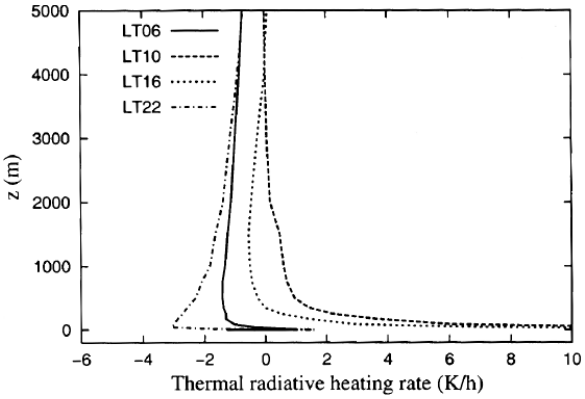

Figure 3.10: Same as Fig. 3.4 but for thermal long wave (CO_2+dust) radiative heating rate (K/hr)

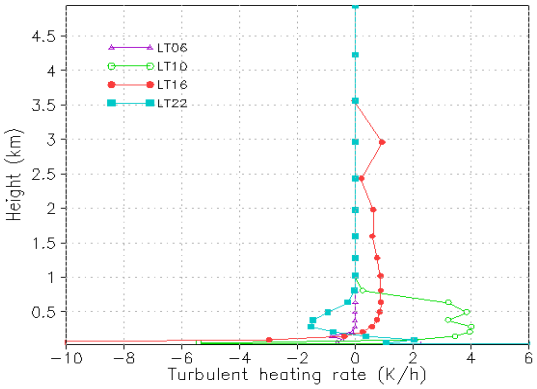

Figure 3.11: Same as Fig. 3.3 but for turbulent heating rate (K/hr)

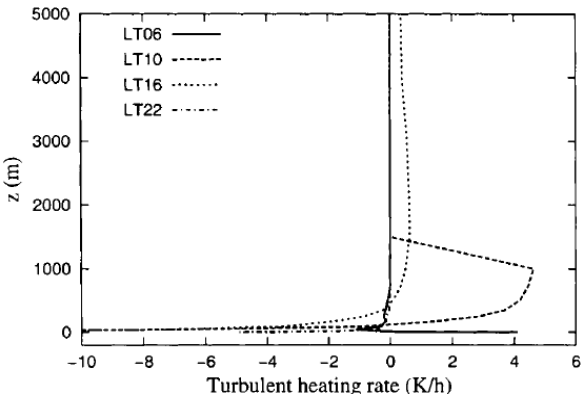

Figure 3.12: Same as Fig. 3.4 but for turbulent heating rate (K/hr)

Figure 3.3 is the vertical temperature profile from GEM-Mars 1-D model simulation at local solar time 0600,1000,1600, 2200 at MPF landing site around Ls = 141^0. Figure 3.4 displays vertical temperature profile from UH 1-D model simulation at local solar time. Their daytime temperature is warmer near surface and the night-time is cooler. The vertical temperature is determined by the total (radiative and turbulent diffusion) heating rate as shown in Figure 3.5 from GEM-Mars simulation and Figure 3.6 from UH model. The components of heating rate are displayed in Figure 3.7, 3.9, 3.11 as solar heating rate by dust absorption and scattering, thermal heating rate by CO_2 and dust, and turbulent diffusion heating rate in sequence from GEM-Mars 1-D model. The same heating rates are shown in Figure 3.8, 3.10, 3.12 from the UH 1-D model. In Figure 3.7 and 3.8 the solar heating rate is almost constant below 5 km with maximum ~1 K/hr and minimum around zero. The thermal heating rates in Figure 3.9 and 3.10 are negative at all the levels except for very near the surface at daytime approaching a maximum above 10 K/hr. Turbulent diffusion heating rates show opposite values near surface. The thermal heating rate and turbulent heating rate are strong and variable especially at near surface levels (under 2 km).

We know that CO_2 and water vapour are the most important greenhouse gases in Earth's atmosphere. The 15 μm long wave emission and absorption band of CO_2 in the Martian atmosphere is strong but quite narrow and as well as the low air pressure can explain why the greenhouse effect on present-day Mars is quite small despite the fact that 95% of the air consists of CO_2 [Savuärvi, et al., 2003]. During the daytime, the Mars surface reflects part of the solar radiation and absorbs the rest resulting in heating the surface temperature and emitting long wave radiation back to the atmosphere. The upwelling long wave radiation from surface is absorbed by cooler CO_2 and dust in the atmosphere resulting in warming of the atmosphere. The heating rate can be as high as 100 K/hr near the surface at midday. At night, the inverse occurs, and the warm atmosphere emits long wave radiation towards the cold surface which in turn warms the surface but cools the air near the surface. The cooling rate can reach -20 K/hr at night.

Figure 3.11 and 3.12 show the turbulent heating rate from GEM-Mars and UH 1-D model respectively. Our simulation shows the similar turbulent heating pattern to that of UH simulation except that the strongly positive turbulent heating rate reach up to 1 km in our model but 1.5 km in UH model. We can see during the daytime the surface is getting warmer, the boundary layer become unstable and the turbulent heating becomes stronger. However, near the surface because the daytime radiative heating is so intense, the turbulent flux divergence is actually cooling the atmosphere below 100 m, despite the fact that the surface layer is very unstable in the thin Martian atmosphere [Savuärvi, et al., 2003]. The activated convection is able to heat the air directly above the surface only shortly after sunrise (0600 Local time in Figure 3.11 and Figure 3.12) when the surface is just slightly

warmer than the air [Savuärvi, et al., 2003].

3.2 Dust lifting schemes

The two dust lifting schemes have been explored by using GEM-Mars 1-D model. Previous research suggested that the background dust in the Martian atmosphere is maintained by dust devils and the dust storms are caused by wind shear. In order to test wind shear lifting scheme the dust devils scheme was turned off. In our 1-D model, the near surface wind (~ 40 m above the surface) is the input to the dust lifting subroutine, a range of geostrophic wind from 10 m/s up to 50 m/s is tested. We found that the dust can be lifting from the surface and dust amount is gradually growing when the geostrophic wind is greater than 20 m/s. The following results are from 1-D GEM-Mars model with geostrophic wind 30 m/s. In the DEAD model a tuning parameter called global mass flux tuning factor is used to adjust the simulated column dust amount to match observed values. The default turning parameter of dust lifting mass flux is 7×10^{-4} for Earth but for Mars a factor of 2.6×10^{-4} is set in the following tests. This turning parameter was chosen by running GEM-Mars 3D model at different seasons and comparing the dust lifting locations and dust optical depths (details is discussed in section 4.3). In the 1-D GEM-Mars model the vertical dust mass flux lifted from the surface multiplies this factor and is divided into four dust bins which can be diffused upward by the vertical diffusion process and settled down by the dry deposition process.

Figure 3.13 shows the simulated dust optical depth from the 1-D GEM-Mars for 120 sols from Ls = 81^0 - 141^0 at MPF landing stie 19^0 N and 33^0 W. The red curve demonstrates

the total dust (wind shear lifting dust + dust devils lifting) optical depth, the green curve is the dust optical depth due to the wind shear lifting scheme and the black curve is the dust optical depth due to the dust devils lifting scheme. At the Sol 120 or around Ls = 141^0, the total dust optical depth is about 0.26, wind shear contributes about 0.2 which accounts for ~ 77% of total dust optical depth, and the rest about 0.05 optical depth is caused by dust devils. Figure 3.15 shows the sensible heat flux which controls the dust devils, and Figure 3.16 addresses the near surface wind which drive the wind shear lifting in 5 sols around Ls = 141^0.

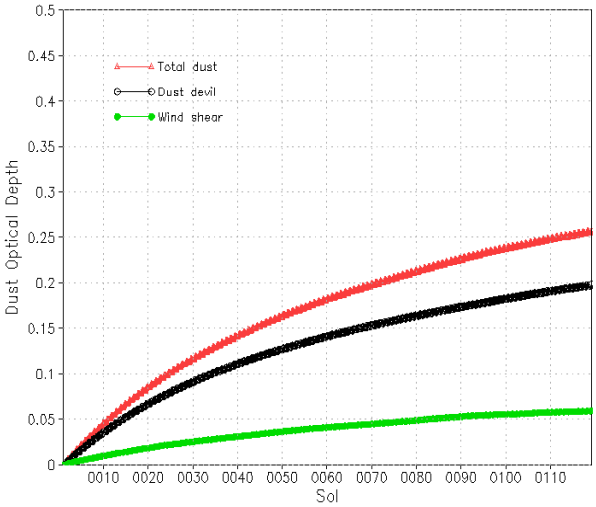

Figure 3.13: Dust optical depth from 1-D GEM-Mars for 120 sols at MPF landing site 19^0N and 33^0W (Ls = 81^0 - 141^0).

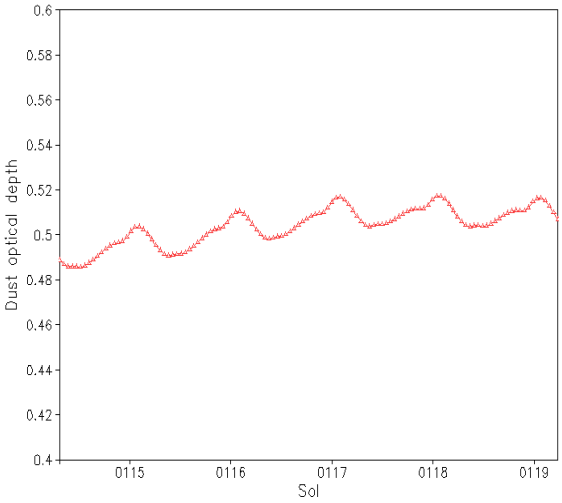

Figure 3.14: Dust optical depth from 3-D GEM-Mars for 5 sols (Ls = 141^0) at MPF landing site 19^0 N and 33^0 W.

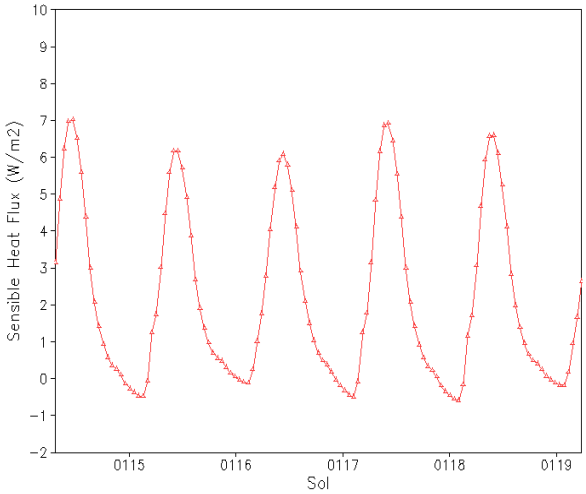

Figure 3.15: Sensible heat flux from 1-D GEM-Mars for 5 sols (Ls = 141^0) at MPF landing site 19^0N and 33^0W.

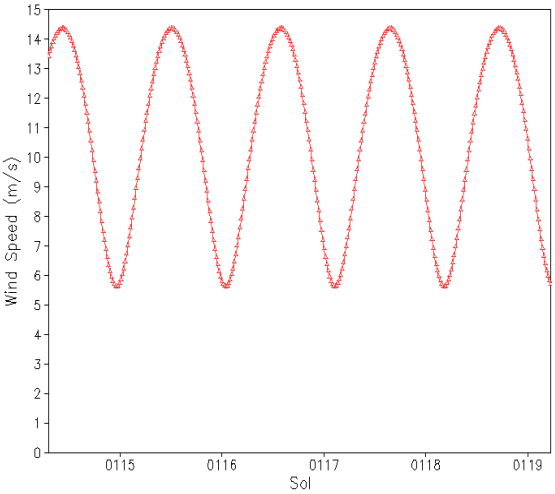

Figure 3.16: Near surface (~40 m above surface) wind speed from 1-D GEM-Mars for 5 sols (Ls = 141^0) at MPF landing site 19^0N and 33^0W.

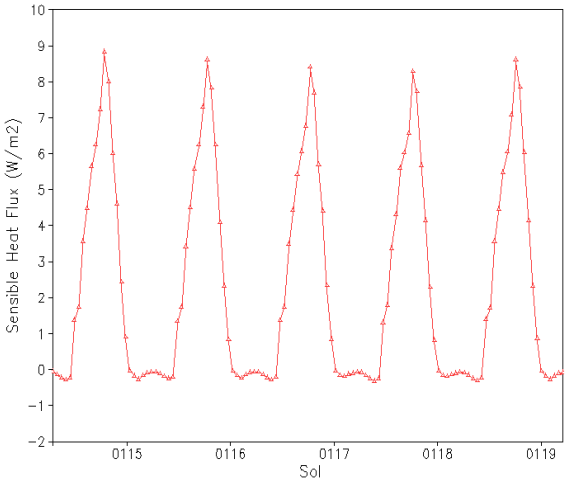

Figure 3.17: Same as Figure 3.15 but from 3-D GEM-Mars.

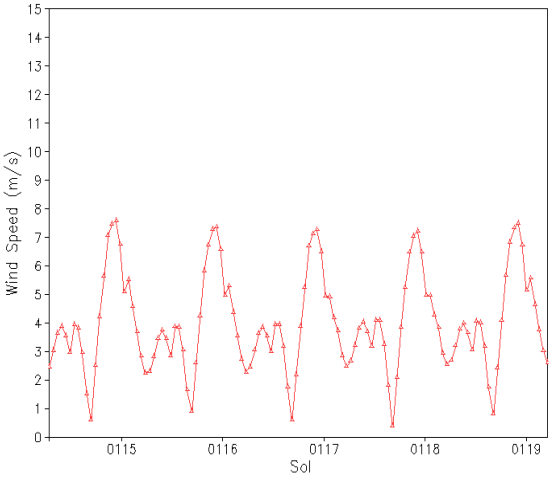

Figure 3.18: Same as Figure 3.16 but from 3-D GEM-Mars

Figure 3.14 shows the total dust optical depth including both wind shear and dest devils lifting from the 3-D GEM-Mars for 5 sols at the same time and location. The dust optical depth is in the range of (0.49, 0.51) shown in Figure 3.14 and increases when sensible heat

flux (shown in Figure 3.17) and wind speed (Figure 3.18) increase during the daytime. The sensible heat fluxes from 3-D model (Figure 3.17) and from 1-D model (Figure 3.15) are compareable and their magnitudes are in the range of (-1,9) Wm^{-2}. The simulated near surface wind from 3-D model (Figure 3.18) is almost 50% less than that from 1-D model (Figure 3.16). The fluctuation and less magnitude in wind speed in 3-D model (Figure 3.18) are due to the momentum diffusion through turbulence and the horizontal advention by GEM dynamics.

3.3 Surface heat budget

As described in section 2.9 the total heat flux in the atmosphere at the surface H_A is the sum of the upward infrared heat emitted by the ground, the sensible heat from the ground to the atmosphere, the latent heat of condensation, the downward solar flux, and the downward infrared flux from the atmosphere to the ground. The sign of H_A is defined as positive in the upward direction. The ground heat flux (or soil heat flux referred as Deardroff [1978]) G ($G = -H_A$) is the storage energy in the ground soil and is defined as positive when directed downward. The sensible heat flux on Mars is lower than that of Earth due to the Martian atmosphere density is much thinner than Mars. From our GEM-Mars result the typical sensible heat flux peaks at around 15 ~ 20 W/m^2 shortly after noon at low latitudes, and it is nearly zero at night. For Earth the sensible heat flux can reach several hundred W/m^2 varying with the locations and seasons. In GEM-Mars the latent heat released by CO_2 during the condensation and sublimation processes is neglected. We use a simplified force-restore method to derive the surface temperature. After we combine the upward and

downward infrared fluxes and ignore the latent heat, then the equation (2.22) becomes $H_A = LW + H_{sg} - SW = -G$. The LW stands for the net long-wave heat flux and SW for the net short-wave heat flux.

To evaluate the simplified force-restore surface scheme we compare our 1-D result with 1-D simulation developed by Davy [2009] which combines a planetary boundary layer (PBL) model based on that of Savijarvi et al. [2004] with an eddy-diffusion dust model [Taylor et al., 2007]. Our GEM-Mars had been run for 60 sol with an initial Ls = 60^0 and the geostrophic wind 32.5 m/s. The following result is plotted at around Ls = 90^0 after 60 sol running.

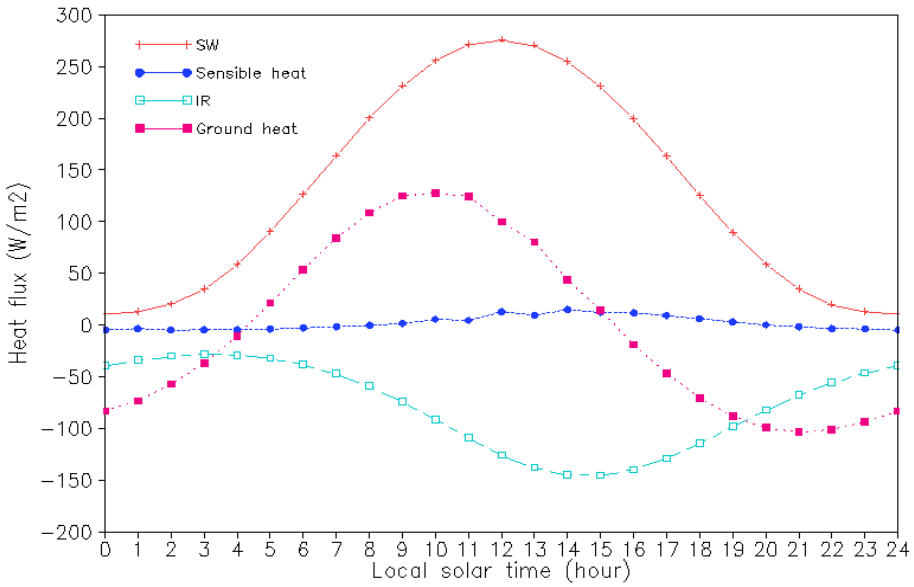

Figure 3.19: The diurnal surface heat budget simulated by GEM-Mars 1-D model for Phoenix landing site (68^0N, 234^0E) around Ls = 90^0 with geostrophic wind 32.5 m/s and dust optical depth ~ 0.3 at the sol 60 of the run: the net longwave heat flux (IR), the net shortwave (SW) heat flux, sensible heat flux, and ground heat flux for 1 sol (24 hours).

Figure 3.19 shows the diurnal surface heat budget simulated by our GEM-Mars 1-D

model for Phoenix landing site (68^0N, 234^0E) around Ls = 90^0. The surface scheme in the GEM-Mars 1-D model is simplified force-restore method. Figure 3.20 displays the diurnal surface heat budget produced by PBL 1-D model [Davy, 2009] which adopts a five-layer Crank-Nicholson surface scheme [Savijarvi 1995]. The maximum value of the net solar heat flux of our model is about 40 W/m^2 more than that of Davy's model resulting in our ground heat flux is ~40 W/m^2 more in the magnitude. Both simulated sensible heat fluxes are around zero during the night and morning, and are getting higher (below 10 W/m^2) during the afternoon. The two simulated longwave (infrared) heat flux are consistent with lowest values around -175 W/m^2 and highest around -50 W/m^2.

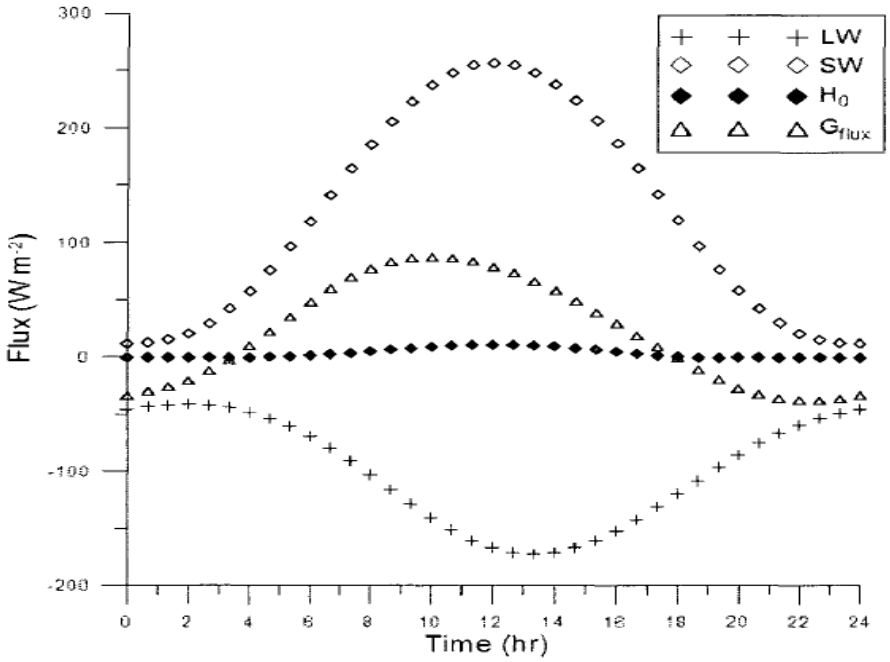

Figure 3.20: The diurnal surface heat budget simulated by Davy's 1-D model for the same location and time with dust optical depth ~ 0.3 [Davy, 2009].

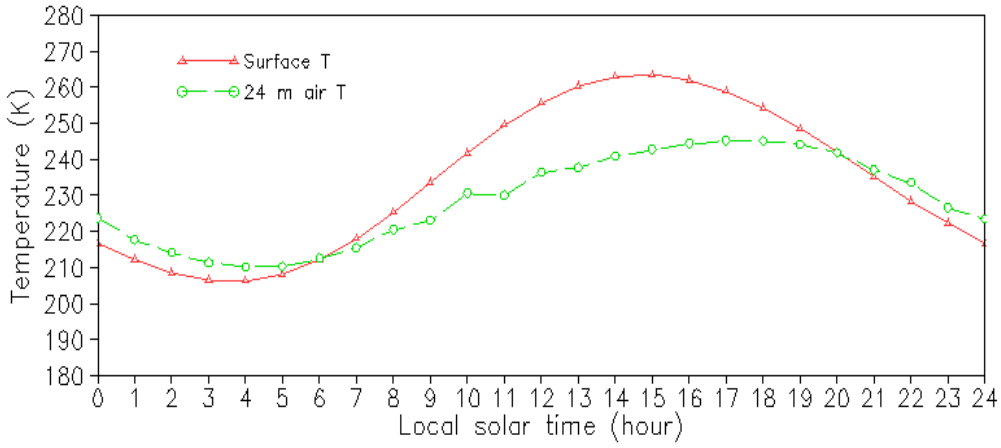

Figure 3.21: The diurnal temperature profile simulated by GEM-Mars 1-D model for Phoenix landing site (68^0N, 234^0E) around Ls = 90^0 with geostrophic wind 32.5 m/s, and the dust optical depth ~ 0.3 at the sol 60 of the run. The surface and near air temperature (24 m above the surface) are plotted for 24 hours.

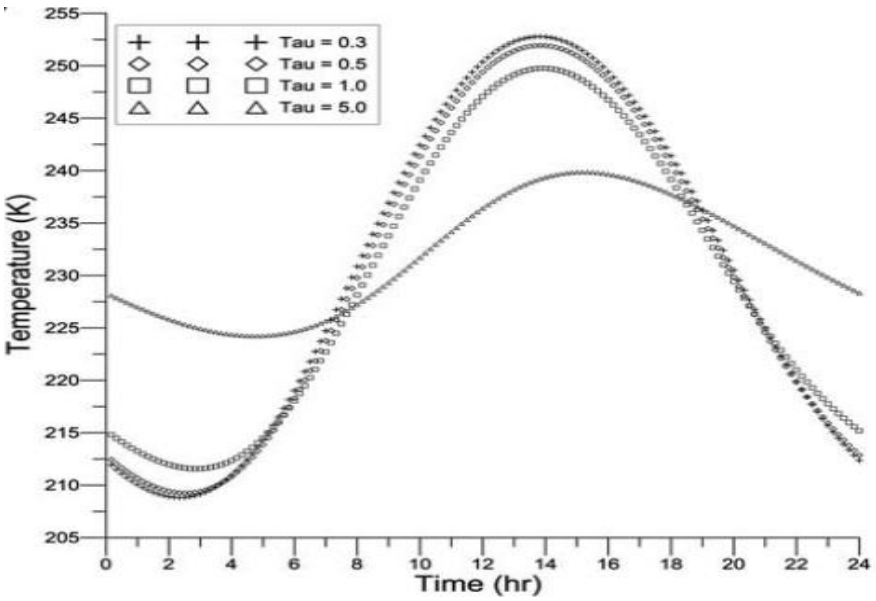

Figure 3.22: The diurnal surface temperature for the Phoenix landing site a ~ Ls = 90^0 with dust optical depth of 0.3, 0.5 1, and 5 [Davy, 2009].

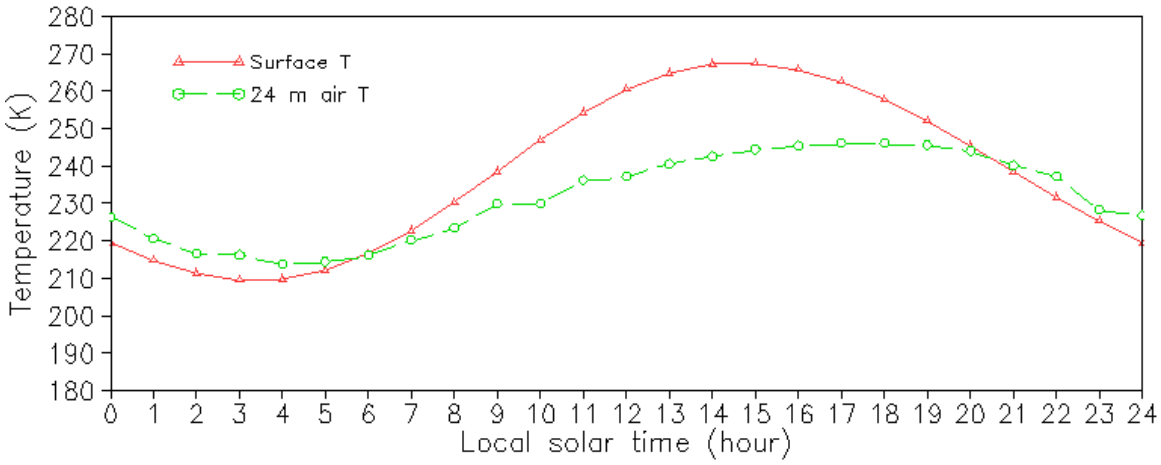

Figure 3.23: The simulated diurnal surface and near air temperature by GEM-Mars 1-D model for Phoenix landing site at Ls = 90^0 with geostrophic wind 30 m/s and the dust optical depth ~ 0.175 at the sol 60 of the run.

The simulated surface temperatures are plotted in Figure 3.21 (GEM-Mars 1-D model) and 3.22 (Davy's 1-D model). The surface temperature in Figure 3.21 is in the range of 205 K ~ 263 K and in Figure 3.22 is in the range of 207 K ~ 257 K for dust optical depth 0.3. Our surface temperature is ~6 K higher than that of Davy's due to the greater ground heat flux in our 1-D model. Both 1-D models contain dust lifting schemes with the dust optical depth varying around 0.3 for both surface heat budget profiles. The latent heat due to CO_2 phase change is ignored in both models.

To explore how much dust optical depth affects surface temperature, different geostrophic wind 30 m/s and 35 m/s are tested for the Phoenix landing site. Again, the test was set an initial Ls = 60^0 and run for 60 sols. Figure 3.23 and Figure 3.24 are plotted for geostrophic wind 30 m/s and 35 m/s, which result in dust optical depth ~ 0.175 and 0.5 respectively at the sol 60 of the run ~Ls = 90^0. After 60 sols run, the dust optical depth

reaches 0.175 corresponds to the surface temperature with a diurnal cycle 210 ~ 268 K; the dust optical depth reaches 0.6 corresponds to the surface temperature with a diurnal cycle 202 ~ 258 K. The near air temperature (24 m above the surface) is in the range of 213~245 K and 206~240 K respectively. Thus stronger wind cause greater dust optical depth and lower surface temperature (~8 K less) in both daytime and night time; near air temperature ~5 K less in the daytime and ~7 K less at night.

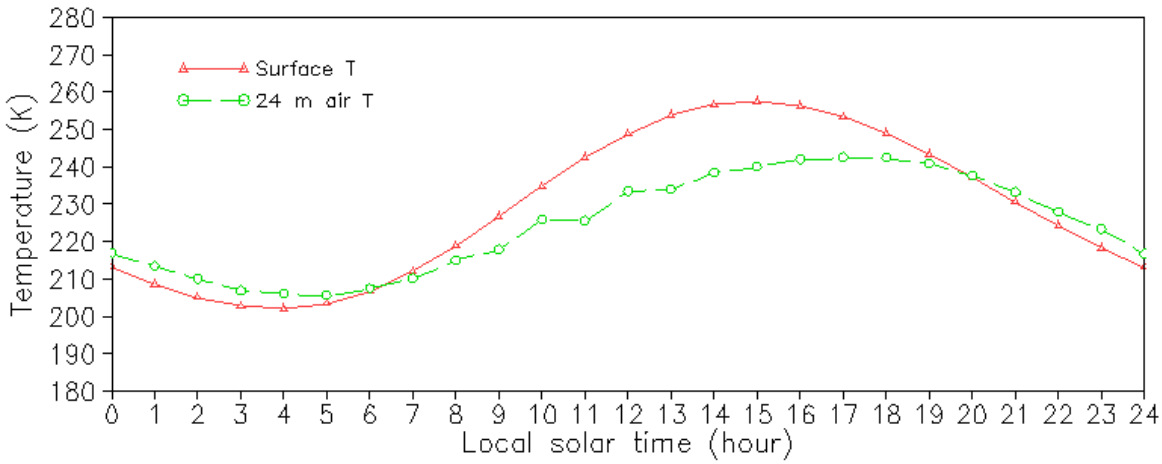

Figure 3.24: Same as Figure 3.23 but with geostrophic wind 35 m/s and the dust optical depth ~ 0.5 at the sol 60 of the run.

Chapter 4 Simulation with 3-D GEM-Mars

In the current 3-D GEM-Mars model, the horizontal resolution is 64 by 36 grid nodes, (5.625^0 by 5^0), with 102 vertical levels from surface up to ~180 km. Initial input data is measured thermal inertia and albedo from TES and topography from MOLA. The model runs from an initial isothermal temperature atmosphere 220K, with no wind and no dust in the atmosphere. The model is run from Ls = 0^0 with a time step of 3698.97 seconds, (~1 Mars sidereal hour with 24 hours per sol, one sol is about 88775.244 seconds) and had been run for three years. Different time steps 5, 15, 30, 60 minutes have been tested in GEM-Mars. There is no significant effect in accuracy between these results after the model run for 60 sols. GEM-Mars can run in a high horizontal resolution of 2^0 by 2^0 but in order to get high efficiency and compare with other GCM models, which usually use about 5^0 by 5^0, the horizontal resolution 5.625^0 by 5^0 is adopted in the current GEM-Mars.

The time required for a model to research a pseudo equilibrium is called spin-up time. Previous study of Mars GCM dynamics by Moudden [2005] has shown a spin-up time of 30 sols which is similar to the other simulations such as Haberle et al. [1993b]. In the testing runs, spin-up times between 30 and 60 sols were used to tests physics schemes at

different seasons. We find that the dynamics fields obtain a stable diurnal cycle within a spin-up time of 30sols. In the following results the Mars-Mars has run for three Mars year and all the plots are taken from the second and third Mars year. We use the first Mars year to complete one year CO_2 cycle since there is no CO_2 ice deposited on both poles in the initial state.

4.1 The dust cycles in multiyear simulation and observation

The global dust storm on Mars appears every two or three years according to the previous observations. GEM-Mars was set to run three Mars years starting from Ls (solar longitude) = 0^0 to Ls = 1080^0 with one Mars year equal to 360^0 in Ls. The GEM-Mars results show that the surface column dust optical depth almost repeated in the three Mars years as seen in Figure 4.1. The retrieved 3.5 Mars years of dust optical depth from the Thermal Emission Imaging System (THEMIS) on board the Mars Odyssey spacecraft in Figure 4.2 provide apparent inter-annual variability, with one global dust storm that occurred in the third observed year (MY 26). THEMIS has retrieved the column dust and water ice in nine thermal bands for three and half Mars years. The observed column dust optical depth in Figure 4.2 is retrieved at wavelength 1075 cm^{-1} (equivalent 9.36 μm). In the current GEM-Mars model we adopt a visible optical dust opacity to IR ratio as a factor of 2 ($\tau_{0.67\mu m}/\tau_{9\mu m}$=2 [Forget, 1998]). The simulated dust optical depth in the DEAD model is calculated in the wavelength 0.63 μm [Zender, 2003] so a factor of 0.5 is multiplied to simulated dust optical depth to get the IR dust optical depth which is consistent with the wavelength (9.36 μm) measured by THEMIS.

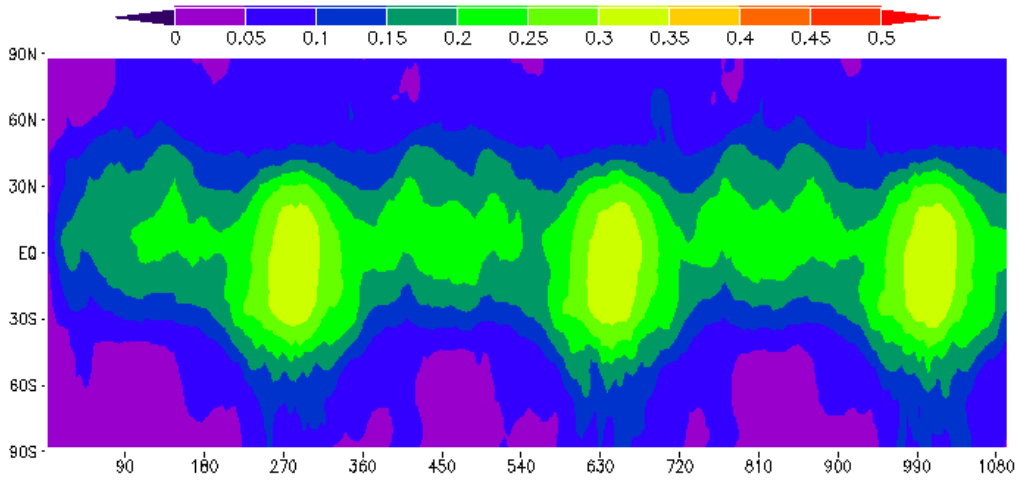

Figure 4.1: Daytime zonal average column dust optical depth over three Mars years from GEM-Mars simulation. The simulated visible optical dust opacity is scaled to IR band by a factor of 2 ($\tau_{0.67\mu m}/\ \tau_{9\mu m}=2$ [Forget, 1998]) and scaled to an equivalent 6.1 mbar pressure surface to remove the effect of topography.

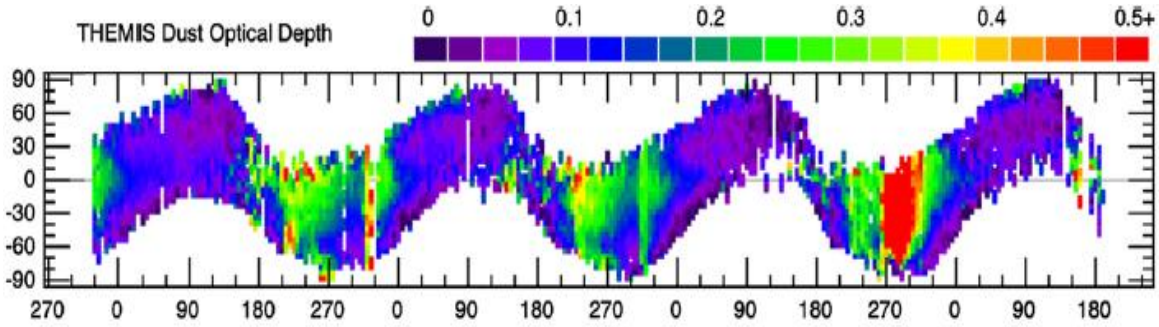

Figure 4.2: Daytime zonal average column dust optical depth over 3.5 Mars years from THEMIS [Smith 2009]. The dust optical at 1075 cm^{-1} (9.35 μm) scaled to an equivalent 6.1 mbar pressure surface to remove the effect of topography.

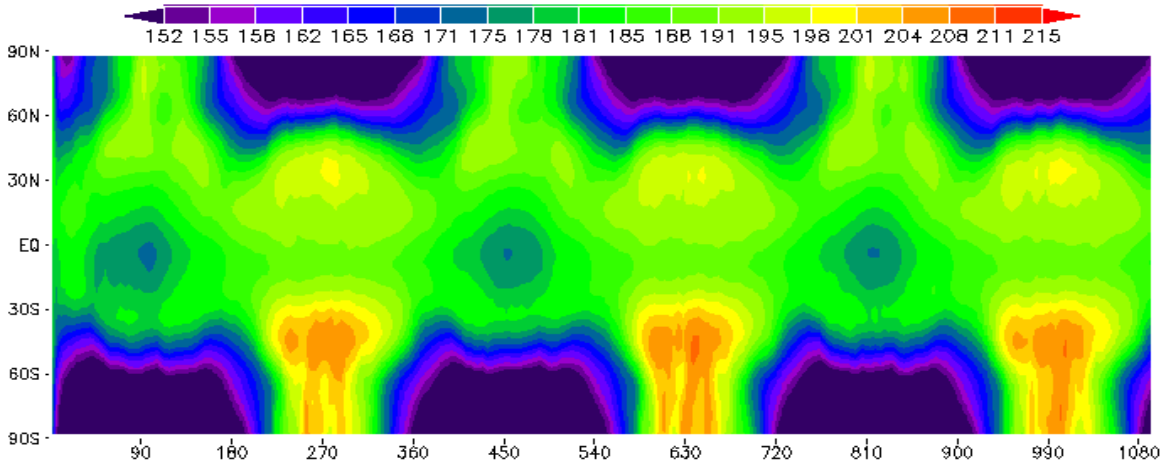

Figure 4.3: Daytime zonal average air temperature at ~0.5 mb (~25 km above the surface) over three Mars years from GEM-Mars simulation.

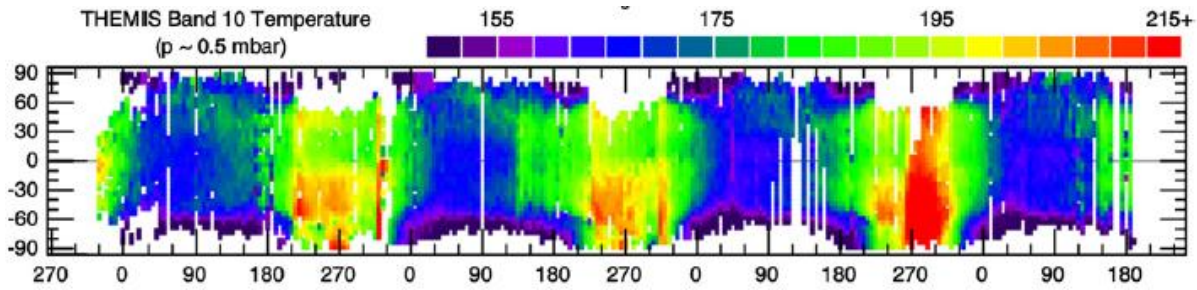

Figure 4.4: Daytime zonal average air temperature at ~0.5 mb (~25 km above the surface) over 3.5 Mars years from THEMIS [Smith 2009].

Comparing Figure 4.1 and 4.3 (simulations) with Figure 4.2 and 4.4 (observations), we see that the observations demonstrate that the perihelion season (roughly southern spring and summer) Ls = 180^0 - 360^0, is relatively warm and dusty, while the aphelion season (Ls = 0^0 - 180^0) is relatively cool and free of dust. The perihelion season shows a relatively high degree of inter-annual variability in dust optical depth and atmospheric temperature while the aphelion season shows a low degree of inter-annual variability for dust optical depth and air temperature.

Furthermore, the simulated column dust optical depth is scaled to a surface pressure of 6.1 mbar to remove the effect of topography, i.e., dust optical depth is scaled by the factor of 6.1/surface pressure/1.3. The factor of 1/1.3 is because the retrieved values from the THEMIS IR band spectral measurements considered only the dust absorption radiative effect without scattering. The extinction optical depth is about 1.3 and 1.5 times as large as the absorption optical depth for dust and water ice respectively for low and moderate optical depth (<0.5) [Smith, 2004], while the simulated dust optical depth is the extinction optical depth which is the sum of absorption and scattering optical depth. The THEMIS observed at about 5pm local sidereal time on Mars for Mars Years 26, 27, 28 and half of MY29, where each MY runs from Ls = 0^0 to Ls = 360^0 i.e. one circle of solar longitude. Thus the simulated data chosen for daytime is between 3pm and 6pm local sidereal time on Mars.

Observations illustrate that there is one global dust storm appeared in the observed three and a half Mars years, which is showed in the third year in Figure 4.3. In the three simulated Mars year, there is no global dust storms appeared as the dust optical depth is between 0.3 and 0.35 during perihelion season. Between 30^0 N and 30^0 S the simulations predict higher optical depths than measurements in the aphelion seasons is mainly due to the simulated thermal convection dust lifting usually occur around equator and low latitudes where the sensible heat flux is much greater than higher latitudes areas. During the aphelion season simulated dust optical depths are below 0.25 while the measurements are below 0.15. Corresponding simulated air temperatures at ~ 0.5 mbar within northern hemisphere are ~ 10 K or ~ 20 K higher than the measurements during the aphelion season. Note that in

Figure 4.3 the Model output temperatures are chosen around 0.5 mb as the model's vertical levels are hybrid levels and on each level there are large variations in pressures because of striking differences in elevations on Mars.

The THEMIS observations are consistent with previous TES observations. Figure 4.6 shows the globally averaged dust optical depth (only absorption optical depth considered) observed by TES during MY 24, 25 and 26 for a total of three Mars years. The retrieved absorption dust optical depth from TES shows a background dust optical depth of about 0.15 during Ls = 180^0 to Ls = 360^0. The magnitude and time of dust storms varied within the three years. Similar magnitude dust storms appeared in MY 23 (not plotted in Figure 4.6) and MY 24 at Ls = 225^0 and Ls = 330^0. In MY 25 there was a planet-encircling dust storm and the globally-averaged dust optical depth reached 1.3 at Ls = 205^0-215^0 [Smith 2003]. During Ls = 0^0-180^0 dust optical depth is below 0.15, while after Ls = 0^0 the dust optical depth gradually decreases to a minimum level 0.05 at Ls = 135^0. After Ls = 135^0, global dust optical depth rises to the 0.15 level by Ls = 180^0 [Smith 2003]. In the perihelion season (Ls = 180^0 - Ls = 360^0) global dust optical depth changes from year to year but in the aphelion season (Ls = 0^0 - Ls = 180^0) the global dust optical depth shows higher consistency between years with variations seldom exceeding 0.02 from year to the next [Smith 2003].

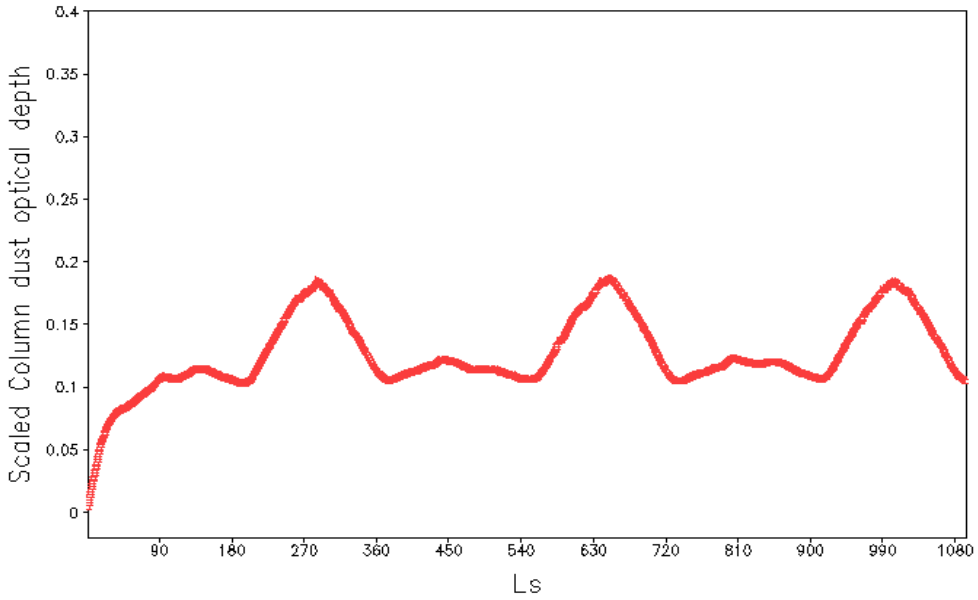

Figure 4.5: Global average column dust optical depth scaled to IR band from GEM-Mars for three Mars years

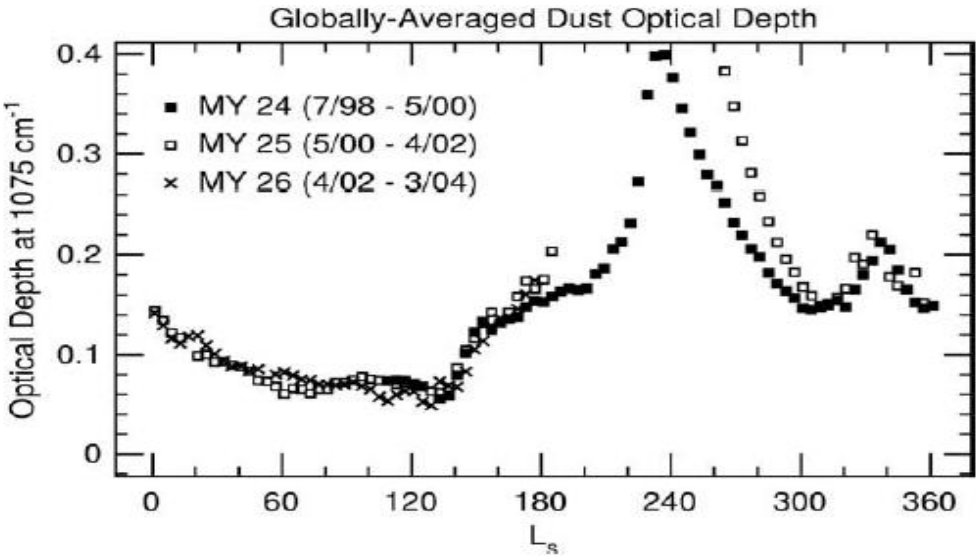

Figure 4.6: Observed global average dust optical depth at IR band from TES for Mars years 24, 25 and 26 [Smith 2003]

The simulated dust optical depth in Figures 4.5 is scaled to an equivalent 6.1 mbar pressure surface (by multiplying dust optical depth by a factor 6.1 mbar/surface pressure) and scaled to absorption dust optical depth by multiplying by 1/1.3. The simulated global dust optical depth shows a repeated pattern in the three Mars years. It appears that the current version of GEM-Mars cannot simulate the interannual variability in dust storms. Although the reasons for the interannual variability are still unclear, the two assumptions made in GEM-Mars may cause the model not be able to capture it. The first assumption is the global uniform surface roughness length (0.01m), and the second is the unlimited dust reservoirs on the surface without any deflation after dust lifting.

The simulated global dust optical depth in Figure 4.5 agrees with the observation that dust storms occur in the aphelion seasons and that there is a much lower dust optical depth in perihelion seasons. But the detailed variation of global dust optical depth in our model is different from the observations in the following aspects:

1) After Ls = 0^0 the simulated dust optical depth increases gradually until Ls = 90^0 then decreases gradually until Ls = 185^0, so there are two minimums at Ls = 185^0 and Ls = 360^0 around 0.15. While the observed dust optical depth decreases until Ls = 135° and one minimum around 0.05.

2) After Ls = 180^0 the simulated dust optical depth increases relatively sharply, reaches a maximum (0.3) near Ls = 270^0 and then decreases sharply until Ls = 340^0. The observed dust optical depth varies in amplitude and in timing.

4.2 The CO_2 cycles in multiyear simulation and observation

Every Mars year about ~30% of the CO_2 in the atmosphere is involved in a CO_2 deposit and sublimation cycle which causes variation of the mean surface pressure. The average density of seasonally deposited CO_2 ice is in the range of 910 ± 230 kg/m^3 [Smith, 2001]. Figure 4.7 shows that the simulated deposited CO2 ice approaches a maximum of 550 kg/m^2 at latitudes higher than 80^0 in the northern hemisphere. The corresponding maximum CO_2 ice depth is about 0.6 m (taking the average CO_2 ice density as 910 kg/m^3). This is lower than the measured greatest elevation change (1.5 to 2 m) [Smith, 2001]. The deposited CO_2 ice appears repeatedly in all simulated Mars years. Model simulated surface pressure shown in Figure 4.8 again repeats every Mars year. The surface pressure becomes lowest when more CO_2 ice is deposited in the northern winter.

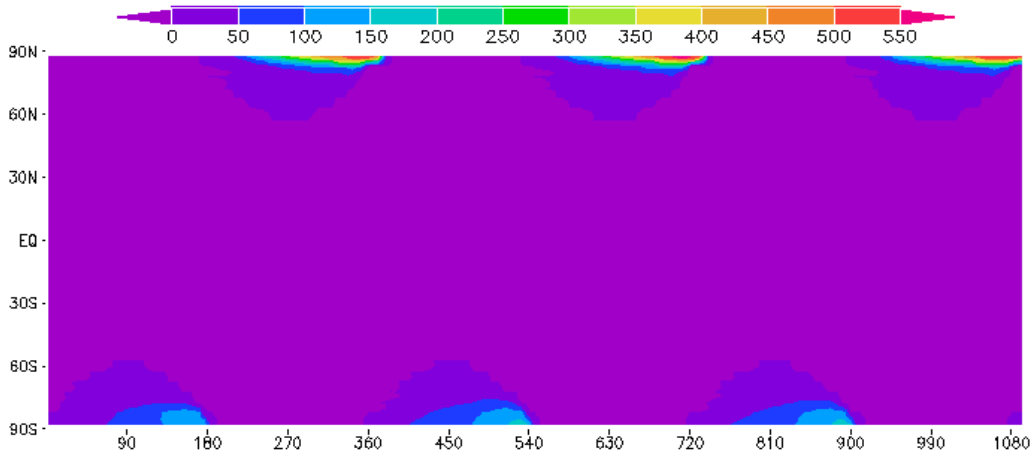

Figure 4.7: Simulated zonal average accumulated CO_2 ice (kg/m^2) within three Mars years

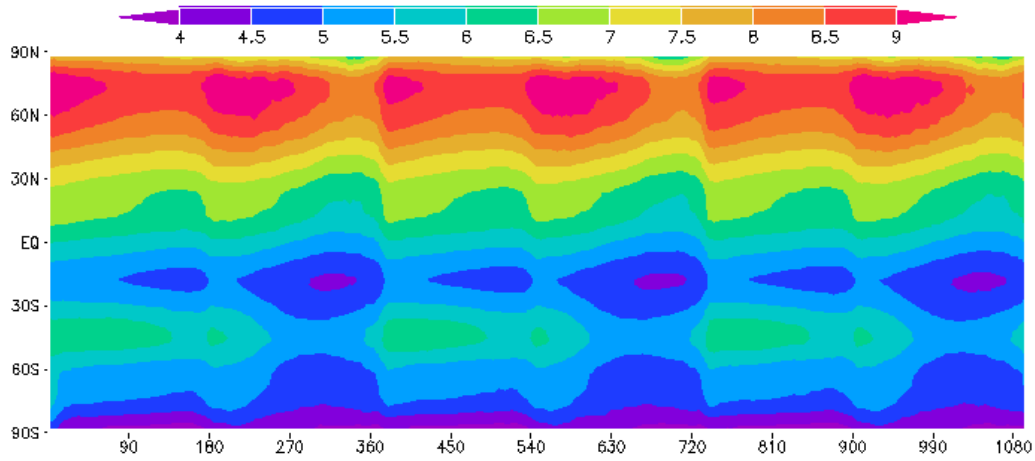

Figure 4.8: Simulated zonal average surface pressure (mbar) within three Mars years

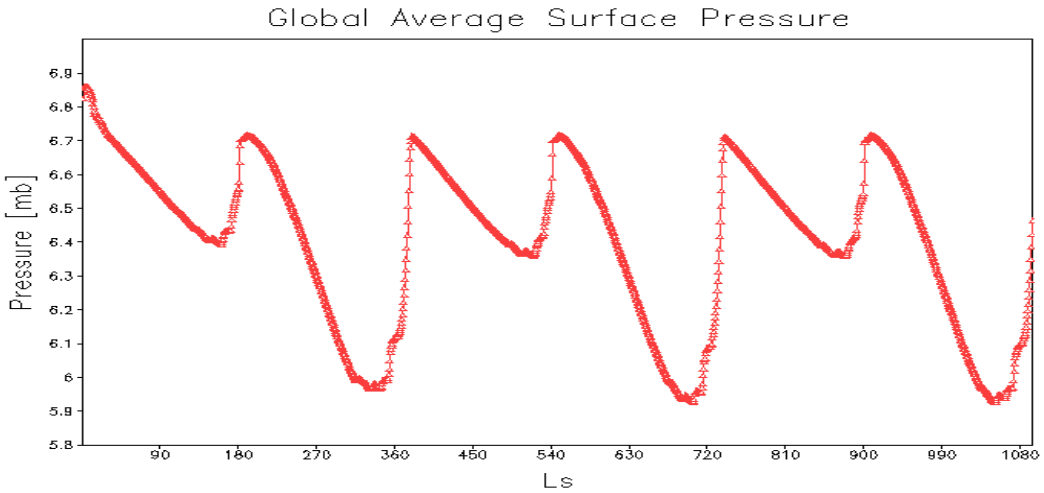

Figure 4.9: Global average surface pressure from GEM-Mars for three Mars years

A clearer view of the change of global average surface pressure is shown in Figure 4.9 it shows a variation of about 0.8 mbar between the maximum (6.7 mbar) and the minimum global average surface pressures (5.9 mbar). Other simulations and measurements by High Energy Neutron Detector (HEND) on board Mars Odyssey show this variation in global average surface pressure around 1.0 to 1.5 mbar [Karatekin, 2006]. This result again shows that the simulated deposition of CO_2 ice is less than that measured. The zonal and time averaged surface deposited CO_2 ice in Figure 4.7 agrees with the measurements that CO_2

ice in southern winter covers larger areas than in the northern winter due the longer southern fall and winter. The deeper CO_2 deposition in north polar cap is consistent with the measurement described by Smith et al. [2001] that the snow deposition on the northern ice cap is greater than in the south ice cap at latitudes above 80^0. The zonal and time averaged surface pressure in Figure 4.8 confirms that there is striking difference in surface pressure between northern and southern hemisphere due to the difference in elevation of Mars topography.

4.3 The variations of dust in different seasons

The dust cycle on Mars varies with the seasons on Mars. Figure 4.10 and Figure 4.11 at four seasons Ls = 90^0, 180^0, 270^0 and 360^0 are simulated dust column optical depth and surface temperature for the second simulated year. Note that the results of the third simulated year are almost the same to those in the second year. We can see that there are large dust storms which start to form around Ls = 180^0 and are well developed at Ls = 270^0 and the dust lifting centers are generated in the agreement with observations, the western and northern rim of Hellas (42.4°S, 70.5°E), Syria in the southern part of Tharsis (1.57°N, 112.58°W), in the northern midlatitudes in the Acidalia (49.8°N 20.7°W) and Chryse (28.4°N 40.3°W) regions The lifted dust spreads globally and the dust optical depth is greater than 1 around Hellas at Ls = 270^0.

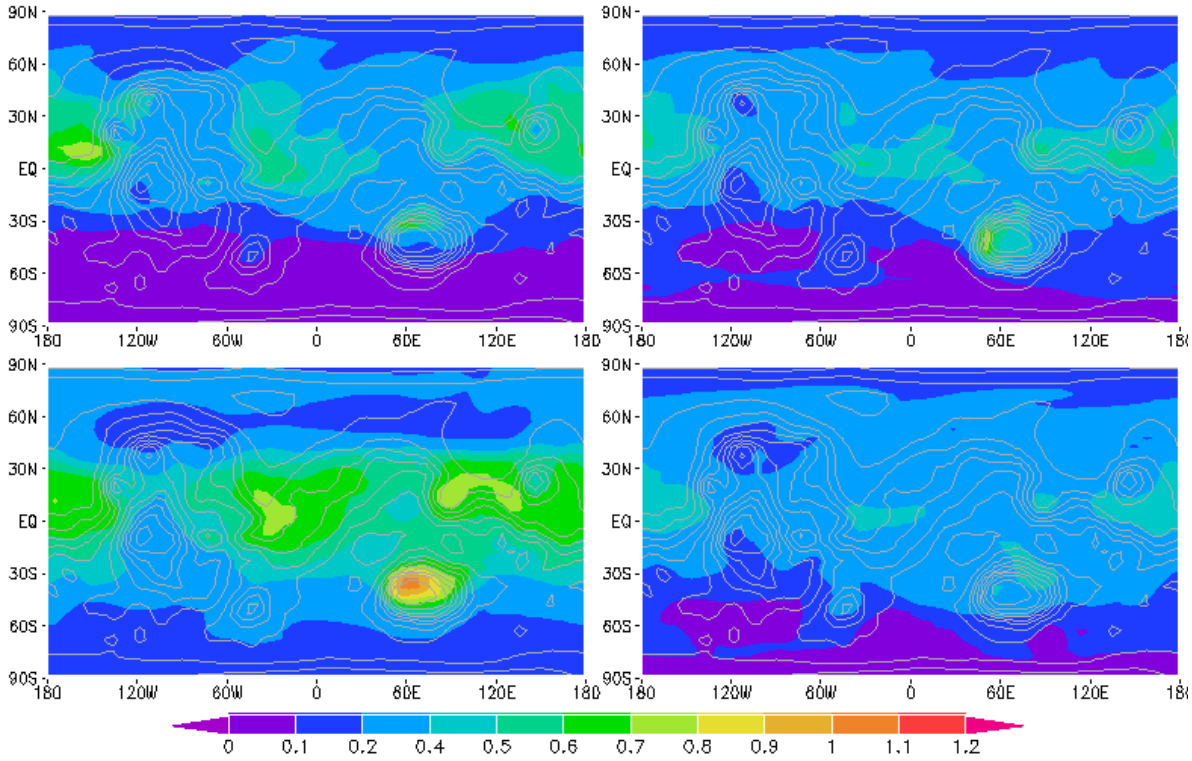

Figure 4.10: The snapshots surface dust column optical depth in the visible wavelength 0.63 μm at four seasons Ls = 90^0 (top left), 180^0 (top right), 270^0 (bottom left), 360^0 (bottom right) for the second simulated year. The local noon is around longitude 30^0 E. The background gray contours stands for the topography.

In Figure 4.11 the variation of surface temperature with seasons is driven by the solar insolation. At northern summer solstice at Ls = 90^0 the maximum surface temperature is round 30^0 N and is below 280 K, and it is relatively lower than other season since the largest Sun-Mars distance (Aphelion) occurs at Ls = 71^0. At the spring equinox (Ls = 0^0) and autumn equinox (Ls = 180^0) the maximum surface appear around equator. The maximum surface temperature is below 290 K at autumn equinox and is higher (below 300 K) at spring equinox, because the global dust storms during southern summer haven't

decayed totally at spring equinox in our simulation. The maximum surface temperature can be higher than 300 k at winter solstice (Ls = 270^0) since there are dust storms and smallest sun-Mars distance is at Ls = 251^0.

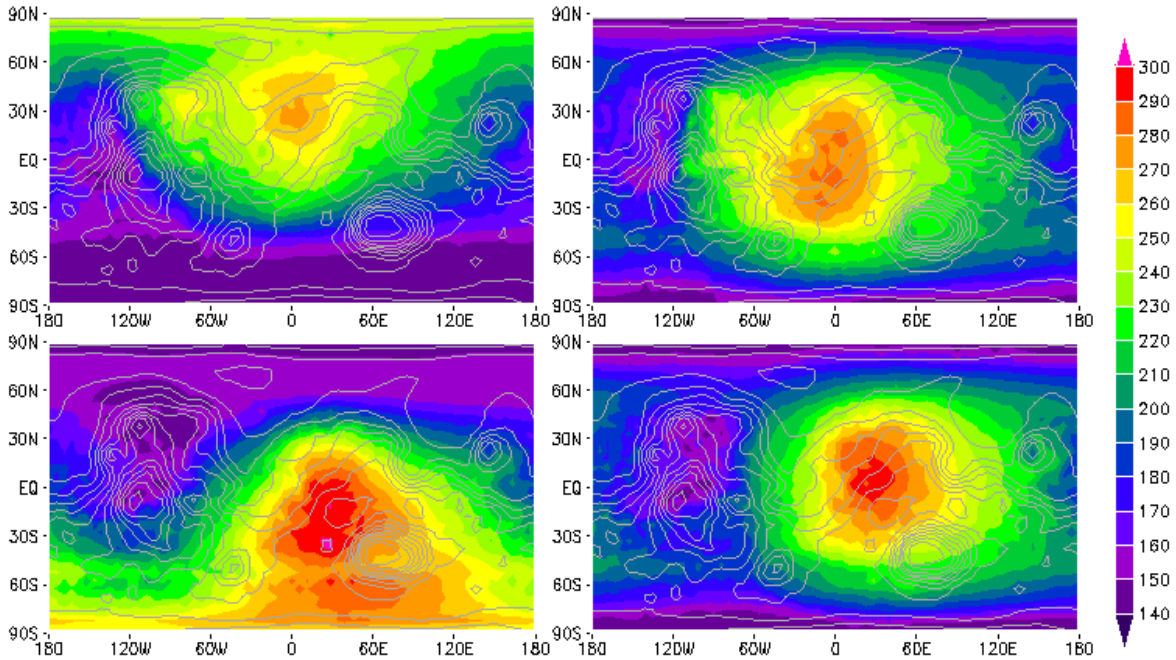

Figure 4.11: The snapshots surface temperature at the same time as Figure 4.10.

The near surface wind vectors (~50 m above surface) at Ls = 270^0 for the second simulated Mars year are shown in Figure 4.12. We can see strong winds along mountain slopes especially at the dust lifting areas mentioned above. The wind directions generated by GEM confirm that in the daytime winds blow up the valleys and mountain slopes, for example upward wind along Hellas (42.4°S, 70.5°E) in the afternoon in Figure 4.12; and at night the winds blow down mountain slopes, for example downward wind along Tharsis Montes (1.57°N, 112.58°W) at night in Figure 4.12.

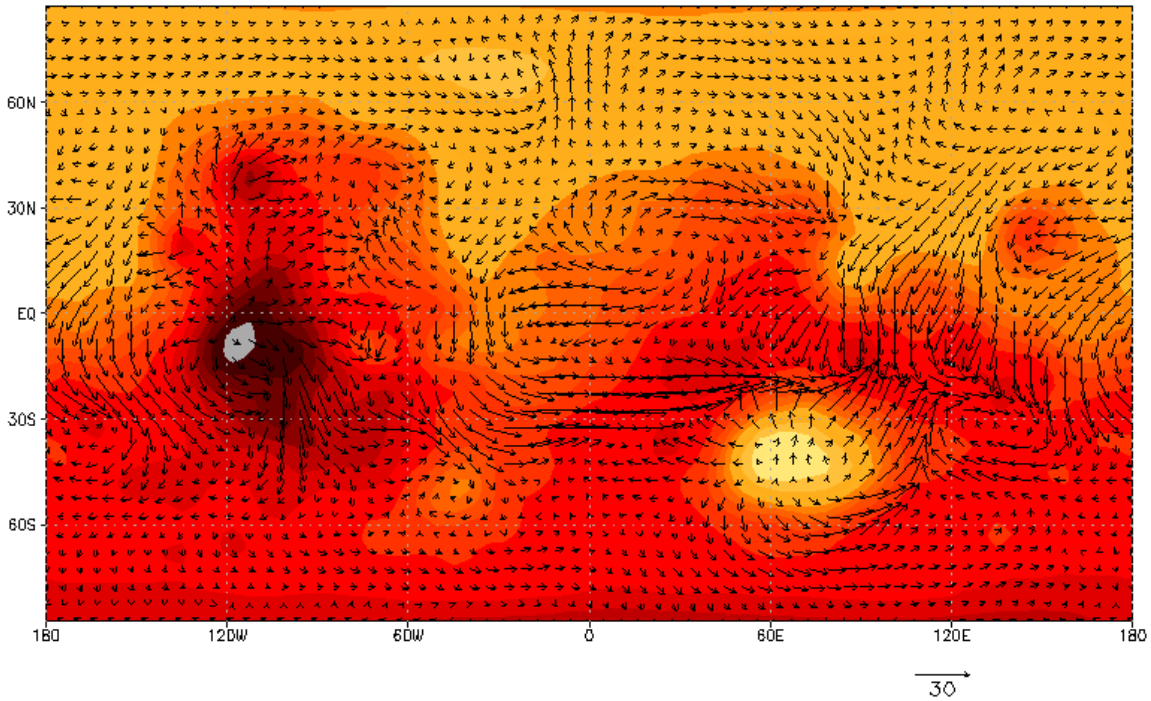

Figure 4.12: A snapshot of near surface winds for Ls = 270^0 (same time as bottom left panel in Figure 4.11) for the second simulated Mars year, local noon is around longitude 30^0 E. Topography is shaded in colors with grey is highest and decreases from red to yellow.

Figures 4.13 shows the snapshots of threshold friction velocity for saltation, deposited CO_2 ice, surface friction velocity, the magnitude of near surface wind with local noon at 30^0 E which is the same time as Figure 4.12. In the dust DEAD model, the condition of dust lifting is the surface friction velocity for saltation is greater than the threshold of saltation when surface temperature greater than CO_2 condensation temperature. The surface friction velocity (bottom left), and the wind magnitude of near surface wind (bottom right) in Figure 4.13 are greater in magnitude at the western and northern rim of Hella. In order to simulate the wind gust (is a sudden, brief increase in speed of the wind) in the DEAD model the GEM near surface wind are partitioned into 5 wind bins according to the Weibul

distribution and then a surface friction velocity for each wind bin is recalculated. A Weibull distribution represents how often the wind blows at a certain speed, demonstrated by weighted wind bins with more wind bins better way to represent the real wind speed distribution. The recalculated surface friction velocity in wind bins 4 and 5 are usually greater than the original GEM surface friction velocity and increase the chance and amount of dust lifted from surface. The thermal convection dust lifting scheme also considered as a cause of dust lifting. The maximum sensible heat area is around the local noon and afternoon.

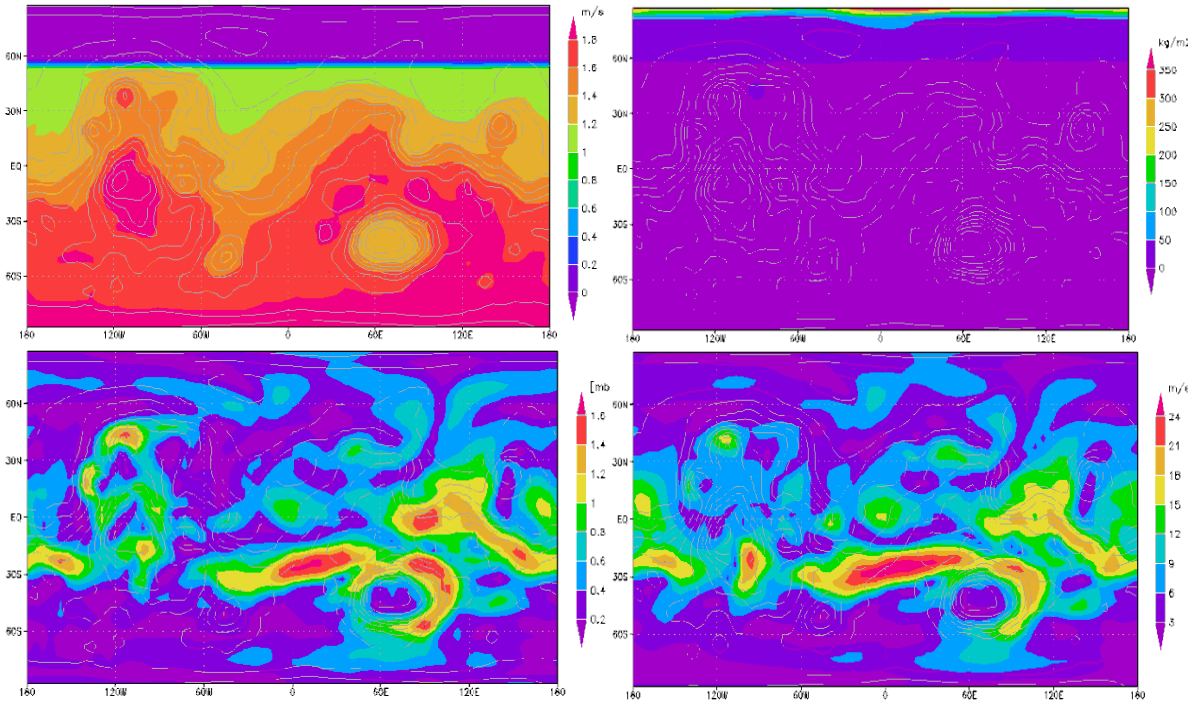

Figure 4.13: Snapshots for threshold friction velocity for saltation (top left), deposited CO_2 ice (top right), surface friction velocity (bottom left), and the wind magnitude of near surface wind (bottom right) with local noon at 30^0 E for Ls = 270^0. The topography is plotted as grey contours.

The values of dust mass mixing ratio address that the smallest dust bin 1 covers almost globally except for two polar regions and has the lowest mixing ratio values in the range of (2.5×10^{-7}, 6.5×10^{-7}); bin 2 covers less areas and the mixing ratio values are in the range of (3.5×10^{-6}, 5×10^{-7}); bin 3 has the highest mixing ratio values in the range of (8×10^{-6}, 1×10^{-6}); the largest bin 4 covers the least areas and the mixing ratio values are in the range of (6.5×10^{-6}, 5×10^{-7}). We see that the most lifted dust is represented by the dust bins 2, 3 and 4, and this result is consistent with the mass fraction M_j for each bin in Table 2.3.

In order to improve the accuracy of the simulation of GEM-Mars the tuning parameters in the DEAD model for mechanical dust lifting mass flux and saltation threshold have been tested in GEM-Mars. Our tests agree with the previous studies that it is relative easy to simulate dust storms in one season but it is difficult to simulate dust storms in a spontaneous way for years. To test the two tuning parameters GEM-Mars 3D model has run from isothermal atmosphere without dust for 30 sols (spin up time) at four different seasons (only mechanical dust lifting is used). We know that during the aphelion season ($Ls = 0^0 \sim 180^0$) there are less dust storms on Mars during the perihelion season of ($Ls = 180^0 \sim 360^0$) when usually large dust storms prevail. The parameters have been tested for four seasons around $Ls = 0^0$, 90^0, 180^0 and 270^0. The previous researches, such as Basu et al. [2004, 2006] and Kahre et al. [2006], a range value of fixed stress-thresholds and injection rates have been tested. Varying the thresholds and injection parameters, their models could develop a range of local and regional storms.

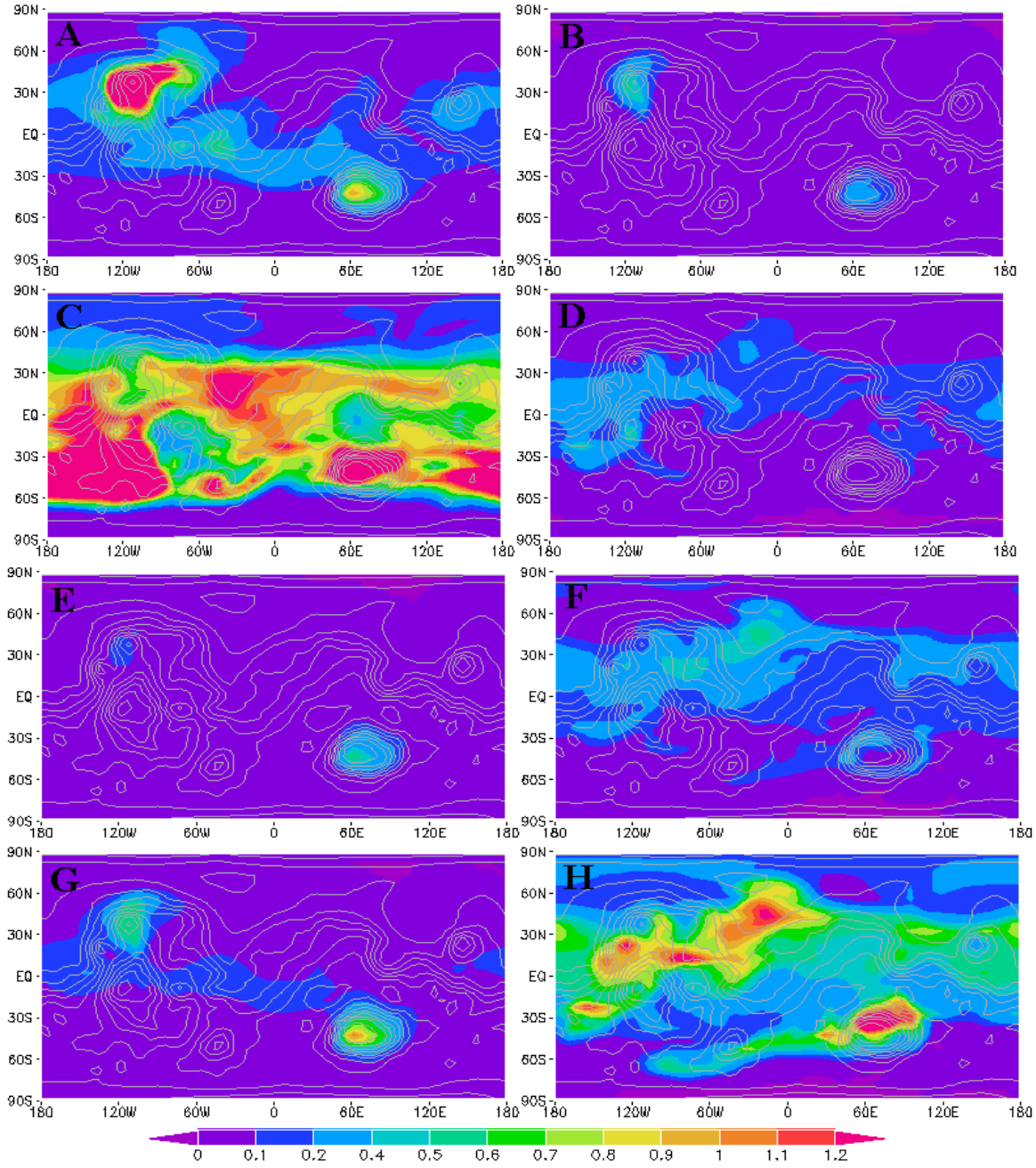

Figure 4.14: The snapshots of dust optical depths in the visible wavelength 0.63 μm for constant saltation friction velocity thresholds (A and C 1.7m/s; B and D 1.2 m/s); for variable saltation thresholds with inject tuning parameter (7×10^{-3} for E and G; 7×10^{-5} for F and H). A, C, E, and G at Ls = 90^0; B, D, F and H at Ls = 270^0

For GEM-Mars, firstly we tested several fixed saltation thresholds with a default injection lifting rate of value (7×10^{-4}) in the DEAD model as shown in Figure 4.14 A-D; secondly a range of injection rates were tested using a variable threshold scheme as shown in Figure 4.14 E-H. The results at Ls =90^0 (represents the aphelion season) and Ls = 270^0 (represents the perihelion season) are shown in left and right column in Figure 4.14 respectively. The discussions of the two testing scenarios are below:

1) The fixed saltation threshold for friction velocity

A global constant threshold at high value1.7 m/s is plotted in A and C and a low value 1.2 m/s in B and D with A and C for Ls = 90^0 B and D for Ls = 270^0. For the low fixed saltation threshold in the southern summer Ls = 270^0 (plot C in Figure 4.14) the large dust storms occur almost at all latitudes except for polar regions with the maximum dust optical depths above 1.2. But this low threshold doesn't work well for northern summer Ls = 90^0 (plot A in Figure 4.14). Although the dust coverage is much smaller than in the southern summer the regional dust storms with maximum dust optical depths greater than 1.2 appear in the northern hemisphere and around the equator which are not consistent with observations. In the previous studies, Basu [2004 and 2006] demonstrated that the high threshold and high injection rate are required to generate spontaneous and variable dust storms. A high saltation threshold 1.7 m/s is tested in B and D. The problem addressed in D (southern summer) is that dust is lifted in a much smaller regions and even when the dust lifting mass flux parameter is increased, there is still not enough dust coverage in the southern hemisphere. In plot B (northern summer) the dust lifting regions are the same as for the low threshold that focused on the north side of Olympus Mons and Hellas Basin.

From these tests we conclude that the differences in the dust optical depth for four seasons trend to decrease when we try to tune the threshold values for seasons. From plots A-D, the low and high thresholds do not work for both seasons but it seems that some threshold and some dust flux lifting parameter could exist suitable for all the seasons. Basu [2004 and 2006] did similar tests to find the tuning parameters to generate the dust cycle on Mars but their results of dust amount and optical depth do not quantitatively compare with observations. A series of threshold values between 1.2 and 1.7 m/s have been tested in the 3D GEM-Mars model. We find that it is difficult to tune the threshold for both aphelion and perihelion seasons, that is, if the threshold matches the right dust scenario in perihelion season it creates less dust in the aphelion season.

2) Variable saltation threshold with different mass flux lifting parameters

We adopt the calculation of saltation threshold built in the DEAD model to calculate the threshold value for each grid at every time step. The detailed calculation method is described in section 2.8.2. We don't need extra adjustment of the threshold with this method. To match the observations, the parameter of lifting dust mass flux has been tested for different values. The parameter of lifting dust mass flux multiplies the vertical mass flux obtained by equation (2.17) in section 2.8.2. The low lifting parameter value of 7×10^{-5} is shown in plots E and G and a high parameter of 7×10^{-3} is shown in F and H. Each parameter is tested for the aphelion season (Ls = 90^0) E and F, and for perihelion season (Ls = 270^0) G and H. In the plot G for the southern season the simulated dust optical depth is too low due to the low lifting parameter while in the plot H for the northern season the optical depth is relatively high for the northern hemisphere due to the high lifting parameter.

So several lifting parameter between 7×10^{-5} and 2×10^{-3} have been tested in GEM-Mars 3D with only mechanical dust lifting scheme at four seasons. Finally, a medium value 2.6×10^{-4} is used while the default value for earth is 7×10^{-4}. The variable threshold has its advantage that we just need to adjust one parameter instead of two parameters for a fixed threshold method. The result of variable threshold for both mechanical and thermal convection dust lifting schemes is presented in Figure 4.10 for four seasons. Figure 4.10 shows a dust cycle vary with time for one Mars year. We can conclude that the threshold calculated in the DEAD model for Mars dust lifting condition. In the next section 4.4 direct comparisons of dust vertical distribution with observations will be discussed.

4.4 The vertical dust distribution and vertical temperature profiles

4.4.1 GEM-Mars dust vertical profile comparing with prescribed dust profile

The vertical dust distribution directly affects atmospheric temperature and dynamics. Thus the proper representation of the dust distribution in the model is crucially important. The dust is lifted from surface by wind shear and dust devils, and further the lifted dust is split into four bins with different size ranges (as seen in Table 2.3). Dust is diffused vertically using the GEM diffusion scheme with vertical diffusion coefficients calculated from the turbulence scheme in GEM. The four dust bins are carried by four tracers and transported horizontally in GEM dynamics.

In the previous Mars GCM the vertical dust distribution is as prescribed by Conrath [1975] $q = q_0 \exp(v(1 - P_0 / P))$ where q_0 is the mass mixing ratio at the surface, v is the

ratio between the characteristic dust diffusion time and the characteristic dust sedimentation time at the surface (the Conrath parameter, v=0.01), P_0 is the reference pressure 700 Pa. Figure 4.15 shows the difference between the simulated vertical dust optical depth (Left) at the north-western rim of Hellas with dust optical depth about 0.98 around local noon with the prescribed dust optical depth, again with a total dust optical depth of 0.98 at the surface.

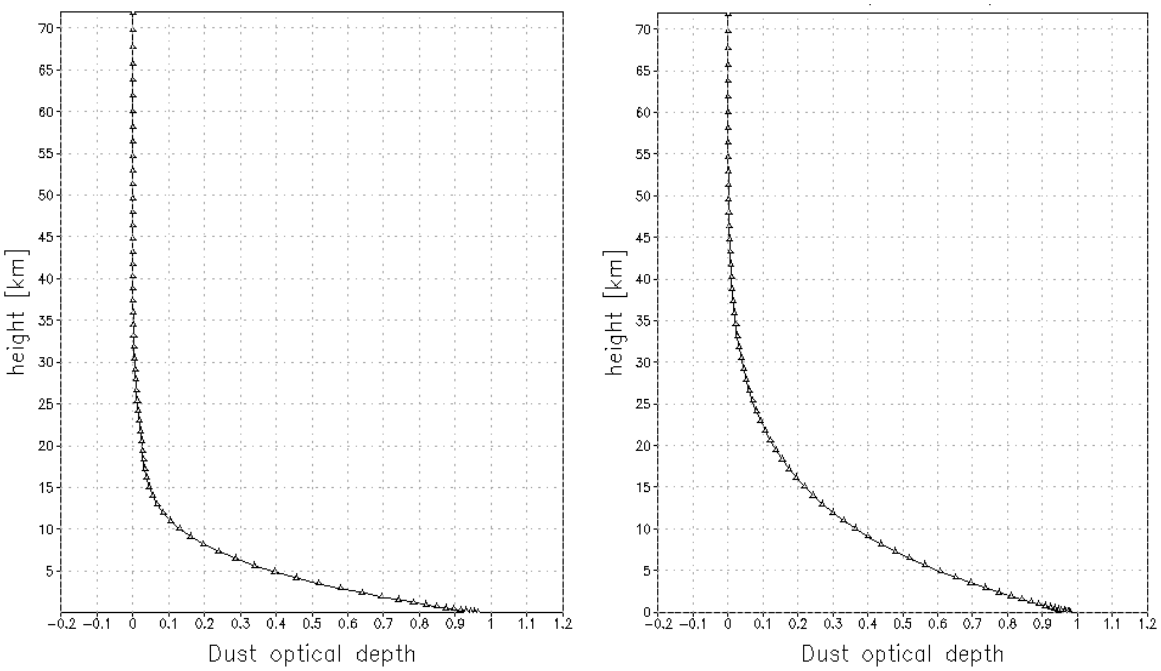

Figure 4.15: (Left) simulated vertical dust optical depth at visible band at local noon around Ls = 270^0 located at 35^0 S, 65^0 E (northwestern rim of Hellas) with dust optical depth about 0.98; (Right) prescribed dust optical depth with dust optical depth 0.98 at the surface.

The corresponding scaled simulated dust mass mixing ratio for all four dust bins at the same time and location is shown in the Figure 4.16 (Left), the simulated value is normalized (divided by 1.125×10^{-5}) so that the surface dust mass mixing ratio is scaled to 1. Comparing with the prescribed scaled dust mass mixing ratio in Figure 4.16 (Right), the

simulated dust mostly resides in low levels, mainly within the boundary layer, and the dust mixing ratio is almost a constant below 5km, and sharply reduced above 5 km. The simulated dust mixing ratio reaches to a minimum at about ~19 km, and increases up to 25 km then decreases gradually until to zero at about ~42km. By contrast the prescribed dust mixing ratio decreases gradually from surface until zero ~65 km. The prescribed dust distribution causes a greater dust optical depth in the vertical levels above 5 km, and further causes a warmer atmosphere in these levels.

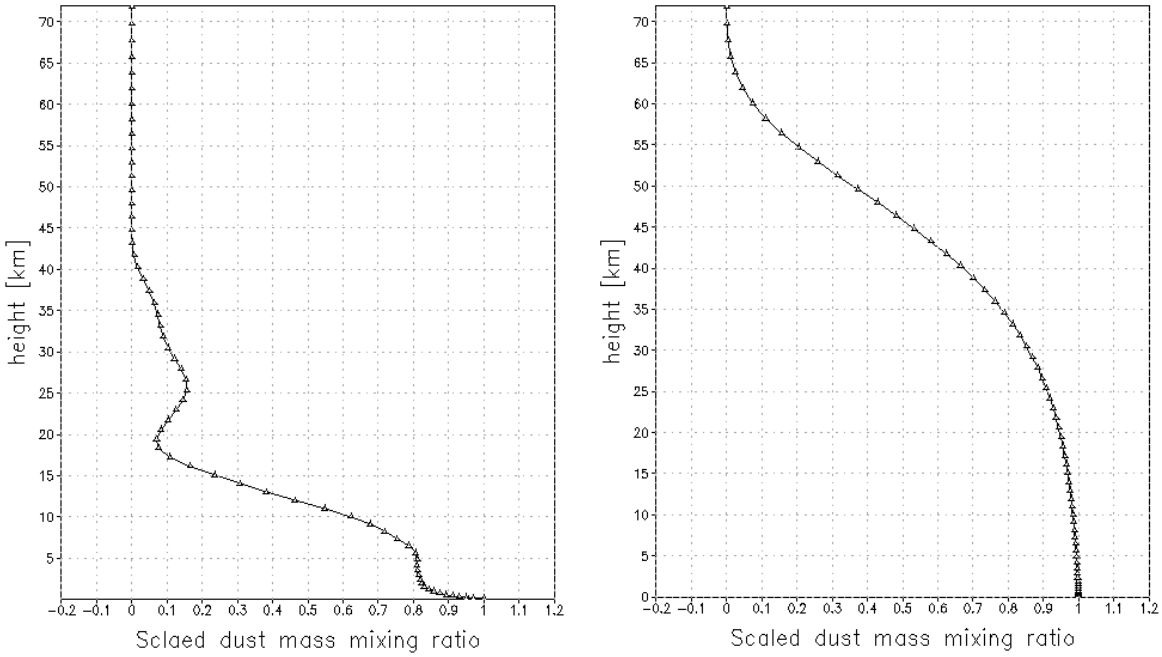

Figure 4.16: (Left) Scaled simulated dust mass mixing ratio for all four dust bins at the same time and location as Figure 4.15, dust mixing ration is divided by $1.1254e^{-5}$ so that the surface dust mass mixing ratio is scaled to 1; (Right) prescribed scaled dust mass mixing ratio

4.4.2 Comparison with MCS datasets

The Mars Climate Sounder (MCS) on mars Reconnaissance Orbiter (MRO) has been making global, vertical resolved observations of infrared radiance from Mars's limb, nadir, and off-nadir in nine broadband channels sensitive to dust, temperature, and other aerosol [McCleese et al. 2007]). Simultaneous retrievals from MCS limb observations of vertical profiles of temperature, dust and water ice are now available at the NASA Mars data archive website (http://pds-atmospheres.nmsu.edu/data_and_services/atmospheres_data/Mars/Mars.html). More recently, such as Guzewich et al. [2013a], Wang and Richardson [2015], Kavulich e al. (2013), Greybush et al. [2012], Madeleine et al. [2011,2012], and Steele et al. [2014 b] use a horizontal dust distribution derived from Mars Clime Sounder (MCS) observations in Mars year 30. These model studies use different approaches to represent dust vertical, such as Madeleine et al. [2011,2012] adopt a modified Conrath vertical profile to predicate accurate temperatures.

The vertical dust distribution is retrieved as dust opacity per unit height (the extinction dust optical depth per unit height) which is equivalent to the dust optical depth thickness divided by the height thickness between two vertical levels. In order to better present the vertical profile the dust opacity per unit height is scaled by air density and $\log_{10}$ is applied as proposed by Heavens [2011]. The results referred below to a particular season are in fact the average over day and night in the interval [$Ls-0.5^0$,$Ls+0.5^0$] for both MCS retrieved data and GEM-Mars output.

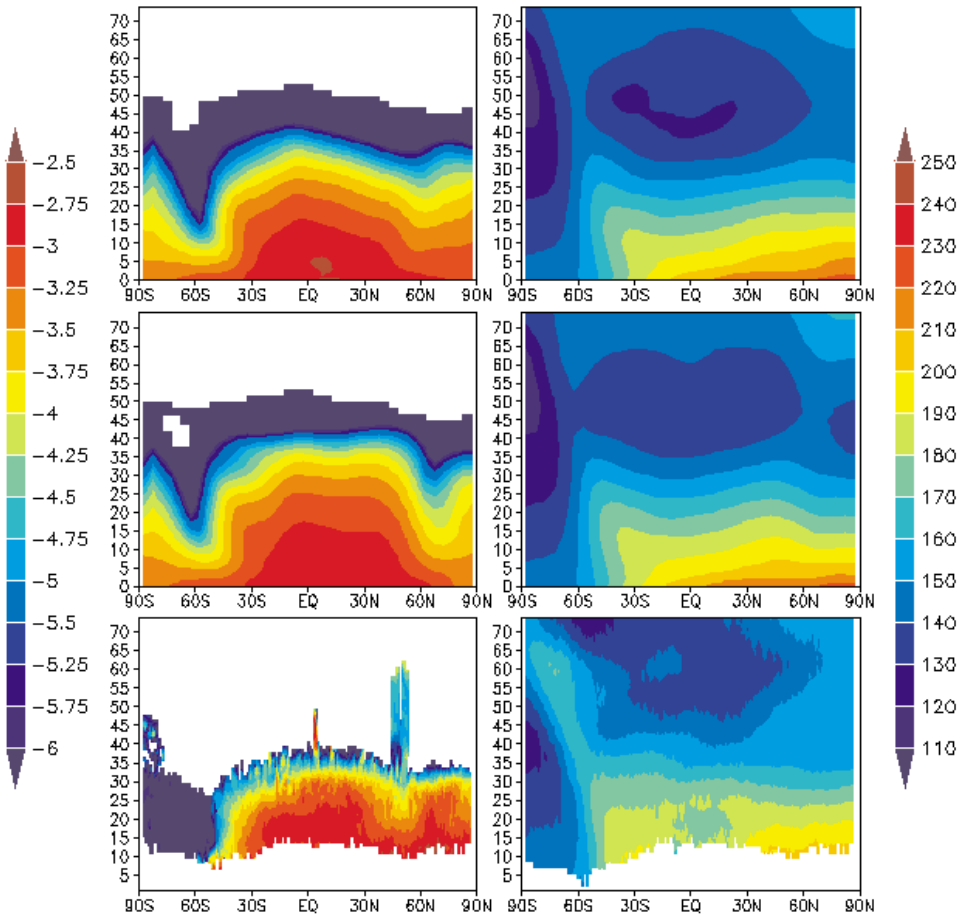

Figure 4.17: The $\log_{10}$ of zonal average and time average of density-scaled dust opacity per unit height (m^2/kg) for the 2nd simulated year (top left) and 3rd simulated year (middle left) versus MCS retrieved data (bottom left) which is at 463 cm^{-1} (wavelength 21.6 μm); zonal average and time average air temperature (K) for the 2nd simulated year (top right) and 3rd simulated year (middle right) versus MCS retrieved data (bottom right). The simulated dust opacity is scaled from visible band to IR band by multiplying a factor 0.5. The vertical axis is altitude in km. Time average is taking the day and night between Ls = 89.5^0 to Ls = 90.5^0 for MCS observations around June 2008 and the second and third year for GEM-Mars. In the bottom panels the white space at low altitude is missing data in the MCS retrieval.

The GEM-Mars results show an overall agreement in magnitude and pattern of the temperature and dust opacity for four seasons (from Figure 4.17 to Figure 4.20). Northern spring and summer are mostly free of dust storm seasons. The temperature discrepancies between observation and simulation in Figure 4.17 (Ls = 90^0) locate above southern polar region. The TES and MCS have observed that middle atmospheric temperatures (between 55 km to 70 km) over the south pole during northern summer are 10-30 K warmer than those predicted by most Mars climate models. In Figure 4.17 northern summer, the polar warming event is not simulated by GEM-Mars above southern polar region.

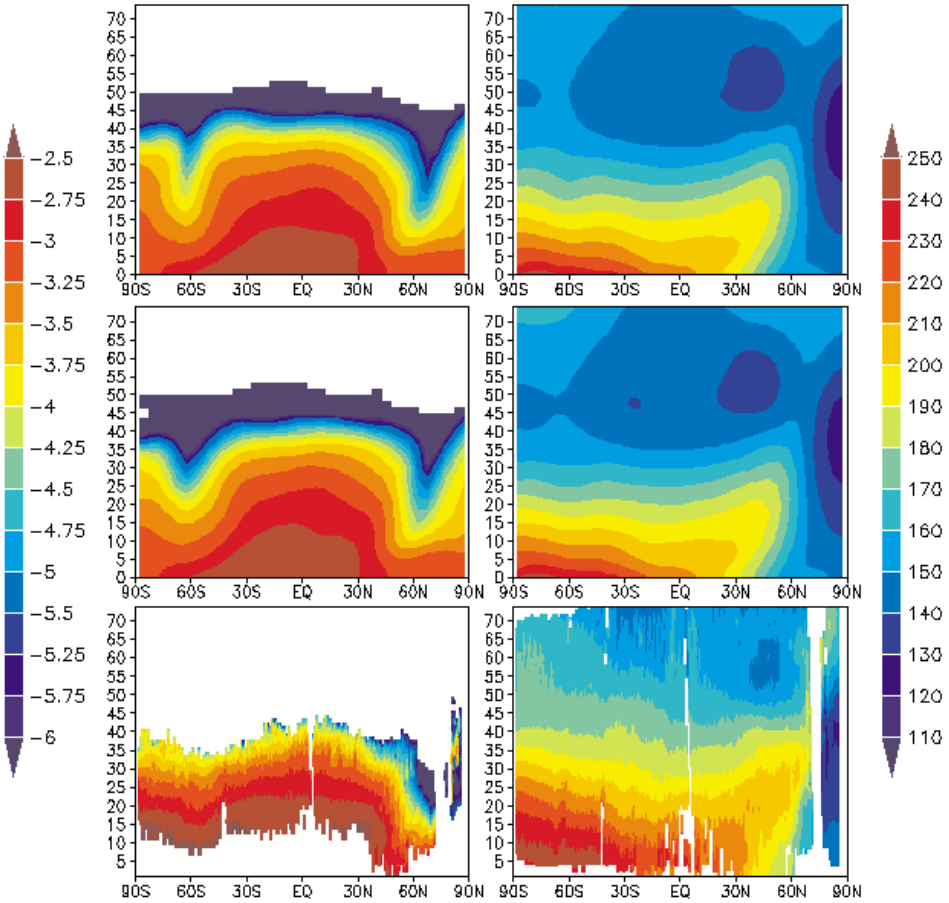

Figure 4.18: Same as Figure 4.17 but for Ls = 269.5^0 to Ls = 270.5^0

In Figure 4.18 the northern winter solstice observed temperatures are usually highest in the southern high latitudes, lower toward the tropics, and have a secondary maximum in the northern midlatitudes that tilts poleward at higher altitude (between 40-70 km). The simulated temperatures are lower than the observations at the same heights. Both observed and simulated dust is mainly restricted to the summer hemisphere and winter hemisphere tropics. The higher values of $\log_{10}$ of density-scaled dust opacity, in the range (-3, -2.5), reach up to 25~30 km in northern winter solstice (Ls = 270^0) which is higher than 20~30 km at northern summer solstice and 15~20 km in northern equinox fall and spring simulations. The vertical extent of density-scaled opacities from both observations and simulations are significantly deeper from 60^0S to 30^0N, indicating strong vertical and meridional mixing in the lower atmosphere at these latitudes. There is a minimum in dust density-scaled opacity at ~50^0S at 20 km. We infer this minimum is probably due to downwelling of atmospheric circulation above this location [Heavens 2011].

The thermal structure is very different between northern summer and northern winter. Both observed and simulated temperatures throughout atmosphere are warmer at northern winter solstice than northern summer solstice. For the observed temperature below 35 km and simulated temperature below 20 km at northern winter solstice (Figure 4.18) are highest in the southern hemisphere, decreasing toward northern hemisphere, and have a secondary maximum in the northern hemisphere above the midlatitudes that tilts poleward at high altitudes.

Again the MCS observations show a middle atmospheric (50~60 km) polar warming near north pole is ~180 K. The temperature of this region exceeds temperature at the same

levels at other latitudes, but there is no dust or water ice and with no or limited solar insolation at this region, so it can be inferred that this warming is not caused by radiative adiabatic heating. Heavens et al, [2011] suggest that a downwelling is inferred for this polar warming. As we know that an air parcel is forced to rise (sink) in the atmosphere, it will cool (warm) adiabatically. Therefore, in the absence of diabatic heating by absorption of visible and infrared radiation by aerosols or trace gases species departure of temperatures from radiative equilibrium directly indicates upwelling and downwelling driven by dynamical processes [Heavens, 2011].

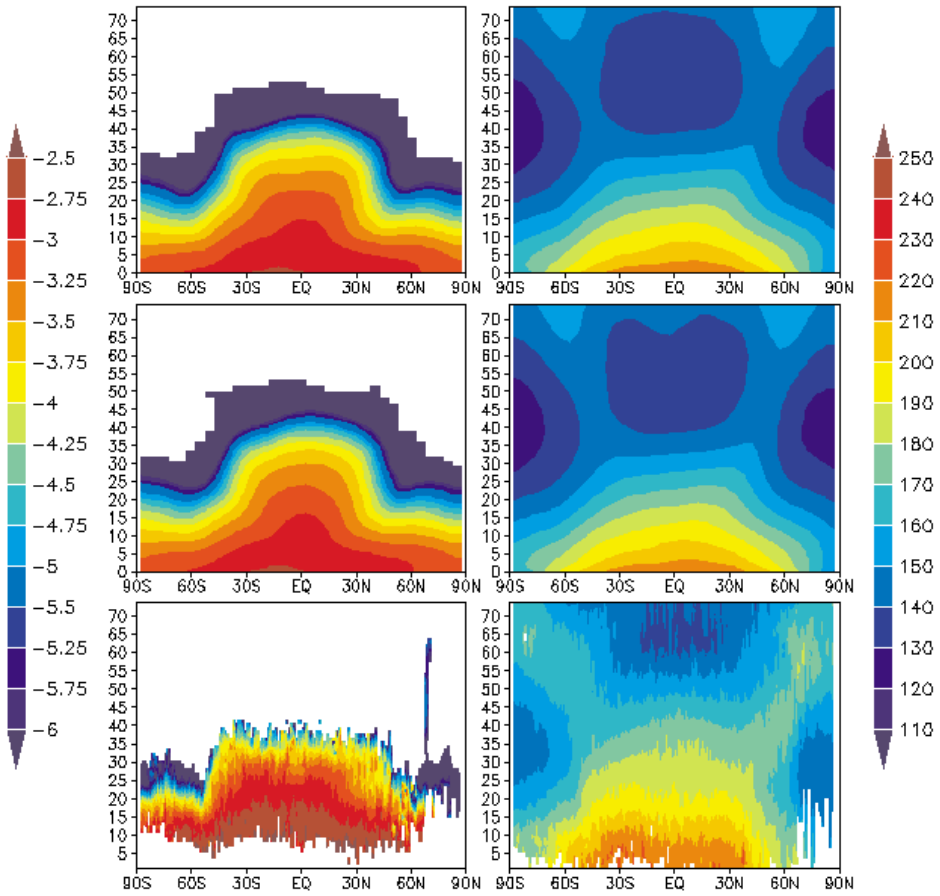

Figure 4.19: Same as Figure 4.17 but for Ls = 359.5^0 to Ls = 0.5^0

The polar warming at this season also simulated by Forget et al. [1999] shows this polar warming is the results of a fully kinematically coupled lower and middle atmospheric meridional circulation. From our result (Figure 4.26, right bottom) the simulated mass streamfunction indicate that a fully kinematically coupled lower atmospheric circulation above north pole up to 80km (positive, equator-ward) with middle atmospheric circulation south of 60^0S (negative towards north pole). The coupled interface across this region results in a warming between 60~80 km above north pole due to downwelling and cooling from the surface up to 60 km due to upwelling.

The dust distribution at both equinoxes Ls = 0^0 (Figure 4.19) and Ls = 180^0 (Figure 4.20) are relatively symmetric about the equator. Both observed and simulated density-scaled opacity are greater and approach higher altitudes above the equator than at the two poles. The observed dust density-scaled opacity is higher in the tropical atmosphere at Ls = 0^0 than Ls = 180^0, and we can find this difference in Figure 4.19 and Figure 4.20. Simulated dust density-scaled opacity appears to have very similar pattern at Ls = 0^0 and Ls = 180^0. Dust density-scaled opacities at 10 km are relatively similar from pole to pole, but the vertical extent of dust is significantly deeper from 50^0 S to 50^0 N for both observations and simulations. The MCS measurements show relative higher values than simulated values in the lower levels up to 20 km above the equator and up to 10 km and 60 latitudes in both hemispheres. There is a minimum in dust density-scaled opacity at ~50^0S at 25 km for Ls = 0^0 and at 20 km for Ls = 180^0 in both measurements and simulations.

The observed temperature structure at northern spring equinox (Ls = 0^0, Figure 4.19) is very similar to the northern fall equinox (Ls = 180^0, Figure 4.20), except that the high

latitudes at ~30 km and tropics at ~50 km are warmer. The simulated temperature at high latitudes becomes warmer at higher altitudes above ~65 km at Ls = 0^0 and above ~60 km at Ls = 180^0, and is about 20 K lower than observed temperature. The simulated temperature at the tropics is about 10~20 K lower than observed temperature at the same levels due to the simulated dust is less and dust can warm up the ambient air by absorption and scattering solar radiation.

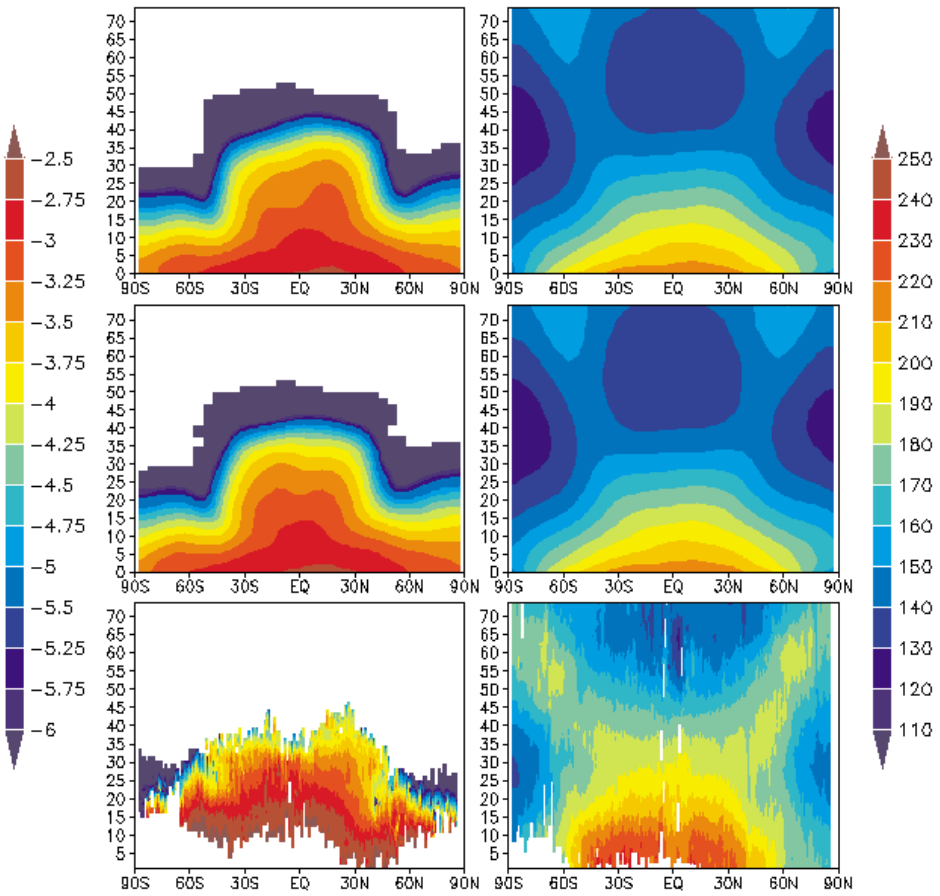

Figure 4.20: Same as Figure 4.17 but for Ls = 179.5^0 to Ls = 180.5^0

4.5 Comparison with Phoenix datasets

Phoenix landed in the Green Valley of Vastitas Borealis within northern polar region on May 25, 2008 , i.e. in the late Martian northern hemisphere spring (Ls = 76.73^0) in Mars Year 29 (MY 29). The datasets downloaded from Mars Data Archive (http://atmos.pds.nasa.gov/data_and_services/atmospheres_data/Mars/Mars.html) include surface pressure and air temperature for sols 1-150 from Meteorological Station (MET), atmospheric opacity for sols 1-151 from the Surface Stereo Imager (SSI), and an atmospheric temperature entry profile from Atmospheric Structure Experiment (ASE). A light detection and ranging (LIDAR) on board the Phoenix lander was designed for measuring the vertical distribution of atmospheric dust and ice clouds up to heights of 20km. The Canadian Space Agency was responsible for the development of the MET and LIDAR instruments with the support of York University, DMA and Optech for specific development of the LIDAR.

The Phoenix lander has dimensions ~ 5.5 m long with the solar panels deployed, the science deck 1.5 m in diameter, from the ground to the top of the MET mast about 2.2 m tall. The lander was located in the northern arctic region (68.22^0 N, 234.25^0 E). The GEM-Mars model has a coarse horizontal resolution 5.625^0 by 5^0 (1^0 ~59.3 km in the equator, 1^0 ~22 km at latitude 68.22^0 N) and the output from GEM-Mars is considered as the average within each horizontal grid. The output is used here is the average over 124 km by 110 km centered at (67.5^0 N, 236.25^0 E) that is the closest to the Phoenix lander location.

4.5.1 Comparison with atmospheric dust optical depth

The retrieved dust optical depths from Phoenix Lander's Surface Stereoscopic Imager (SSI) of the Sun at wavelengths of 451 nm, 671 nm, 887 nm, and 991 nm are compatible with each other for the atmospheric dust optical depths from sol 3 (~Ls = 78^0) to sol 150 (~Ls = 148^0). In Figure 4.21 the measured dust optical depth of wavelength at 451nm during the daytime (1000-1800) and simulated by GEM-Mars from three Mars years are also plotted. The simulation is over much larger area than the in-situ measurements. The measurements are quite variable from 0.18~0.85 while the simulated for three years show much less variations with time in a range 0.15 ~0.26. During the latter half of Phoenix mission (after sol 80), there were nearly always clouds at the top of the boundary layer in the early morning hours that obscured the observations of dust at heights below 5 km [Komguem et al. 2013]. The variable optical depth in early portion of Phoenix mission was due to water-ice cloud [Moores, 2015]. In order to obtain the optical depth only due to dust daytime except for the early morning (1000-1800) observed data is plotted in Figure 4.21 because in the current GEM-Mars there is no clouds formation scheme. Figure 4.21 shows that the observed high opacity values (can approach as high as 0.7~0.8) and simulated values reach just about the baseline of the observed optical depths.

It has been observed by Hubble Space Telescope that dust activities occurred near the edge of the retreating north polar cap regions. High dust optical depths at high latitudes near north polar cap in the summer hemisphere also have been observed by TES [Montabone, 2015]. Numerical simulations have demonstrate that there would be enhanced dust lifting due to strong wind speeds and weather activity driven by the thermal contrast at

the polar cap edge [Komguem et al. 2013]. The lower simulated dust optical depth by GEM-Mars model probably occurs because it cannot properly simulate CO_2 ice coverage and durations for both poles resulting in the smaller thermal constant and less wind speed near the north polar cap. Furthermore, the small scale local dust storms or dust devils at Phoenix landing site cannot be simulated due to unresolved subgrid-scale wind and unresolved subgrid-scale sensible heat flux.

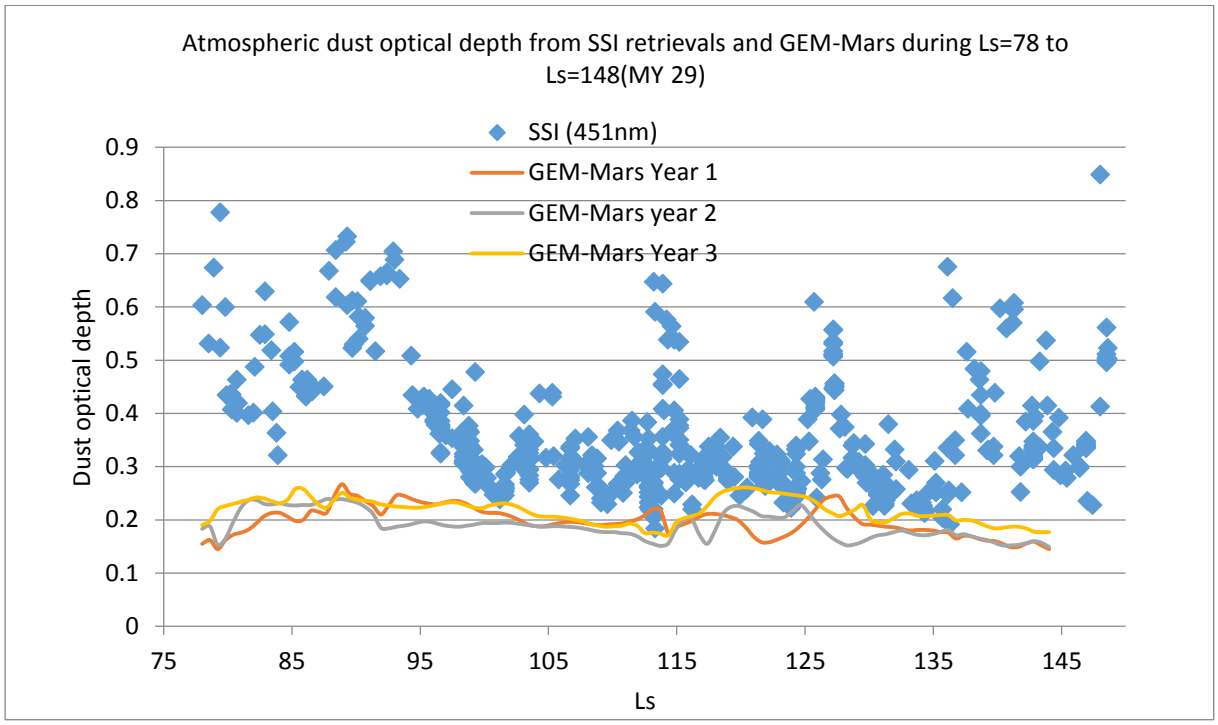

Figure 4.21: Atmospheric dust optical depth measurements obtained from Phoenix Lander's Surface Stereoscopic Imager (SSI) of the Sun at wavelengths of 451 nm for Mars Year 29 and simulated dust optical depth for three Mars years

4.5.2 Comparison with LIDAR measurements

Since the posted LIDAR data is the average signal voltage per height bin rather than dust opacity, a direct comparison of the dust vertical profile with the published paper by L. Komguem et al. [2013] for sol 48 is shown below. In Figure 4.22 the plotted extinction coefficient in unit (km^{-1}) is equivalent to the dust opacity per unit height. The comparison focus on the nighttime (21:00-24:00) around Ls = 98.3^0, GEM-Mars averaged extinction coefficient is only about half of the measurement (0.03 vs. 0.065) values. GEM-Mars density-scaled extinction is about one third of that measured (0.005 vs. 0.0015). The measured dust opacity (around local mean solar time 22:00) decreases gradually below 4 km and decreases rapidly above 4 km. The simulations show a similar dust vertical decay but with much smaller amounts and less vertical variation.

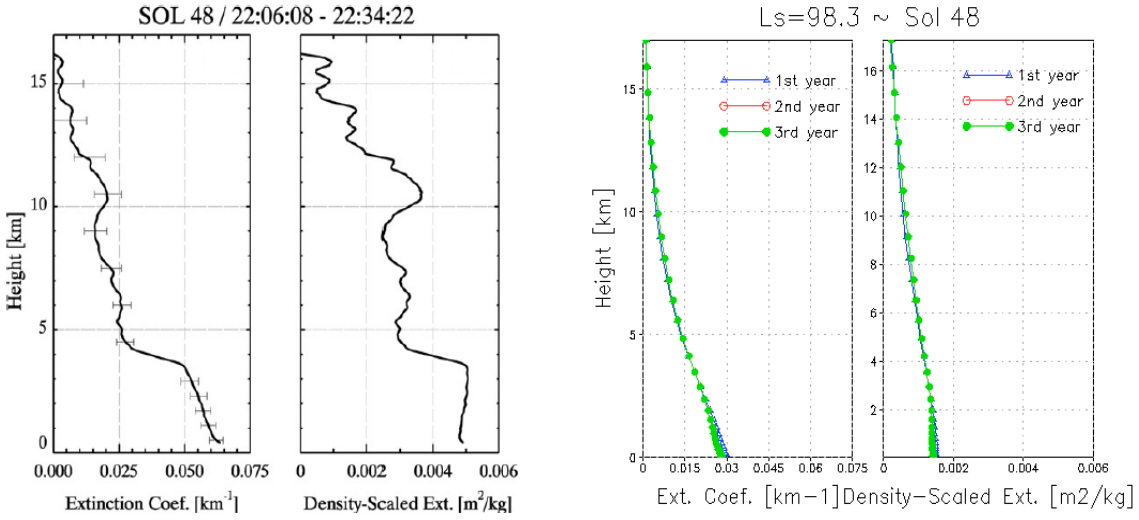

Figure 4.22: Dust extinction coefficient and density-scaled extinction coefficient retrieved at wavelength 523nm on mission sol 48 ~ Ls = 98.3^0 (Left, cited from Komguem et al. [2013]) simulated (Right) at Ls = 98.3^0 for three Mars years.

In GEM-Mars the dust source is assumed unlimited globally except for ice covered areas. Our simulated showed that mass transported by general circulation (Hadley cell) as shown in Figure 4.26 and 4.27, where dust can be transported from low latitudes to high latitudes, and cross equator arriving to the other hemisphere in the summer. The dust previously settled there in high latitudes is injected into atmosphere when CO_2 ice was sublimating from the polar cap [Komguem et al. 2013]. The atmospheric dust loading was a maximum during the first 40 sols of the Phoenix mission, in the period around summer solstice. The observations from Mars Color Images show that a dust clouds passing over the Phoenix site on mission sol 25 followed a trajectory a trajectory that tracked back to the polar ice cap. But in GEM-Mars there is only about half of the observed dust obtained for the Phoenix mission period. As mentioned in the previous section the dust lifting activity along the edge of retreating ice cap is not captured in GEM-Mars. And if even there is enough wind speed across the edge of ice cap the dust is not allowed lifted from the surface over ice in GEM-Mars.

4.5.3 Comparison with entry data from ASE

During the entry, descent, and landing phase of the mission, atmospheric data were collected by Atmospheric Structure Experiment (ASE) in order to determine the first profiles of atmospheric density, pressure, and temperature from a Martian polar region. The simulations was chosen at the Phoenix landing site 68.22^0 N, 234.25^0 E around Ls = 76.73^0 to compare with the measured data. Figure 4.23 temperature profile (left), temperature pressure (right top), and density (right bottom) are shown, both measurements and

simulations. There is about 20 K different in atmospheric temperature around 50 km, 60 km, 70 km and deviations between 100 and 130km.

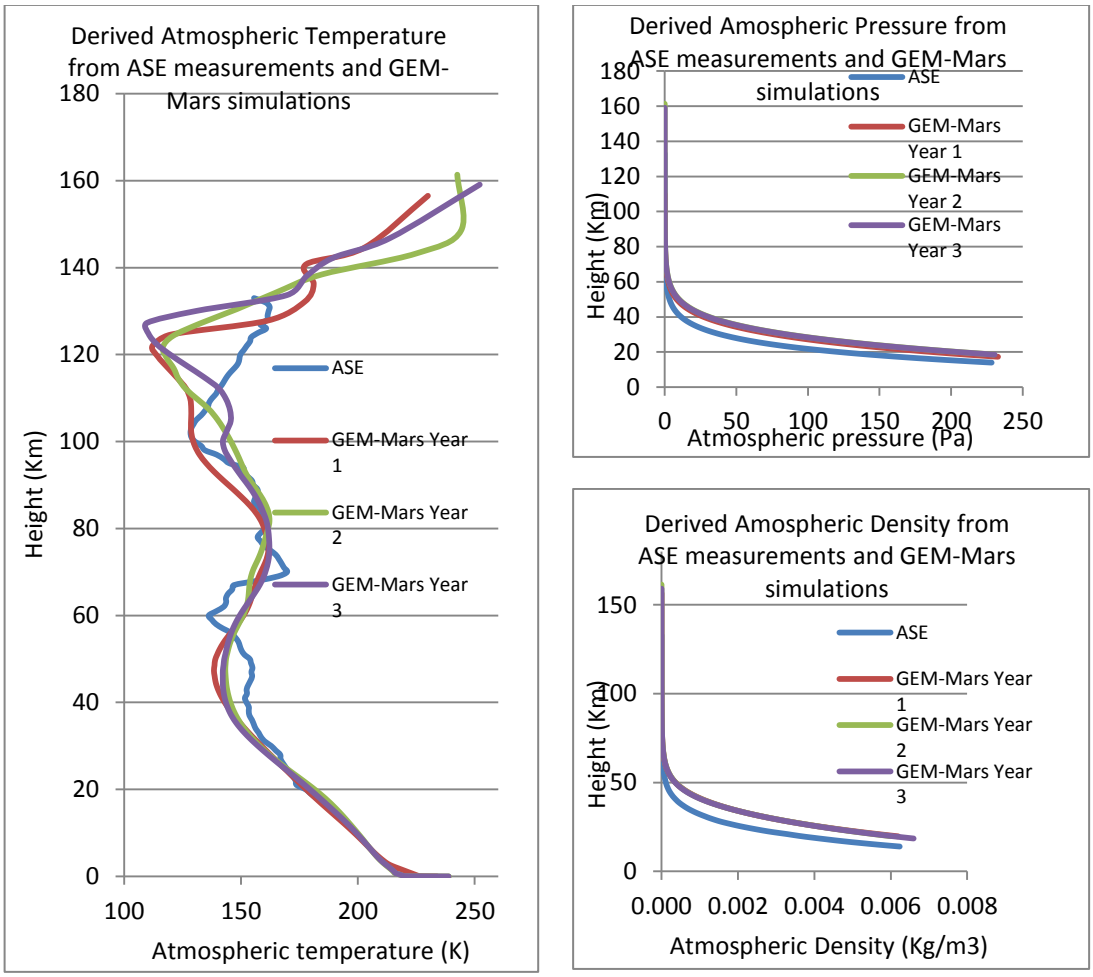

Figure 4.23: Comparison of retrieved temperature (left), pressure (right top), and density (right bottom) profiles from Phoenix entry datasets with GEM-Mars simulations for three Martian years at landing location 68.22^0 N, 234.25^0 E around Ls = 76.73^0

For the upper atmosphere radiative energy is balanced by UV-EUV absorption, CO_2 cooling and molecular diffusion. Above 80 km a non-local thermodynamic equilibrium (non-LTE) CO_2 cooling rates replace the CO_2 cooling rates from the surface up to 80 km

since in the upper levels CO_2 molecular collisions become too infrequent to maintain the local thermal equilibrium. The molecular diffusion is replaced by the GEM diffusion scheme. GEM-Mars atmospheric pressure is ~30 Pa higher than measurements at 20 km so atmospheric density ~0.002 kg/m3 higher at 20 km. The simulated pressure and density are higher than measurements in all levels. The reason of the higher pressure results from that the simulated CO_2 ice deposition is less than the reality. We also note that measurement is a single sample and that there may be substantial spatial and temporal variability.

4.5.4 Comparison with near surface temperature from MET

The simulated two diurnal surface temperature cycles for two Sols at Ls = 105^0 for the Phoenix lander location range between 215 K and 250 K in Figure 4.24. The measured near surface temperature at 0.25 m is significantly lower (~195 K) at night while daytime high temperatures are close (~250 K) to the modeled values. The measured temperatures at 0.5 m and 1 m are little bit lower than temperature at 0.25m. The simulated surface temperature is warmer (~20 K) than the measurements at night in the northern polar region.

The surface heat budget and surface temperature is discussed in section 3.3 for the Phoenix landing site at Ls = 90^0 using GEM-Mars 1-D model. The surface temperature is determined by the ground heat flux which is the sum of solar heat flux, infrared heat flux and sensible heat flux. The reasons that the simulated surface and near surface temperature are warmer than observed ones especially for the evening and early morning may be due to the simplified surface forcing scheme that may not accurate enough for artic regions. The Phoenix found the presence of water ice under the surface at the landing site. The ground

heat flux can be diffused/conducted downward especially the presence of ice direct below therefore the less ground heat flux left on the surface and results in the lower surface temperature than the simulated one.

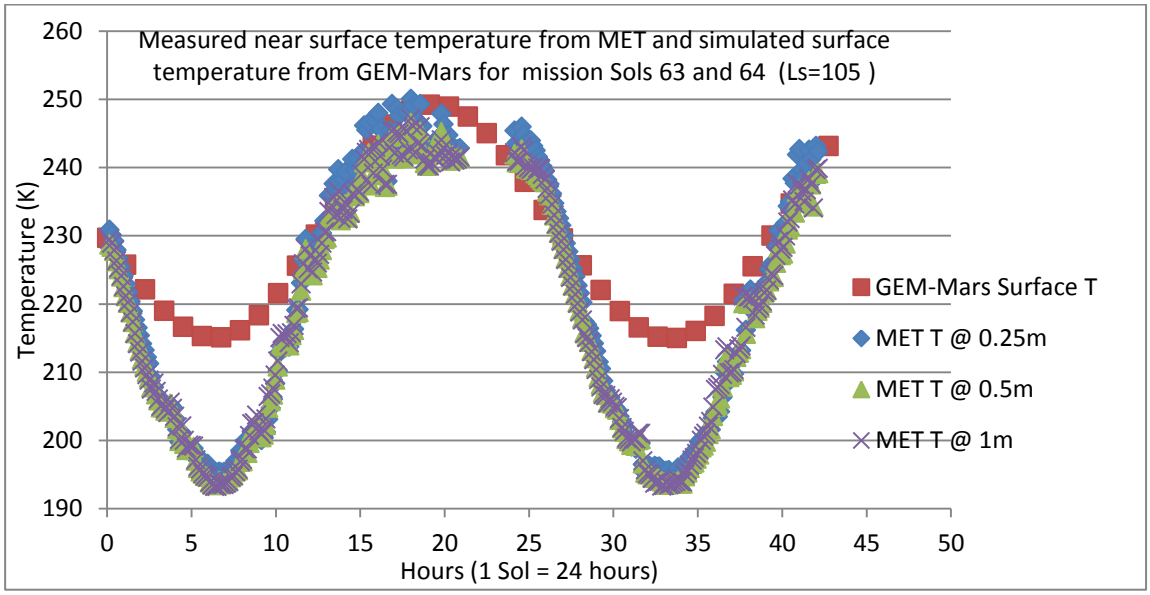

Figure 4.24: Comparison retrieved temperature from MET at 0.25 m,0.5 m, and 1 m with surface temperature from GEM-Mars third year simulation at Phoenix landing location 68.22^0 N, 234.25^0 E around Ls = 105^0

From the tests in section 3.3 we conclude that more suspended dust in the air turns in the lower surface and near surface temperature. From Figure 4.21 we see that the dust optical depth simulated by GEM-Mars is generally less than observed values, furthermore, the ice clouds optical depth during the evening and early morning is neglected in the GEM-Mars model, so that the simulated total optical depth is less than the reality on Mars especially at night and early morning.

4.5.5 Cross section above Phoenix lander location from GEM-Mars

Vertical cross sections, with topography, along longitude 125^0 W (Phoenix lander at 68.22^0N) at Ls = 90^0 for air temperature (K), wind magnitude (m/s), dust opacity per kilometer and density scaled dust opacity (m^2/kg) are plotted in Figure 4.25.The plots are for daytime (1500-1800) during the third Mars year from GEM-Mars.

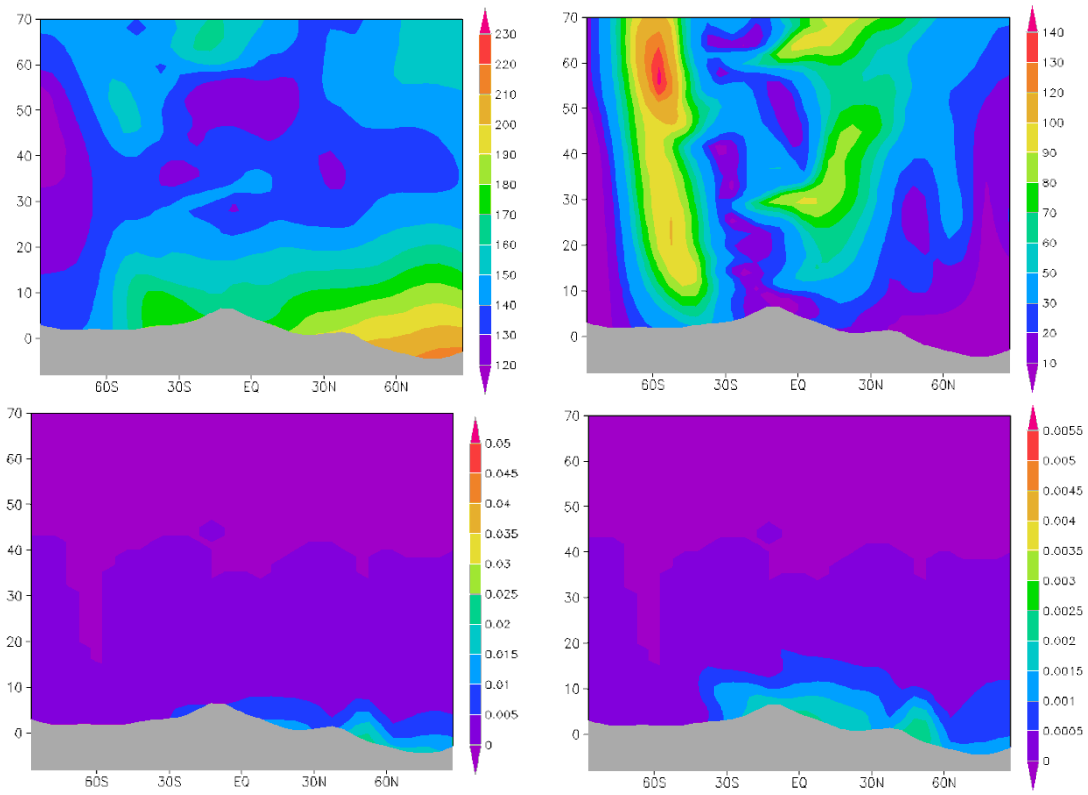

Figure 4.25: The cross section with topography along longitude 125^0W (Phoenix lander at 68.22^0N) for air temperature in K (top left), wind magnitude in m/s (top right), dust opacity (bottom left) and density scaled dust opacity (bottom right) at third Mars year Ls = 90^0 from GEM-Mars. The vertical axis is altitude in km.

The near surface air temperature at the lowest vertical level in GEM-Mar (between 30 and 50 m above the surface) is below 230 K, the modelled magnitude of wind at the same

level is below 10m/s, and we can see from Figure 4.25 that the wind speed is greater in southern hemisphere. The dust opacity and density-scaled opacity reach a maximum around 50^0 N with maximum 0.03 km^{-1} and 0.0025 m^2/kg respectively. The maximum values of dust opacity and density-scaled opacity in Figure 4.25 are lower than the measurements in Figure 4.22. The density-scaled opacity (an indicator of dust mass mixing ratio) can reach as high as 20 km above equator.

4.6 Zonal mean structure and global circulation of the Martian atmosphere

To study the circulations of the atmosphere the zonal-mean circulation and mean meridional circulation are plotted. The zonal mean is usually obtained by taking the average over both longitude and time. The following zonal mean is taking the time average over 10 sols around each season at Ls = 90^0, 180^0, 270^0 and 0^0 in the third simulated Mars year. The mean meridional circulation can be described by a mass streamfunctoin, which is defined by calculating the northward mass flux above a particular pressure p, as given in equation (4.1) with latitude φ, polar radius a = 3376.2 km, gravity 3.72 m/s^2, and zonal average meridional wind [v].

$$\psi = \frac{2\pi a \cos\varphi}{g} \int_0^p [v] dp \tag{4.1}$$

The simulated zonal mean atmospheric temperature shows the main features and is comparable with previous simulations (Richardson et al., 2007; Moudden et al., 2005, Forget et al. 1999). For the top atmosphere above 150 km, temperature is relatively high

mainly due to solar UV-EUV heating. Below 50 km temperature is balanced by the absorption and scattering by dust in solar and IR wavelengths, and CO_2 IR cooling. Between 50 km and 150 km CO_2 IR cooling and CO_2 near IR heating control the temperature.

The mass streamfunction is commonly known as the meridional overturning circulation. The mean meridional circulation dominates the low latitudes and is characterized by a deep Hadley circulation, which undergoes significant seasonal variation in structure and intensity. At the equinoxes, two roughly symmetric Hadley cells develop that share a common rising branch centered at nor near the equator. At the solstices, a single cross-equational circulation Hadley cell dominates.

Using a sufficient deep domain, GEM-Mars is able to simulate a polar warming event which is supposed to be caused as a result of convergence over the pole with concomitant subsidence [Wilson 1997]. In Figure 4.26 we can see warmer air above 60 km over the north polar region in north winter solstice Ls = 270^0. This warming results from a convergence of mass above the polar region and forces a descent into the polar region and an adiabatic warming at much lower altitude [Forget 1999]. The mass convergence can be seen in Figure 4.26 that shows negative mass streamfunction clockwise and positive counterclockwise meet for Ls = 270^0 above the north polar region. There is strong negative (downward) vertical velocity and meridional velocity descends toward the north pole above 100 km. The dynamics are also strongly influenced by resolved waves from below [Akingunola, 2009] but the current model does not include gravity wave drag.

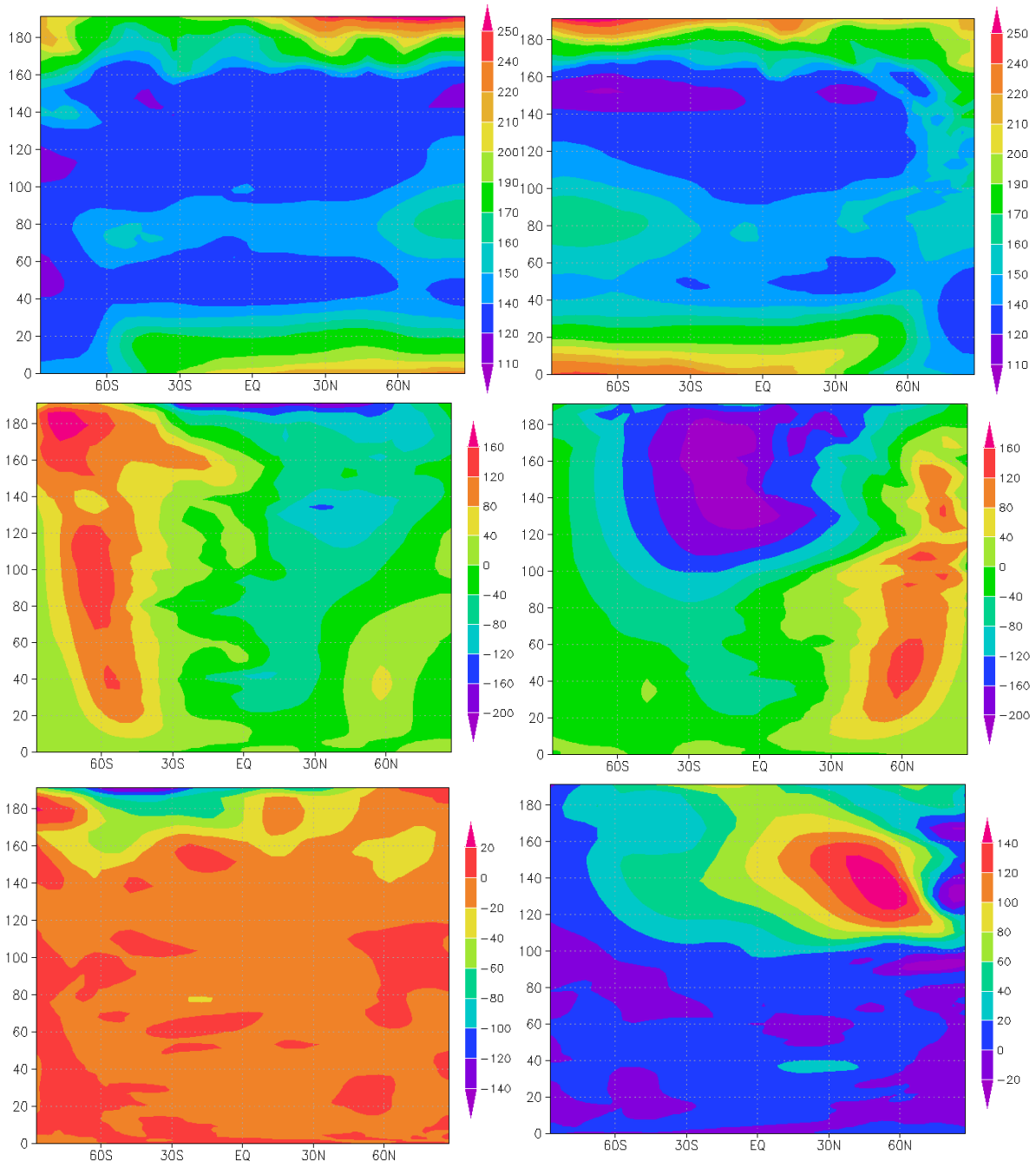
180
160
140
120
100
80
60
40
20
0
60S
30S
EQ
30N
60N
250
240
220
210
200
190
170
160
150
140
120
110
160
120
80
40
0
−40
−80
−120
−160
−200
20
0
−20
−40
−60
−80
−100
−120
−140

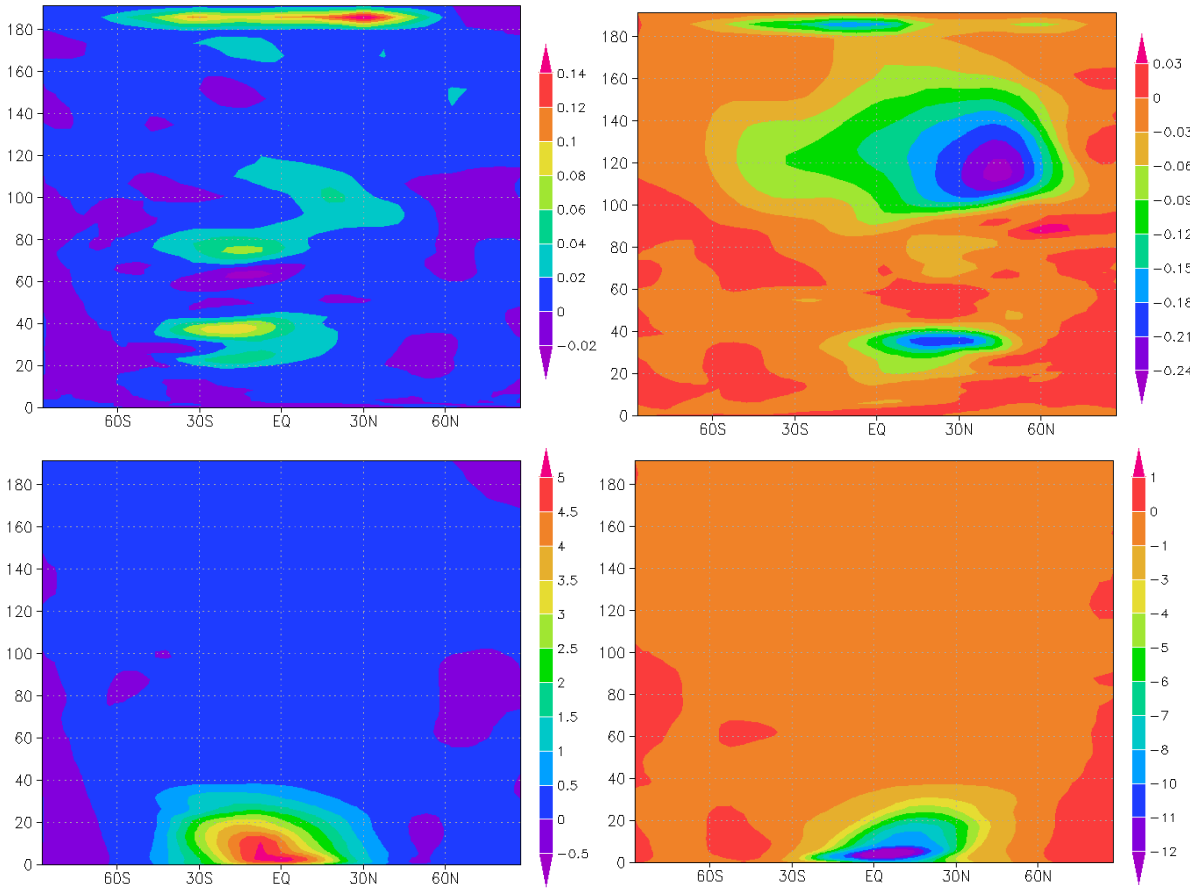

Figure 4.26: Latitude–height cross section of zonal mean atmospheric temperature (K), zonal wind (m/s), meridional wind (m/s), vertical wind (m/s) and mass streamfunction (10^9 kg/s) from the top panel to the bottom in sequence. Left column for Ls = 90^0 and right column Ls = 270^0. The vertical axis is altitude in km.

The zonal-average meridional and vertical components of wind are much weaker than the zonal wind. In Figure 4.26 the mean zonal winds are larger than 100 m/s in most regions for both seasons, while the mean meridional winds are less than 20 m/s except for higher altitude above 100 km and they are stronger in Ls = 270^0. The mean vertical wind is typically a hundred times smaller than the mean meridional wind. The mass streamfunction

in Figure 4.26 shows that the meridional circulation is dominated by a quasi-global Hadley cell which is clockwise in Ls = 270^0 and anticlockwise in Ls = 90^0. The magnitude of the circulation is more than twice as strong at Ls = 270^0 than in Ls = 90^0. This Hadley circulation results from a pole to pole heating gradient. The Hadley circulation simulation is comparable in both shape and magnitude with other simulations [Forget et al. 1999; Moudden et al. 2005].

Figure 4.27 shows the zonal mean states of the atmosphere in the model during northern spring Ls = 0^0 and fall Ls = 180^0.The main feature of the circulation is the domination by two Hadley cell, i.e. one clockwise in the northern hemisphere and one anticlockwise in the southern hemisphere. This circulation feature is also comparable with other simulations (Forget et al. 1999; Moudden et al. 2005).There is a strong retrograde zonal jet simulated above the equator for both northern spring and fall, which is in agreement with other simulations and observations [Lellouch et al. 1993].

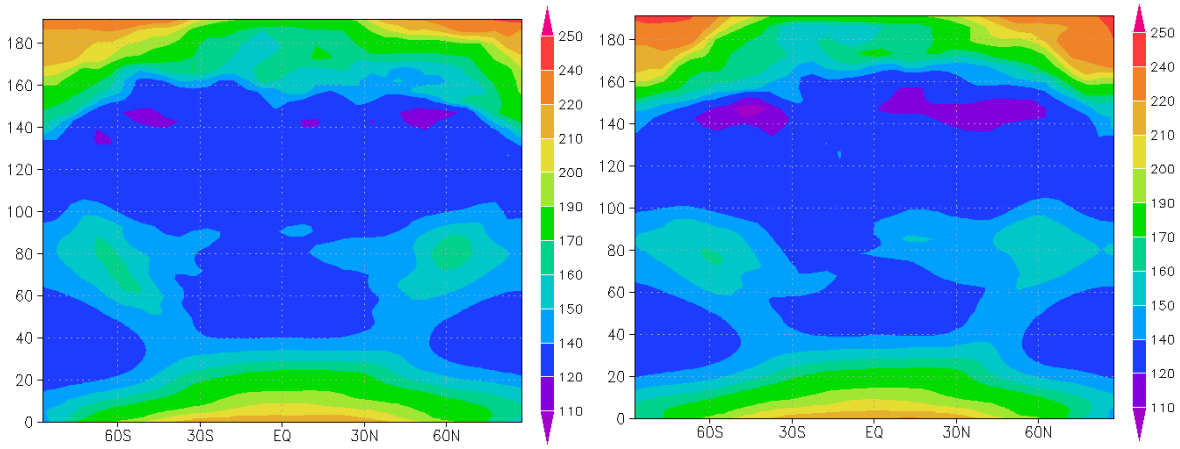

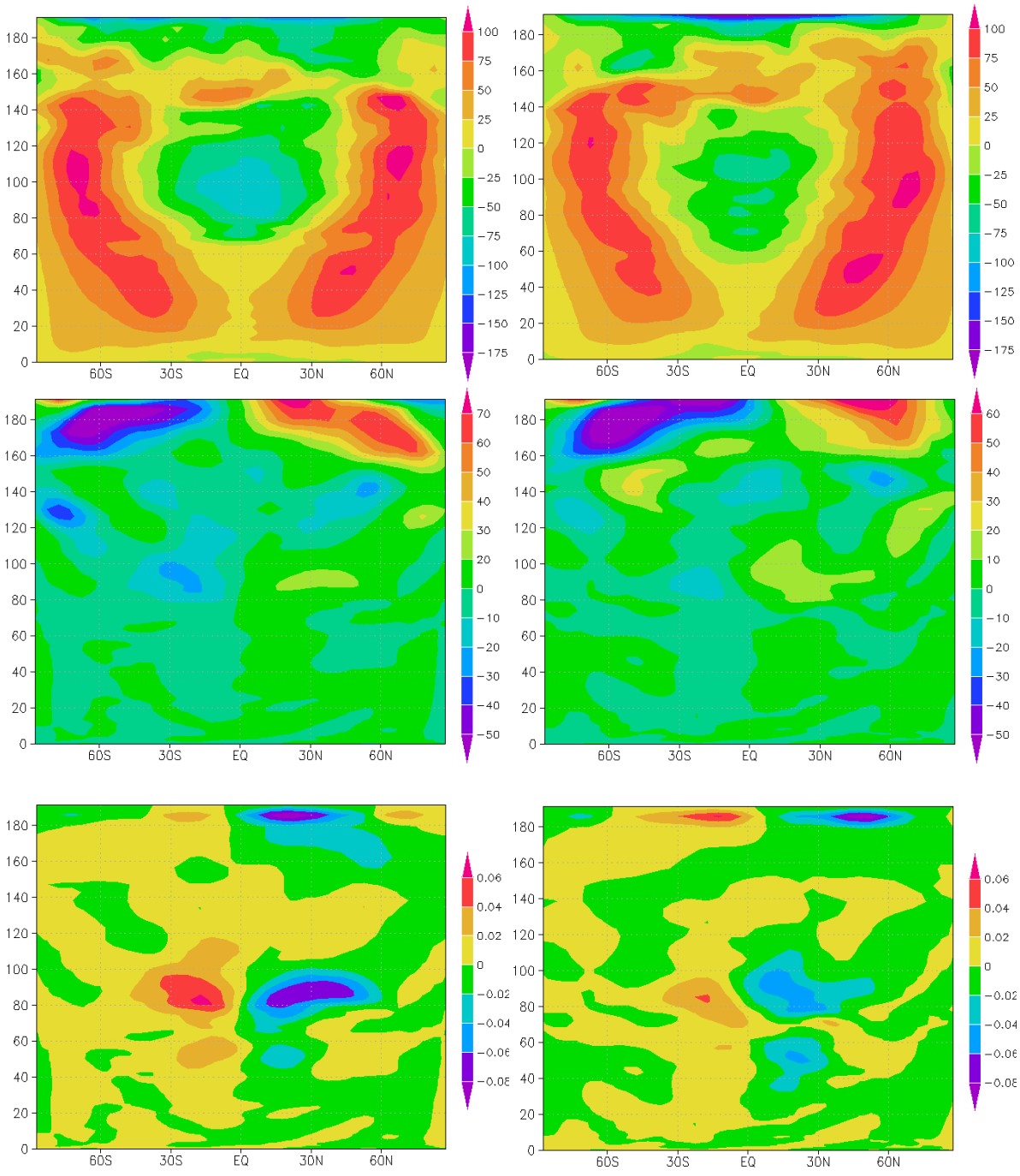
180
160
140
120
100
80
60
40
20
0
60S
30S
EQ
30N
60N
100
75
50
25
0
−25
−50
−75
−100
−125
−150
−175
70
60
50
40
30
20
0
−10
−20
−30
−40
−50
0.06
0.04
0.02
0
−0.02
−0.04
−0.06
−0.08

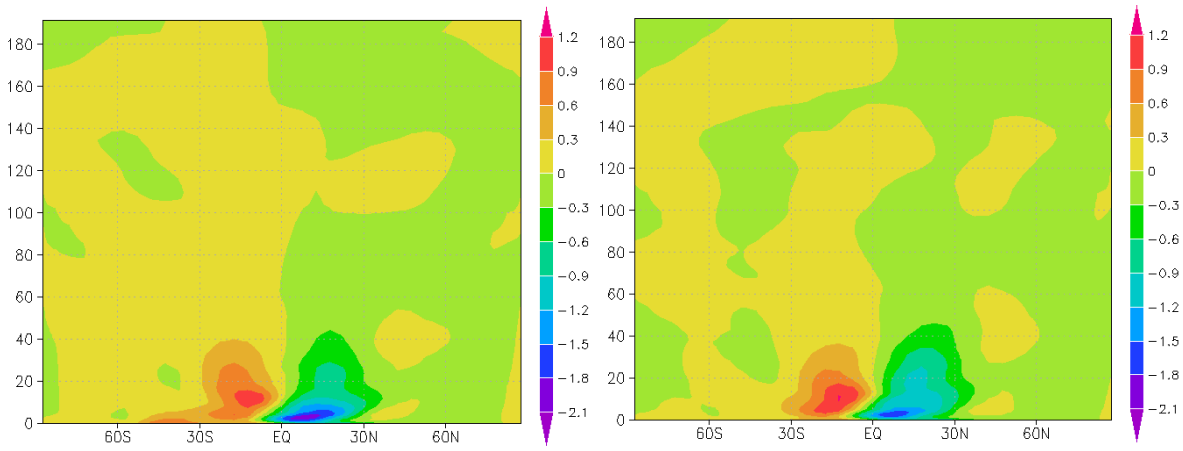

Figure 4.27: Latitude–height cross section of zonal mean atmospheric temperature (K), zonal wind (m/s), meridional wind (m/s), vertical wind (m/s) and mass streamfunction (10^9 kg/s) from the top panel to the bottom in sequence. Left column for Ls = 0^0 and right column Ls = 180^0. The vertical axis is altitude in km.

4.7 Comparison dusty atmosphere with clear atmosphere

In order to explore the contribution of the dust to the Martian atmosphere we ran the 3-D GEM-Mars for 120 sols without dust by simply setting the dust mixing ratio to zero. The following Figures 4.28-4.30 are snap shots at Ls = 90^0 and Ls = 270^0 for comparing dusty and clear Martian atmosphere. In all Figure 4.28-4.30 the top panels are for a dusty atmosphere with two dust (wind shear and dust devils) lifting schemes; middle panels are clear atmosphere with zero dust mixing ratio and no dust lifting schemes; bottom panels are the difference between the values of dusty atmosphere and the values of clear atmosphere. We can see that dust usually warms up the atmosphere below 60 km for both seasons from Figure 4.28.

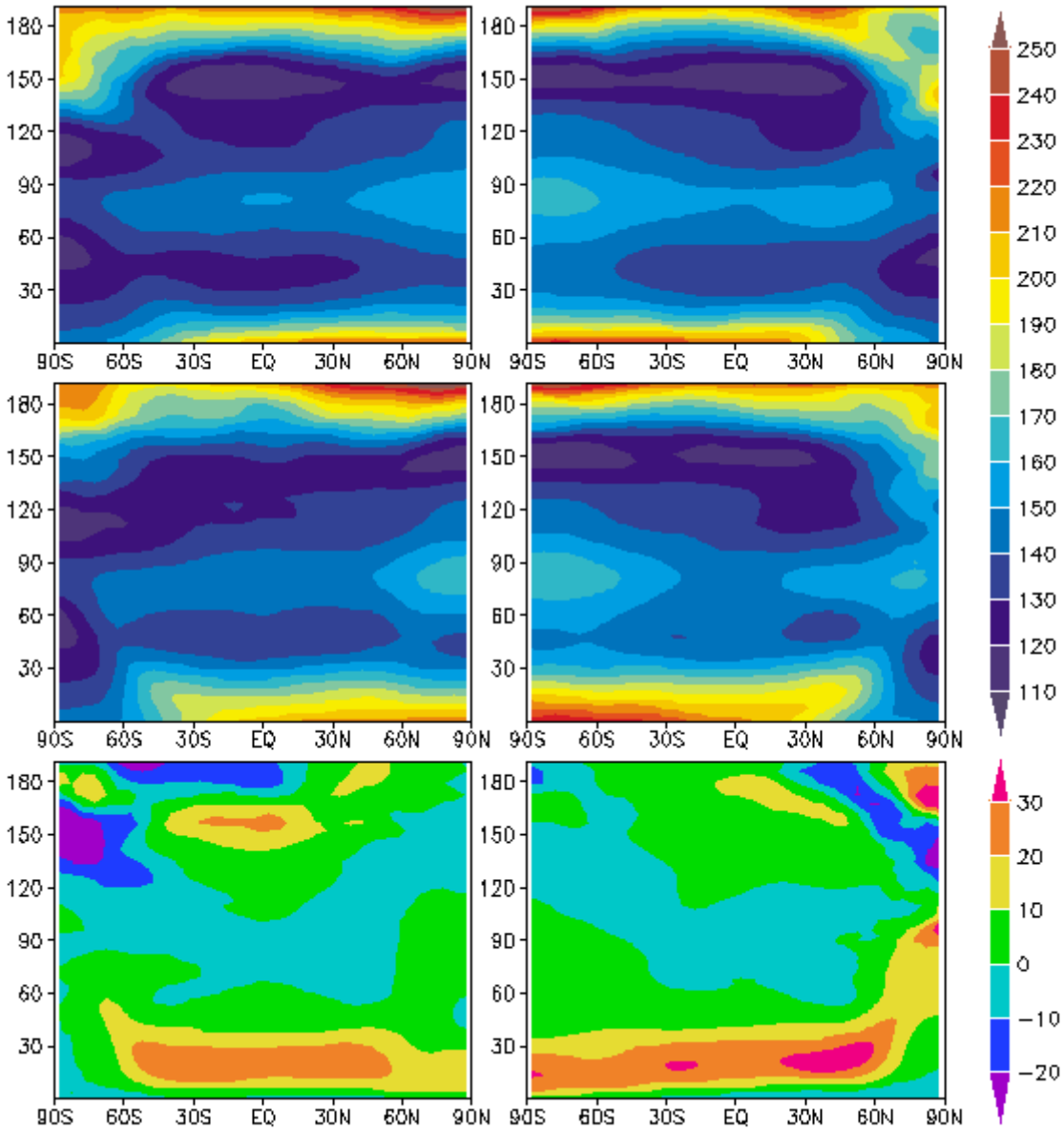

Figure 4.28: Latitude–height cross section of zonal mean atmospheric temperature (K), left column for Ls = 90^0 and right column Ls = 270^0, clear atmosphere top panel, dusty atmosphere (middle), the difference between dusty and clear atmosphere (bottom). The vertical axis is altitude in unit km.

For Ls = 270^0 there is more dust in the middle and low atmosphere therefore more heating occurs in these levels with a maximum difference above 30 K. The dust causes

atmosphere zonal mean temperatures 20-30 K warmer than for the clear atmosphere over the northern polar region in the altitude range between 40 and 110 km above the surface.

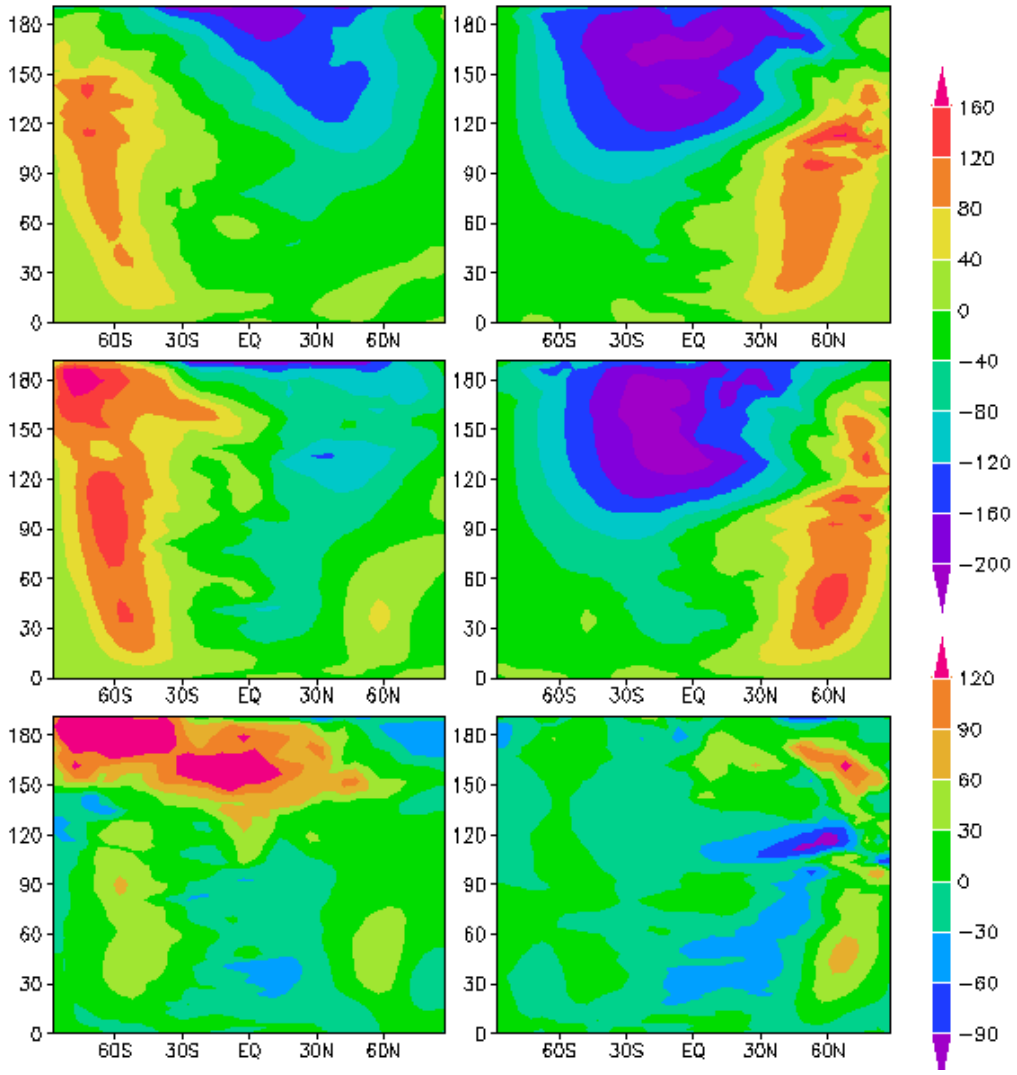

Figure 4.29: Latitude–height cross section of zonal mean atmospheric zonal wind (m/s), left column for Ls = 90^0 and right column Ls = 270^0, clear atmosphere top panel, dusty atmosphere (middle), the difference between dusty and clear atmosphere (bottom). The vertical axis is altitude in unit km.

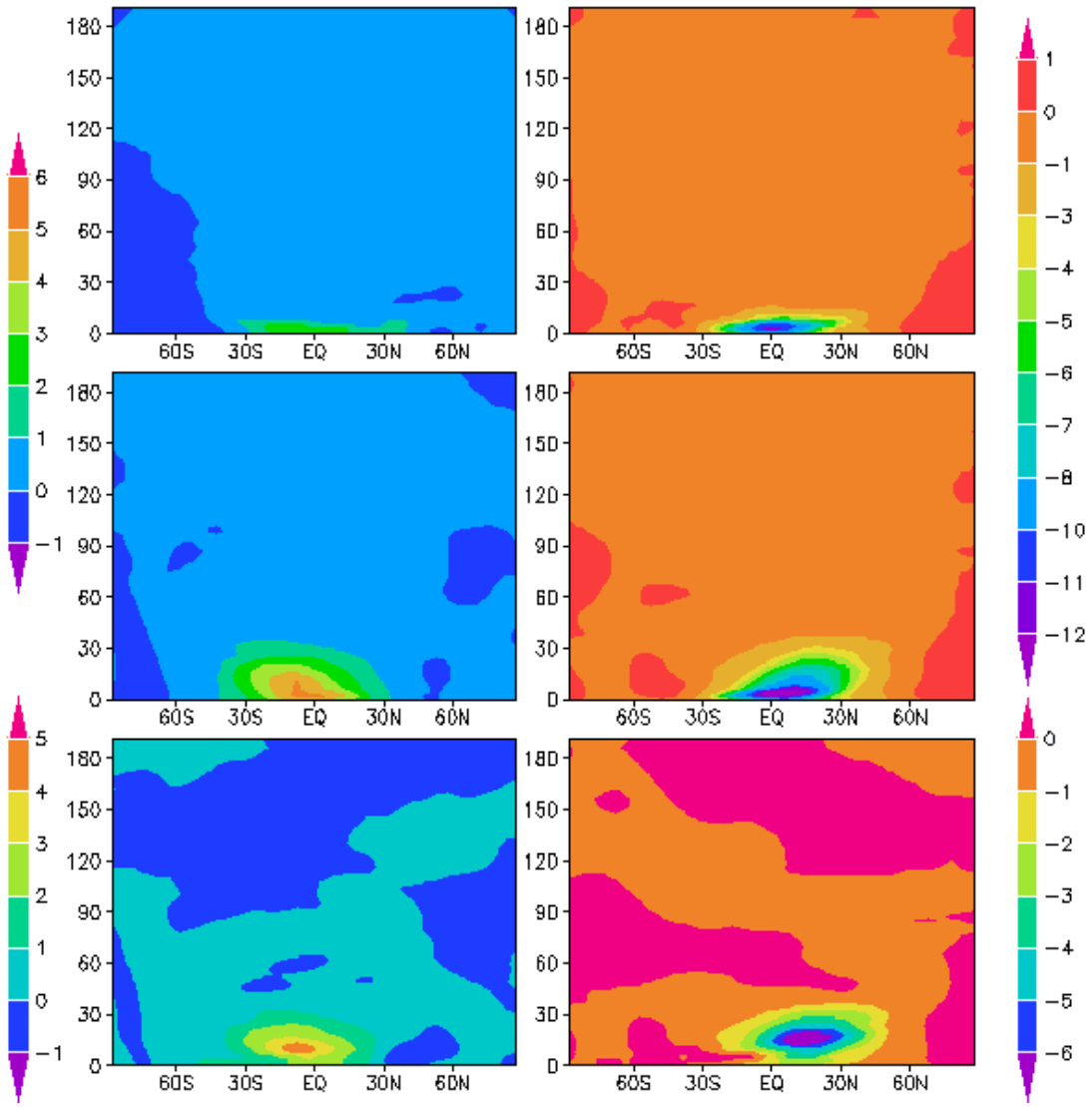

Figure 4.30: Latitude–height cross section of zonal mean atmospheric mass streamfunction (10^9 kg/s), left column for Ls=90^0 and right column Ls=270^0, clear atmosphere top panel, dusty atmosphere (middle), the difference between dusty and clear atmosphere temperature (bottom). The vertical axis is altitude in unit km.

Figure 4.29 shows that the zonal mean wind is stronger over higher latitudes due to dust. We can see that the values of the zonal mean atmospheric mass streamfunction with dust

are enhanced more than 50% compared with a clear atmosphere from Figure 4.30. Mean meridional circulation can reach as high as 40 km in a dusty atmosphere and only below 15 km in a clear atmosphere. Thus, the results demonstrate that the suspended dust in the Martian atmosphere indeed warms up the low and middle atmosphere, enhances the zonal wind and increases the intensity and range of the meridional circulation, i.e. dust affects both thermal structure and dynamics.

Chapter 5 Conclusions

Our Mars GCM GEM-Mars has been enhanced to study the dust cycle including dust lifting, transport and deposition on Mars. The expanded model has successfully simulated Mars dust cycles in a spontaneous and self-consistent way. Our simulations agree with observations in the following respects:

1. During the perihelion season (roughly southern spring and summer, solar insulation is stronger, Ls = 180^0-360^0) is relatively warm and, dusty, and during the aphelion season (Ls = 0^0-180^0) is relatively cool, with less dust.
2. The simulated dust vertical distributions and atmospheric temperatures are generally consistent with the MCS and Phoenix observations.
3. The two dust lifting schemes mechanical and thermal convection both contribute to atmospheric dust loading with mechanical lifting scheme triggering dust storms while dust devils keep the atmospheric dust background.
4. The model can simulate all the main features in the zonal mean circulation with its deep domain. The simulated features are comparable with other simulations.
5. Comparing with clear atmosphere our results confirm that dust contributes to warm the

lower atmosphere, affect dynamics and strengthen the meridional circulation.

Our simulated dust storms show a regular variability with time and locations every Mars year and have simulated maximum globally averaged dust optical depths ~ 0.3 around Ls = 270^0. Observations include planet-encircling dust storms such as in MY 25 with a globally averaged dust optical depth reaching 1.3. The differences between our simulated and observed dust storms in details are:

1. Dust source: Observations show that dust storms occur in several regions on Mars: at the polar cap edges, at the base of high elevation regions in the northern hemisphere, near the polar hood during northern fall, and at mid-latitudes in both hemisphere. However, most dust is lifted from the slopes along mountains and basins, and lifting areas focus in the range between 30^0 S and 30^0 N. For dust devils, the observations of dust devil tracks found that the lifting areas are mostly from two narrow bands centered at 60^0 N and 60^0 S during the spring and summer in both hemispheres, while the equator is the area of a lesser peak and few dust devil tracks are found at the poles and middle latitudes. The GEM-Mars simulations show the locations of dust devils are around the equator where the surface temperature is warm and the sensible heat flux is high.
2. Dust storm location distributions changing with time: As observed by MOC in 1999 a systematic southward migration in the location of dust storms appears as a function of time. Storms in the southern hemisphere tend to follow the receding south polar cap edge, while in the north the storms seem to follow the formation of the polar hood. Our simulations can show the southward migration from northern spring to southern

summer but there is no dust storm along the polar cap edge. Although the near surface wind calculated from GEM-Mars is strong in the polar cap regions, the simulated winter CO_2 ice in both hemispheres is shallower and exists for a shorter time than the observations. The observed CO_2 ice mass variations in the polar regions show that the mean CO_2 ice disappears around Ls = 90^0 - 180^0 in the northern hemisphere and Ls = 270^0 - 300^0 in the southern hemisphere [Karatekin et al., 2006]. But our simulation shows a longer period without polar ice. For the northern hemisphere the period is around Ls = 30^0 to 180^0, and for the southern hemisphere is around Ls = 180^0 – 360^0. Thus GEM-Mars could not simulate dust storms located in the polar regions of 60^0 N ~ 90^0 N during Ls = 109^0 – 189^0 and of 60^0 S ~ 90^0 S during Ls = 190^0-274^0 as observed by MOC in 1999 [Cantor et al., 2001].

3. The surface albedo and thermal inertia do not change with time and the surface roughness is a constant globally in our model. Albedo and thermal inertia feedbacks have thermodynamic effects on the local atmosphere [Smith, 2004; Kahre et al., 2005a] and could affect the simulated dust cycle and the simulated spatial pattern of annual net dust deflation/deposition. Dust storms over polar caps can change the polar surface albedo and thereby the polar heat budget. Additionally, including a spatially and temporally varying surface roughness field could affect the results.

In other models [Newman (2002); Basu et al.,(2004, 2006); Kahre et al., (2006)], the wind stress threshold for mechanical dust lifting is a global constant; up to three dust bins are used in the dust partial size distribution without any sub-bin size distribution; there is no consideration of unresolved subgrid-scale wind gust which cannot be simulated by the

GCM due to the coarse resolution. In our model the saltation wind threshold is calculated every time step and is variable with the topography and the surface temperature; the four transported dust bins follow a tri-modal lognormal probability density function size distribution and each sub-bin has a normalized size distribution which can increase the precision of the calculation dust optical depth; the near surface wind field is recalculated using a Weibull speed distribution with five wind bins. Our results demonstrate that terrestrial DEAD model is suitable to simulate dust cycle on Mars. We could be able to match both the column dust optical depth and vertical dust profile better if increase the dust lifting parameter a little bit higher in the DEAD. Ideally we could add a threshold in the devil lifting scheme to improve the simulations.

In further Mars GCM studies, the addition of a water cycle, a multi-layer surface scheme, the simulation of water ice clouds, gravity wave drag, and the use of surface roughness map will improve the accuracy of our model. For the Martian dust cycle the study of the evolution of surface dust reservoirs may help simulate the inter-annual variability of global dust storms successfully [Newman, 2015]. Furthermore, because of the flexible configuration of GEM, i.e. horizontal and vertical grid can have uniform resolution or regional high resolution over a region of interest, GEM-Mars could be suitable for simulation of the weather at a local landing site on Mars surface.

References

Akingunola, A., Martian water cycle modeling with the second generation of the Global Mars Multiscale Model, *York University (Canada), ProQuest Dissertations Publishing*, 2009. NR51665.

Appelbaum, J. and M. D. Flood (1989), Solar Radiation on Mars, *NASA Technical Memorandum 102299*.

Balme, M. R., P. L. Whelley, and R. Greeley (2003), Martian dust devil track survey in Argyre Planitia and Helles Basin, *J. Geophys. Es.*, *108* (E8), 5086 doi:10.1029/2003JE002096.

Basu, S., M. I. Richardson, and R. J. Wilson (2004), Simulation of the Martian dust cycle with the GFDL Mars GCM, *J. Geophys. Res.*, 109, E11006, doi:10.1029/2004JE002243

Martian Seasons and Solar Longitude. (2015, March 06). Retrieved from (Martian Seasons and Solar Longitude)

Basu, S. J., R. M. Wilson, and A. Ingersoll (2006), Simulation of spontaneous and variable global dust storms with the GFDL Mars GCM, *J. Geophys. Res., 111,* E09004, doi:10.1029/2005JE002660.

Bell, J., M. Wolff, and The Hubble Heritage Team (2001, October 11), *Scientists Track "Prefect Storm" on Mars*, Retrieved from http://hubblesite.org/newscenter/archive/releases/2001/31/image/a/

Benoit, R. J. Cote, and J. Mailhot, 1989: Inclusion of a TKE boundary layer parameterization in the Canadian regional finite-element model, *Mon. Wea. Rev.*, 117, 1726-1750.

Bougher, S. W., and R. E. Dickinson (1988), Mars mesosphere and thermosphere Global mean heat budget and thermal structure, *J. Geophys. Res., 94*, 7325-7337.

Briegleb, B. (1992), Delta_Eddington Aprroximation for Solar Radiation in the NCAR Community Climate Model, *J. Geophys. Res., Vol. 97*, May 20, 1992, Pages 7603-7612.

Carr, M. H., and Head, J. W. (2010), Geological History of Mars, *EPSL, 296, 185-203*.

Cantor, B., P. B. James, M. Caplinger, and M. J. Wolff (2001), Martian dust storms: 1999 Mars Orbiter Camera observations, *J. Geophys. Res., 106,* E10, PAGES 23,653-23,687.

Clancy, R. T., S. W. Lee, G. R. Gladstone, W. W. Mcmillan, and T. Roush, A new model for Mars atmospheric dust based upon analysis of ultraviolet through infrared observations from mariner 9, Viking, and Phobos, *J. Geophys. Res., 100*, 5251-5263, 1995.

Clancy, R.T., B. J. Sandor, M. J. Wolff, P. R. Christensen, M. D. Smith, J. C. Pearl, B. J. Conrath, R. J. Wilson (2000), An intercomparison of ground-based millimeter, MGS TES, and Viking atmospheric temperature measurements: seasonal and interannual variability of temperature and dust loading in the global Mars atmosphere, *J. Geophys. Res., Volume: 105*, 9553-9572.

Conrath, B. J., Thermal Structure of the Martian atmosphere during the dissipation of the dust storm of 1971, *Icarus, 24, 36.46, 1975*.

Cote, J., S. Gravel, A. Methot, A. Patoine, M. Roch, and A. Staniforth (1997), The Operational CMC-MRB Global Environmental Multiscale (GEM) Model. Part I: Design Considerations and Formulation, *Monthly Weather Review, 126,* PAGES 1373-1395.

Deardorff, J. W., A parameterization of ground-surface moisture content for use in atmospheric prediction models, J. *Appl. Meteor., 16*, 1182.1185, 1978.

Fisher, J. A., M. I. Richardson, C. E. Newman, M. A. Szwast, C. Graf, S. Basu, S. P. Ewald, A. D. Toigo, and R. J. Wilson (2005), A survey of Martian dust devil activity using Mars Global Surveyor Mars Orbiter Camera Images, *J. Geophys. Res., 110*, E03004, doi:10.1029/2003JE002165.

Forget, F. et. al. (1992), CO2 Snowfall on Mars: Simulation with a General Circulation Model, *ICARUS 131*, 302–316 (1998).

Forget, F., F. Hourdin, R. Fournier, C. Hourdin, O. Talagrand, and et al., (1999), Improved general circulation models of the Marian atmosphere from the surface to above 80 km, *J. Geophys. Res., 104*, E10, PAGES 24,155-24,175.

Fouquart, Y., and B. Bonnel, Computations of Solar heating of the Earth's atmosphere: A new parameterization, *Contrib. Atmos. Phys, 53, 35.62, 1980*.

Garand, L., Some Improvements and Complements to the Infrared Emissivity Algorithm Including a Parameterization of the Absorption in the Continuum Region, *J. Atm. Science, 40*, 230-244.

Greeley, R., and J. D. Iversen, *Wind as a geologial process*, no. 4 in Cambridge planetary Science Series, Cambridge Univ. Press, New York, NY, 1985.

Greeley, R., et al. (2006), Active dust devil in Gusev creater, Mars: Observations from the Mars Exploration Rover Spirit, *J, Geophys. Res., 11*, E12S09, doi:10.1029/2006JE002743.

Haberle, R. M., J. L. Hollingsworth, A. Colaprete, A. F. Bridger, C. P. McKay, J. R. Murphy, J. Schaeffer, and R. Freedman, Mars atmospheric dynamics as simulated by the NASA Ames General Circulation Model 1. The zonal-mean circulation, *J. Geophys. Res., 98*, 3093-3123, 1993b.

Haberle, R. M., Mars, *Planetary and Space Science Vol 46: 1085–1097, 1998*.

Haberle, R., et al. (1999), General circulation model simulations of the Mars Pathfinder atmospheric structure investigation/meteorology data, *J. Geophys. Res.*, 104, 8957.

Haberle, R. M., J. R. Murphy, and J. Schaeffer (2003), Orbitial change experiments with a Mars general circulation model, *Icarus, 161*, 66.

Hartogh, P., A. S. Medvedev, T. Kuroda, R. Saito, G. Villanueva, A. G. Feofilov, A. A. Kutepov, and U. Berger (2005), Description and climatology of a new general circulation model of the Martian atmosphere, *J. Geophys. Res., 110*, E11008, doi:10.1029/2005JE002498.

Heavens, N. G., M. I. Richardson, A. Kleinbohl, D. M. Kass, D. J. McCleese, W. Abdou, J. L. Benson, J. T. Schofield, J. H. Shirley, and P. M. Wolkenberg (2011), Vertical distribution of dust in he Martian atmosphere during northern spring and summere: High-altitude tropical dust maximum at northern summer solstice, *J. Geophys. Res., 116*, E01007, doi:10.1029/2010JE003692.

Heavens, N. G., M. I. Richardson, A. Kleinbohl, D. M. Kass, D. J. McCleese, W. Abdou, J. L. Benson, J. T. Schofield, J. H. Shirley, and P. M. Wolkenberg (2011), The vertical distribution of dust in he Martian atmosphere during northern spring and summere: Observations by the mars Climate sounder and analysis of zonal average vertival dust profiles, *J. Geophys. Res., 116*, E04004, doi:10.1029/2010JE003692.

Hourdin, F., A new representation of the CO2 15 _m band for a Martian general circulation model, J. Geophys. *Res., 97, 18319.18335, 1992*.

Iversen, J. D., and B. R. White, Saltation threshold on Earth, Mars, and Venus, Sedimentology, 29, 111–119, 1982.

Karatekin, Ö., T. V. Hoolst, and V. Dehant (2006), Martian global-scale CO_2 exchange from time-variable gravity measurements, *J, Geophys. Res., 11,* E06003, doi:10.1029/2005JE002591.

Kahre, M. A., J. R. Murphy, and R. M. Haberle (2006), Modeling the Martian dust cycle and surface dust reservoirs with the NASA Ames general circulation model, *J. Geophys. Res., 111*, E06008, doi:10.1029/2005JE002588.

Kolmogorov, A. N., 1942: Equations of turbulent motion of an incompressible turbulent fluid, *Izv. Akad, Nauk SSSR, Ser. Phys., 6*, No. 1-2, 56-58.

Komguem, L., J. A. whiteway, C. Dickinson, M. Daly, M. T. Lemmon (2013), Phoenix LIDAR measurements of Mars atmospheric dust, *Icarus, 223*, 649-653.

Kuroda, T., N. Hasimoto, D. Sakai, and M. Takahashi (2005), Simulation of the Marian Atmosphere Using a CCSR/NIES AGCM, *Journal of the Meteorological Society of Japan, Vol. 83*, No. 1, pp. 1-19.

Lemmon, M. T., M. J. Wolff, J. F.88775. Bell, M. D. Smith, P.H. Smith (2014), Dust, clouds, and the atmospheric optical depth record over 5 Mars years of the Mars exploration rover mission, Fifth international workshop on the Mars atmosphere: Modelling and observations, Jan 13-16, 2014.

Leovy, C. B., R. W. Zurek, and J. B. Pollack (1973), Mechanism for Mars dust storms, *J. Atmos. Sci., 30, 749-762.*

Liou, K. N. (2002), *An introduction to Atmospheric Radiation*, 2nd edition, London; Academic Press.

L´opez-Valverde, M. A., and M. L´opez-Puertas, A non-local thermodynamic equilibrium radiative transfer model for infrared emissions in the atmosphere of Mars, 1, Theoretical basis and nighttime populations of vibrational levels, *J. Geophys. Res., 99, 13093.13115, 1994a.*

Malin, C. M., M. W. Calvin, R. T. Clancy, M. R. Haberle, B. P. James, C. P. Thomas, J. M. Wolff, F. J. Bell, W. S. Lee (2007), Climate, weather, and north polar observations from the Mars Reconnaissance Orbiter Mars Color Imager, *Icarus 194 (2008) 501-512*.

Mailhot, J., and R. Benoit, 1982: A finite-element model of the atmospheric boundary layer suitable for use with numerical weather prediction models, *J. Atmos. Sci., 39*, 2249-2266.

Martin, T. Z., Thermal infrared optical of the Mars atmosphere, *Icarus, 66,* 2-21, 1986.

Marticorena, B., and G. Bergametti, Modeling the atmospheric dust cycle: 1. Design of a soil-derived dust emission scheme, *J. Geophys. Res., 100(D8),* doi:10.1029/95JD00,690, 16,415–16,430, 1995.

McCleese, D. J., J. T. Schofield, F. W. aylor, S. B. Calcut, M. C. Foote, D. M. Kass, C. B. Leovy, D. A. Paige, P. L. Read, and R. W. Zurek (2007), Mars Climate Sounder: An investigation of thermal and water vapor structure, dust and condensate distributions in the atmosphere, and energy balance of the condensate distributions in the atmosphere, and energy balance of the polar regions, *J. Geophys. Res., 112*, E05S06, doi:10.1029/2006JE002790.

Montabone , L., F. Forget, E. Millour, R.J. Wilson, S.R. Lewis, B. Cantor, D. Kass, A. Kleinböhl, M.T. Lemmonh, M.D. Smith, M.J. Wolff (2015), Eight-year climatology of dust optical depth on Mars, *Icarus, VOL 251*, doi:10.1016/j.icarus.2014.12.034

Moores, J. E., M. T. Lemmon, P. H. Smith, L. Komguem, and J. A. Whiteway (2010), Atmospheric dynamics at the Phoenix landing site as seen by the Surface Stereo Imager, *J. Geophys. Res., 115*, E00E08, doi:10.1029/2009JE003409.

Moudden Y. and J. C. McConnell (2005), A new model for multiscale modeling of the Martian atmosphere, GM3, *J. Geophys. Res., 110*, E04001, doi:10.1029/2004JE002354.

Newman, C. E., and M. I. Richardson (2015), The impact of surface dust source exhaustion on the martian dust cycle, dust storms and interannual variability, as simulated by the MarsWRF General Circulation Model, *Icarus 257 47-87*, doi:10.1016/j.icarus.2015.03.030.

Newman, C. E., Lewis, S. R., and Read, P. L., Modeling the Martian dust cycle 1. Representation of dust transport processes, *J. Geophys. Res., 107* (2002), 5123, doi:10.1029/2002JE001910.

Pankine, A. A., and A. P. Ingersoll (2002), Interannual variability of Martian global dust storms: Simulations with a low order model of the general circulation, *Icarus, 155*, 299-323.

Renno, n. O., M. L. Burkett, and M. P. Larkin, A simple thermodynamical theory for dust devils: Test of a scaling theory using Pathfinder data, *J. Geophys. Res., 105*, 1859-1865, 1998.

Richrdson, M. I., A. D. Toigo, and C. E. Newman (2007), PlanetWRF: A general purpose, local to global numerical model for planetary atmospheric and climate dynamics, *J. Geophys. Res., 112*, E09001, doi:10.1029/2006JE002825.

Savijarvi, H., Mars boundary-layer modeling: Diurnal moisture cycle and soil properties at the Viking Lander 1 site. *Icarus, 117*, 120-127

Savijarvi, H., A. Maattane, J. Kauhanen, and A. Harri (2003), MarsPathfinder: New data and new model simulations, *Q. J. R. Meteorol. Soc., 130*, 669-683.

Smith, M. D. (2004), Interannual variability in TES atmospheric observations of Mars during 1999-2003, *Icarus*, *167*, 148-165.

Smith, M. D. (2009), THEMIS observations of Mars aerosol optical depth from 2002-2008, *Icarus, 202*, 444-452.

Smith, D. E., Zuber, M. T., Solomon, S. C., Phillips, R. J., Head, J. W., Garvin, J. B., Banerdt, W. B., Muhleman, D. O., Pettengill, G. H., Neumann, G. A., Lemoine, F. G., Abshire, J. B., Aharonson, O., Brown, C. D., Hauck, S. A., Ivanov, A. B., McGovern, P.J., Zwally, H. J., and Duxbury, T. C. (2001) The Global Topography of Mars and Implications for Surface Evolution. *Science, 284 (5419)*. pp. 1495-1503. ISSN 0036-8075.

Smith, M. D., M. J. Wolff, R. T. Clancy, A. Kleinböhl, and S. L. Murchie (2013), Vertical distribution of dust and water ice aerosols from CRISM limb-geometry observations, *J. Geophys. Res. Planets*, *118*, 321-334, doi:10.1002/jgre.20047.

Staniforth, A. (1997), Regional modeling: A theoretical discussion, *Meteor. Amos. Phys.*, *63*, 15-29.

Stull, R. B. (2009), *An Introduction to Boundary Layer Meteorology*, Springer Science.

Taylor, P. A., P.-Y. Li, D. V. Michelangeli, J. Pathak, and W. Weng (2007), Moudelling dust distributions in the atmospheric boundary layer on Mars, *Boundary Layer Meteorol., 125, 305-328,* doi:10.1007/s10546-007-9158-9.

Tennekes, H., and J. L. Lumley, 1972: *A First Course in Turbulence*, MIT Press, 300 pp.

The Mars Climate Database Projects, *Martian Seasons and Solar Longitude*, Retrieved on March 06, 2015, from: http://www-mars.lmd.jussieu.fr/mars/time/solar_longitude.html.

Toon, O. B., C. P. Mckay, T. P. Ackerman, and K. Santhanam, Rapid calculation of radiative heating rates and photodissociation rates in inhomogeneous multiple scattering atmospheres, *J. Geophys, Res., 94, 16287-16301, 1989.*

Wilson, R. J., and K. Hamilton (1997), Comprehensive model simulation of thermal tides in the Martian atmosphere, *J. Atmos. Sci., 53(9),* 1290-1326.

Whelley, P. L., *and* R. Greeley *(*2008*),* The distribution of dust devil activity on Mars, *J. Geophys. Res., 113, E07002, doi:*10.1029/2007JE002966.

White, B. R., Soil transport by winds on Mars, *J. Geophys. Res.*, *84*(B9), 4643–4651, 1979.

Wu, H., Modelling mineral dust lifting and transport in GEM-AQ: Sensitivity studies and comparison with measurements, *York University (Canada), ProQuest Dissertations Publishing*, 2010. NR62452.

Zhang, L., J. F. Kok, D. K. Henze, Q. Li, and C. Zhao (2013), Improving simulations of fine dust surface concentrations over the western United States by optimizing the particle size distribution, *Geophys. Res. Lett., 40, 3270–3275*, doi:10.1002/grl.50591.

Zender, C. S., H. Bian, and D. Newman, Mineral Dust Entrainment And Deposition (DEAD) model: Description and 1990s dust climatology, *J. Geophys. Res.*, 108(D14), 4416, doi:10.1029/2002JD002775, 2003.

Appendix A: Delta-Eddington Approximation

To incorporate the forward peak contribution in multiple scattering, we may consider an adjusted absorption and scattering atmosphere. The adjusted optical properties include asymmetry factor (the first moment of phase function), optical depth, and single scattering albedo in each layer using Similarity Theory [Liou, 2009]. Delta-Eddington approximation has been employed in the GCM for solar absorption and scattering radiation as described in [Briegleb, 1992]. There are four parameters are the inputs to the radiative transfer equations: extinction optical depth τ, single-scattering albedo ω, asymmetry factor g, and the forward scattering fraction f. The two-stream and Eddington methods for radiative transfer are good approximations for optically thick layers, but they produce inaccurate results for thin layers and when significant absorption is involved. [Liou, 2002, p. 310]. To improve the accuracy the fraction of scattered energy residing in the forward peak, the forward scattering fraction f, is removed from the scattering parameters, and adjust optical depth, single-scattering albedo and asymmetry factor as followings:

$$\tau^* = \tau(1 - \omega f) \tag{A.1}$$

$$\omega^* = \omega \left(\frac{1-f}{1-\omega f}\right) \tag{A.2}$$

$$g^* = \frac{g-f}{1-f} \tag{A.3}$$

The values of ω and g are shown in Table 2.1, the forward scattering fraction f is expresses in terms of the asymmetry factor $f=g^2$ [Liou, 2002, p. 313]. In a numerical model, the vertical dimension of the model usually is divided into a number of layers. The Delta-Eddington nonconservative (ω <1) solutions for each layer for direct radiation at cosine zenith angle μ_0 are following [Briegleb, 1992]:

$$R(\mu_0) = (\alpha-\gamma)\bar{T}e^{-\frac{\tau^*}{\mu_0}} + (\alpha+\gamma)\bar{R} - (\alpha-\gamma) \tag{A.4}$$

$$T(\mu_0) = (\alpha+\gamma)\bar{T} + (\alpha-\gamma)\bar{R}e^{-\frac{\tau^*}{\mu_0}} - (\alpha+\gamma-1)e^{-\frac{\tau^*}{\mu_0}} \tag{A.5}$$

$$\bar{R} = (u+1)(u-1)\left(e^{\lambda\tau^*} - e^{-\lambda\tau^*}\right)N^{-1} \tag{A.6}$$

$$\bar{T} = 4uN^{-1} \tag{A.7}$$

where

$$\alpha = \frac{3}{4}\omega^*\mu_0\left(\frac{1+g^*(1-\omega^*)}{1-\lambda^2\mu_0^2}\right) \tag{A.8}$$

$$\gamma = \frac{1}{2}\omega^*\left(\frac{1+3g^*(1-\omega^*)\mu_0^2}{1-\lambda^2\mu_0^2}\right) \tag{A.9}$$

$$N = (u+1)^2e^{\lambda\tau^*} - (u-1)^2e^{-\lambda\tau^*} \tag{A.10}$$

$$u = \frac{3}{2}\frac{1-\omega^*g^*}{\lambda} \tag{A.11}$$

To calculate the transmission and reflectivity for every interface over the entire column, we combine the total transmission start from the top and proceed downward, and combine the total reflectivity from the surface and proceed upward. Then the upwards and downwards fluxes at every interface is calculated.